UNIVERSITY OF HELSINKI REPORT SERIES IN PHYSICS

HU-P-D139

SEARCH FOR A LIGHT HIGGS BOSON IN CENTRAL EXCLUSIVE DIFFRACTION: METHOD AND DETECTORS

Juha Kalliopuska

Division of High Energy Physics
Department of Physical Sciences
Faculty of Science
University of Helsinki
Helsinki, Finland

ACADEMIC DISSERTATION

To be presented with the permission of the Faculty of Science of the University of Helsinki, for public criticism in the University Main Building, small hall, Fabianinkatu 33 (4th floor), on Tuesday, 24th of April 2007, at 12 o'clock.

Helsinki 2007

ISBN 978-952-10-3243-1 (printed version)
ISSN 0356-0961
ISBN 978-952-10-3244-8 (pdf version)
http://ethesis.helsinki.fi
Yliopistopaino
Helsinki 2007

Acknowledgements

The thesis is a report of the research activity carried out during the years 2002-2007. The work was done at the European Organization for nuclear research (CERN), Helsinki Institute of Physics (HIP) and Technical Research Center of Finland (VTT). The first publication was prepared at CERN in Switzerland and the others in collaboration with HIP and VTT in Finland.

I am indebted to Prof. Risto Orava who suggested me the topic of the thesis, made possible the collaboration with VTT and supervised me through the years. I would like to express my gratitude to my instructor, D.Sc. (Tech) Simo Eränen, who helped me with both practical and theoretical problems and took me to work in his group at VTT. Without their guidance and support this work would not have been possible.

I would like to acknowledge Stefan Tapprogge and Kenneth Österberg who were my supervisors during my time at CERN. They guided me into the fascinating world of particle physics and instructed me in the research for the first publication. I want to thank the pre-examiners of this thesis, Valery Khoze and Erik Heijne. I am grateful to Bert Van Koningsveld for granting me the access to the simulation tools at CERN. I would also like to express my gratitude to Rauno Lauhakangas, Kari Kurvinen and Antti Numminen for the measurements and bonding done at HIP. In addition, I would like to thank Ari Kiiskinen, Nick van Remortel and Tom Schulman for helping me in the final stages of writing the thesis. The help of Adelaide Lönnberg was needed to make the language of the thesis more fluent.

The financial support of the Helsingin Sanomain 100-vuotissäätiö, the Waldemar von Frenckell Foundation, HIP and VTT are deeply acknowledged in that order.

I have had the pleasure of making good friends in the international research community, and I would especially like to stress my gratitude to Artto Aurola, Aatos Heikkinen, Niko Marola, Tuula Mäki, Mikko Möttönen, Elias Noschis, Lukas Tlustos and Mikko Voutilainen.

Finally, I wish to thank my parents, my grand father and the Garam family, especially Virva, for their support and unquestionable love for me during the years of research, the results of which are enclosed within these pages.

Helsinki, March 2nd, 2007

Juha Kalliopuska

J. Kalliopuska: Search for a light Higgs boson in central exclusive diffraction: method and detectors, 2007, 102 p. + appendices, University of Helsinki, Report Series in Physics, HU-P-D139, ISSN 0356-0961, ISBN 978-952-10-3243-1 (printed version), ISBN 978-952-10-3244-8 (pdf version), http://ethesis.helsinki.fi.

INSPEC classification: A06, A07, A29, B25, B74, C40, C74.

Keywords: Higgs boson, central exclusice diffraction, missing mass method, silicon radiation detector, 3D detector, semi-3D detector, radiation hardness, TCAD simulation.

Abstract

By detecting leading protons produced in the Central Exclusive Diffractive process, $p+p \rightarrow p+X+p$, one can measure the missing mass, and scan for possible new particle states such as the Higgs boson. This process augments - in a model independent way - the standard methods for new particle searches at the Large Hadron Collider (LHC) and will allow detailed analyses of the produced central system, such as the spin-parity properties of the Higgs boson. The exclusive central diffractive process makes possible precision studies of gluons at the LHC and complements the physics scenarios foreseen at the next e^+e^- linear collider.

This thesis first presents the conclusions of the first systematic analysis of the expected precision measurement of the leading proton momentum and the accuracy of the reconstructed missing mass. In this initial analysis, the scattered protons are tracked along the LHC beam line and the uncertainties expected in beam transport and detection of the scattered leading protons are accounted for.

The main focus of the thesis is in developing the necessary radiation hard precision detector technology for coping with the extremely demanding experimental environment of the LHC. This will be achieved by using a 3D silicon detector design, which in addition to the radiation hardness of up to 5×10^{15} neutrons/cm^2, offers properties such as a high signal-to-noise ratio, fast signal response to radiation and sensitivity close to the very edge of the detector. This work reports on the development of a novel semi-3D detector design that simplifies the 3D fabrication process, but conserves the necessary properties of the 3D detector design required in the LHC and in other imaging applications.

Contents

Introduction

The main motivation for the world's largest research project, the Large Hadron Collider (LHC), now being commissioned at CERN, is to search for the mechanism that generates the masses of basic matter particles. This thesis focuses on the LHC discovery potential of the Higgs boson in Central Exclusive Diffraction (CED), $p + p \rightarrow p + X + p$, where by measuring the leading forward pair of protons, the energy-momentum conservation can be utilized to produce a uniquely complementary analysis. For measuring the small angle beam-like protons in the LHC environment, novel radiation hard high-precision detector technology is required.

Chapter I gives an overview of the LHC, its operation principles and the detectors of its high luminosity experiments. The current superconducting magnets of the LHC are able to create proton-proton collision energies as high as 14 TeV/c^2. The chapter also introduces the planned steps towards the LHC upgrade, Super-LHC (SLHC), which in its final state should provide twice the collision energies of the LHC. The LHC or possible SLHC will be able to unearth evidence that supports or disproves current theories of particle physics.

Chapter II introduces currently best known description of fundamental particles and forces, the so-called Standard Model (SM) of particle physics. It has been able to define masses of the fundamental particles and interaction strengths of their intermediate forces with high accuracy. Chapter III gives a brief description of the Higgs mechanism and a minimal supersymmeric Standard Model (MSSM). The masses of fundamental particles and the force carriers are generated via a spontaneous symmetry breaking of a complex Higgs field in the SM and two complex Higgs fields in the MSSM. Moreover, it has been shown how a possible Higgs boson signal could be seen in the LHC and Super LHC (SLHC) experiments.

The missing mass (MM) method described in Chapter IV aims at finding clear signs of a "light" Higgs boson, having mass in the range $80 - 130$ GeV/c^2, in the central exclusive diffractive process. The MM method uses position information of the scattered protons obtained from the accurate forward tacking detectors on both sides of the interaction point (IP). The detectors are positioned at 220 and 420 m from the IP and can approach close to the beam line for proton tacking at very small scattering angles. The method can also be used for studying the extra dimensions.

Chapter V gives a detailed overview on the forward physics experiments, TOTEM and FP420, in which the MM method will be applied. The TOTEM experiment has a key role in calibrating the LHC parameters by defining the total proton-proton (pp) cross-section with high accuracy, and in studying the elastic pp scattering and diffractive phenomena in combination with the central detector CMS. The FP420 is a research and development project that aims to use the MM method for reconstructing the mass of the centrally produced diffractive system as introduced in Chapter IV.

The tacking detector systems and their sensors with a high spatial resolution and detection sensitivity close to their very edge are described in Chapter VI. The radiation tolerance requirements are represented in more detail because the detectors have to be able to function in a hostile radiation environment. Chapter VII introduces a new detector concept, the 3D detector, which offer significant benefits over the common planar detector and is well suited to the LHC experiments and imaging applications. Most of the chapter is dedicated to the novel semi-3D detector concept that simplifies the device processing while keeping the main benefits of the 3D detector. In Chapter VIII, an introduction to semiconductor fabrication is given and the key process steps in the 3D detector fabrication are viewed and discussed in detail.

Chapters IX and X give an overview of the characterization methods of the radiation detectors. Chapter IX gives an introduction to a 3D finite element method (FEM) simulation of semiconductor devices used throughout the thesis and shows its potential for characterizing full 3D silicon radiation detector components. Finally, Chapter X represents the measurement setups for defining various characteristics of the semi-3D detectors fabricated at VTT. The semi-3D detectors are mainly designed for tracking in high energy physics, but their X-ray imaging properties are characterized using a medical imaging readout chip, Medipix2, and various X-ray sources. The results are compared with a reference planar pixel detector.

Summary of original publications

I *TOTEM Forward Measurements: Exclusive Central Diffraction*, J. Kalliopuska, J.W. Lämsä, T. Mäki, N. Marola, R. Orava, K. Österberg, M. Ottela and S. Tapprogge, CERN-2005-014, DESY-PROC-2005-001, 448 - 451, oai:arXiv.org:hep-ph/0601013, (2004).

II *3D Simulations of 3D Silicon Radiation Detector Structures*, J. Kalliopuska, S. Eränen and R. Orava, Nuclear Instruments and Methods in Physics Research Section A: Accelerators, Spectrometers, Detectors and Associated Equipment. Vol. 568 No: 1, 27 - 33, doi:10.1016/j.nima.2006.07.015, (2006).

III *Charge Collection Characterization of a 3D Silicon Radiation Detector by Using 3D Simulations*, J. Kalliopuska, S. Eränen and R. Orava, Nuclear Instruments and Methods in Physics Research Section A: Accelerators, Spectrometers, Detectors and Associated Equipment. Vol. 572 No: 1, 292 - 296, doi:10.1016/j.nima.2006.10.370, (2007).

IV *Silicon Semi 3D Radiation Detectors*, S. Eränen *et al.* with J. Kalliopuska, IEEE Nuclear Science Symposium Conference Record, vol. 2, Rome, Italy, 16-22. Oct. 2004, 1231 - 1235, doi:10.1109/NSSMIC.2004.1462424, (2005).

V *Measurements and Simulations of 3D Silicon Radiation Detector Structures*, J. Kalliopuska and S. Eränen, Nuclear Instruments and Methods in Physics Research Section A: Accelerators, Spectrometers, Detectors and Associated Equipment. Vol. 568 No: 1, 22 - 26, doi:10.1016/j.nima.2006.07.014, (2006).

VI *Characterization of Semi 3-D Sensor Coupled to Medipix2*, L. Tlustos, J. Kalliopuska, R. Ballabriga, M. Campbell, S. Eränen and X. Llopart, accepted for publication in The Nuclear Instruments and Methods in Physics Research A in proceedings of the Imaging 2006, Stockholm, Sweden, June 2006.

Publication I: TOTEM Forward Measurements: Exclusive Central Diffraction

J. Kalliopuska, J.W. Lämsä, T. Mäki, N. Marola, R. Orava, K. Österberg, M. Ottela and S. Tapprogge

CERN-2005-014, DESY-PROC-2005-001, (2005), 448 - 451

The paper presents a first systematic analysis of the precision of the momentum measurement of protons produced in the central exclusive diffractive process. The accuracy of the reconstructed mass for the particle created in the process is based on measurements of leading proton momentum loss measurements. The measurement locations along the beam pipe were originally 215 m, 320 m and 420 m from the interaction point. The paper collects the relevant results of measurement locations at 215 m and 420 m. A mass resolution of the order of 1 GeV for the particle masses beyond 120 GeV is reported to be achievable.

The author of the thesis strongly contributed to the creation of the analysis method and did the analysis for the 420 m measurement location. He also participated in writing the original paper "Resolution studies of the leading proton measurement in exclusive central diffraction at LHC" published in HIP-2003-11/EXP (2003).

Publication II: 3D Simulations of 3D Silicon Radiation Detector Structures

J. Kalliopuska, S. Eränen and R. Orava

Nuclear Instruments and Methods in Physics Research Section A, vol. 568, (2006), 27 - 33

The paper reports the results of an electrical characterization of a rectangular 3D silicon detector structure using 3D TCAD simulation software. Topics reviewed include the 3D detector design, the 3D TCAD simulation software and the simulation setup for the 3D detector characterization. The study includes a comparison between the 2D and 3D quasi-stationary simulations and how the surface effects affect the electrical characteristics.

The author of the thesis wrote the paper, performed the simulations and analyzed the results using commercial 3D TCAD software. He presented the paper at the 10^{th} European Symposium on Semiconductor Detectors 2005, the "Elmau conference".

Publication III: Charge Collection Characterization of a 3D Silicon Radiation Detector by Using 3D Simulations

J. Kalliopuska, S. Eränen and R. Orava

Nuclear Instruments and Methods in Physics Research Section A, vol. 572, (2007), 292 - 296

The paper presents a study on the transient characteristics of the simulated 3D detector structure. The 3D simulations are used to assess the performance of a 3D detector structure in terms of charge sharing, efficiency and speed of charge collection, surface charge, location of the primary interaction and the bias voltage. The measured current pulse is proposed to be delayed due to the resistance-capacitance (RC) product induced by the variation of the serial resistance of the pixel electrode depending on the depth of the primary interaction. Extensive simulations are carried out to characterize the 3D detector structures and to

verify the proposed explanation for the delay of the current pulse. A method for testing the hypothesis experimentally is suggested.

The author of the thesis wrote the paper, performed the simulations and proposed that the charge collection characteristics of the 3D detectors depend on the internal RC constant. He gave the oral presentation at the 10^{th} Pisa Meeting on advanced detectors in 2006.

Publication IV: Silicon Semi 3D Radiation Detectors

S. Eränen *et al.* with J. Kalliopuska

IEEE Nuclear Science Symposium Conference Record, vol. 2, (2005), 1231 - 1235

The paper represents a novel semi-3D radiation detector structure, a fabrication process, a preliminary electrical characterization by measurements and simulations, and provides evidence on function and radiation hardness. The detector structures were fabricated on n-type Float Zone (FZ) and Czochralski (CZ) silicon substrates and the process was carried out at VTT. The structure has p-type vertical electrodes that extend from the top surface to various depths in the bulk. The bottom of the detector is uniformly covered by an n-doped electrode, and on the top surface above each vertical electrode is a p-type implant with various areas. The pixels are connected with aluminium to strips for electrical characterization.

The author of the thesis was involved in designing the detector structure, performed the electrical and transient simulations, and wrote part of the paper. He gave the oral presentation at the IEEE Nuclear science symposium and Medical imaging conference in 2005.

Publication V: Measurements and Simulations of 3D Silicon Radiation Detector Structures

J. Kalliopuska and S. Eränen

Nuclear Instruments and Methods in Physics Research Section A, vol. 568, (2006), 22 - 26

The paper gives more detailed measurement and simulation results of the fabricated semi-3D structures. Electrical characteristics such as IV and CV curves are measured in an improved measurement setup, and an order of magnitude better results are obtained for both capacitance and current than was represented in publication **IV**. The measurements are compared with the simulations and are shown to give similar results.

The author of the thesis has wrote the paper, performed the simulations and measurements, and gave the presentation at the 10^{th} European Symposium on Semiconductor Detectors in 2005, the "Elmau conference".

Publication VI: Characterization of Semi 3-D Sensor Coupled to Medipix2

L. Tlustos, J. Kalliopuska, R. Ballabriga, M. Campbell, S. Eränen and X. Llopart

Nuclear Instruments and Methods in Physics Research Section A, accepted for publication, (2007)

The paper describes the characterization of a 300 μm thick semi-3D sensor coupled to a Medipix2 readout chip. It reports measured bonding quality by using a ^{90}Sr-source, comparative measurements with respect to a standard planar 300 μm silicon sensor comprising IV-curves, depletion voltage and energy resolution. In addition, the uniformity of the pixel response has been measured using a pulsed 1060 nm laser. The capabilities of the semi-3D sensor to be used in X-ray imaging were demonstrated with a slit mask image taken with a W-target X-ray tube – a filter of 2.5 mm Al and a tube voltage of 35 kV.

The author of the thesis is the second writer of the paper, performed the 3D simulations and participated in the analysis of the experimental results.

Chapter 1

Large Hadron Collider

The European Organization for Nuclear Research (CERN) was founded in 1954 and is one of the leading research centers for high energy physics in the world. The laboratory aims to discover new physics and test the current theories by building accelerators with top performance. It has gone through several development stages during its existence, from the first synchro-cyclotron to invention of the proton-antiproton collider SPS and to the currently stripped Large Electron Positron (LEP) collider. The latest upgrade, the Large Hadron Collider (LHC), will be completed in 2007 and will start the first physics runs in 2008.

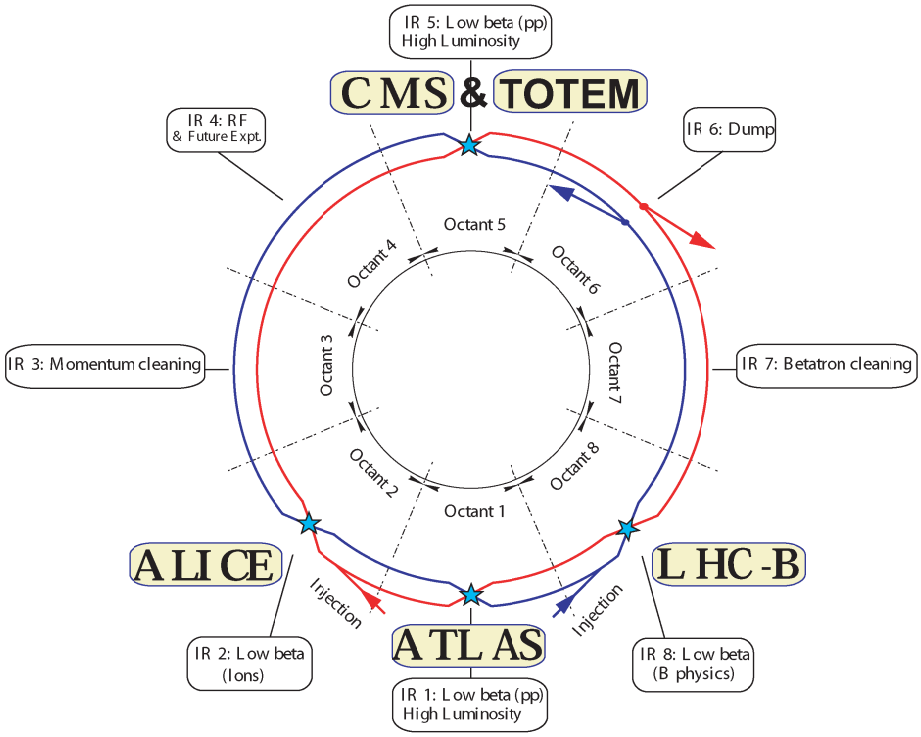

Figure 1. LHC accelerator and experiments.

The LHC is a two-ring superconducting accelerator aiming at the discovery of the Higgs

particle for masses up to $\sim 1\,\text{TeV}$ and the study of rare events. The collider is installed in the 27 km long LEP collider tunnel and is able to function with collision energies up to 14 TeV[1] and luminosities up to $\mathcal{L} = 10^{34}\ \text{cm}^{-2}\text{s}^{-1}$ [1]. The LHC is designed as a proton-proton (pp) collider with separate magnet fields and vacuum chambers in the main arcs and with common sections only at the insertion regions where the experimental detectors are located. To keep the LHC particle beams on track with peak beam energies of 7 TeV, cryogenic superconducting dipole magnets operating at 1.9 K, with a peak magnetic field of 8.36 T, are required. Fig. 1 illustrates the LHC configuration and the associated main experiments.

1.1 LHC experiments

The LHC has two high luminosity experiments, ATLAS [2] and CMS [3], operating at a peak luminosity of $10^{34}\ \text{cm}^{-2}\text{s}^{-1}$. The high luminosity operation is required to obtain enough events, associated with the Higgs boson, over the huge hadronic background in the central experiments. Both of the detector systems contain subsystems which are designed to measure the energy and momentum of photons, electrons, muons, and other products of the collisions. The innermost layer is a silicon-based tracker for measuring the momentum of each charged particle. It is enclosed by scintillating crystals of electromagnetic and hadron calorimeters to measure the energies carried by the produced particles. Around the tracker and calorimeters are a magnet system and a muon detector that return the magnetic field and track muons, respectively. Fig. 2 represents the onion-like construction of the CMS detector and illustrates the particle tracks inside it. The ATLAS detector has a similar architecture, except that the outer magnets are toroidal. It should be noted that the muons always escape the detector.

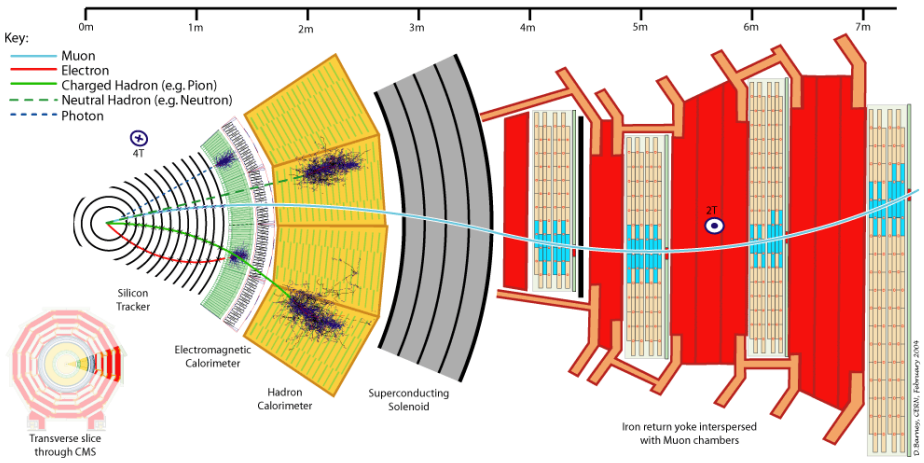

Figure 2. A slice of the CMS detector showing how different particles are observed in the detector [3].

The LHC has two low luminosity experiments. The LHCb experiment [4] aims at a peak luminosity of $10^{32}\ \text{cm}^{-2}\text{s}^{-1}$ for studying the B-physics. The TOTEM experiment [5] is

[1] In a center of mass coordinates

	Unit	Value
Luminosity, $\mathcal{L}$	$\mathrm{cm}^{-2}\mathrm{s}^{-1}$	10^{34}
Beam energy	TeV	7
Magnetic dipole field	T	8.36
Protons per bunch, N_b		1.1×10^{11}
Bunch crossing interval	ns	25
Beam current	A	~ 0.5
β^*	m	0.5
Beam crossing angle, Θ_c	μrad	300

Table 1. Nominal LHC machine parameters at high luminosity operation (CMS & ATLAS).

designed to detect protons from the elastic scattering at small angles and it extends the detection range of the CMS very close to the proton beams. It will operate at a peak luminosity close to 2×10^{29} $\mathrm{cm}^{-2}\mathrm{s}^{-1}$ with 156 proton bunches. In addition to the proton beams, the LHC will also be operated with ion beams. The LHC has one dedicated ion experiment ALICE [6] aiming at a peak luminosity of 10^{27} $\mathrm{cm}^{-2}\mathrm{s}^{-1}$ for nominal Pb-Pb ion operation [1].

1.2 LHC properties

The exploration of rare events in LHC collisions at the interaction points (IP) requires both high beam energies and high beam lumnosities (intensities). This is obtained with a large number of bunches, up to 2808 for each proton beam and each bunch containing 1.1×10^{11} protons, and a nominal bunch spacing of 25 ns. A summary of the LHC nominal operation parameters is given in Tab. 1.2.

The number of events per second (interaction rate) generated in the LHC collisions is given by Eq. 1.

$$N_{event} = \mathcal{L}\sigma_{event}, \tag{1}$$

where $\sigma_{event}\,[\mathrm{cm}^{-2}]$ is the cross-section for the event under study and $\mathcal{L}\,[\mathrm{cm}^{-2}\mathrm{s}^{-1}]$ the machine luminosity.

The luminosity is defined only by the beam parameters and can be written for a Gaussian beam distribution as shown in Eq. 2.

$$\mathcal{L} = \frac{N_b^2 n_b f_{rev} \gamma_r}{4\pi\epsilon_n \beta^*} F, \tag{2}$$

where N_b is the number of particles per bunch, n_b is the number of bunches per beam, f_{rev} is the revolution frequency, γ_r is the relativistic gamma factor, ϵ_n is the normalized transverse beam emittance, β^* is the beta function at the collision point, and F is the geometric luminosity reduction factor due to the crossing angle at the IP, given by

	Unit	Phase 0	Phase 1	Phase 2
Luminosity, $\mathcal{L}$	$\mathrm{cm}^{-2}\mathrm{s}^{-1}$	2.3×10^{34}	9×10^{34}	10^{35}
Beam energy	TeV	7.45	~ 7	14
Magnetic dipole field	T	9	9	$16.5 \pm 1 - 2$
Protons per bunch, N_b		1.7×10^{11}	1.7×10^{11}	$> 1.7 \times 10^{11}$
Bunch crossing interval	ns	25	12.5	12.5
Beam current	A	~ 0.85	~ 1	~ 1
β^*	m	0.5	0.25	0.25
Beam crossing angle, Θ_c	μrad	300	424	424

Table 2. SLHC machine parameters in high luminosity operation at different phases of the upgrade.

$$F = 1/\sqrt{1 + (\frac{\Theta_c \sigma_z}{2\sigma^*})^2}, \tag{3}$$

where Θ_c is the full crossing angle at the IP, σ_z is the Root Mean Squared (RMS) bunch length and σ^* is the transverse RMS beam size at the IP [1].

1.3 Super-LHC

After a few years of running at the maximum luminosity achievable with the LHC, upgrades are foreseen to increase its luminosity and collision energy, and thereby extend the physics reach. The physics potential of the upgraded LHC, henceforth referred to as Super-LHC (SLHC), is discussed later in 3.4 [7].

The SLHC aims at a target luminosity in proton operation of 10^{35} $\mathrm{cm}^{-2}\mathrm{s}^{-1}$ in CMS and ATLAS, and an upgrade of the centre of mass energy to 28 TeV. Three stages in the upgrading process are proposed:

- **Phase 0:** maximum performance without hardware changes to the LHC.
- **Phase 1:** maximum performance while keeping the LHC arcs unchanged (possibility to obtain the aim luminosity).
- **Phase 2:** maximum performance with major hardware changes to the LHC (mainly aims at energy upgrade).

The accelerator high luminosity operation parameters in each upgrade phase towards the SLHC are given in Tab. 1.3 – for comparison see Tab. 1.2 for the nominal LHC parameters.

The steps required to reach the maximum performance without hardware changes to the accelerator (**Phase 0**) are:

- Collide beams only in IP1 and IP5.

- Increase the bunch population up to the beam-beam limit of 1.7×10^{11} protons per bunch, resulting in a luminosity of 2.3×10^{34} cm^{-2}s^{-1}.
- Increase the main dipole field to 9 T, resulting in maximum proton energy of 7.54 TeV.

Increasing the LHC luminosity with hardware changes only in the LHC insertions and/or in the injector complex (**Phase 1**) includes the following steps:

- Modify the insertion quadruples and/or layout to yield a $\beta^* = 0.25$ m from the nominal 0.5 m.
- Increase the crossing angle by $\sqrt{2}$ to 424 μrad from the nominal 300 μrad, see Eq. 3.
- Increase the bunch population up to the ultimate intensity of 1.7×10^{11} protons per bunch, resulting in a luminosity of 3.3×10^{34} cm^{-2}s^{-1}.
- Halving the bunch length with a new high-harmonic RF system would increase the luminosity to 4.7×10^{34} cm^{-2}s^{-1}.
- Increase the LHC luminosity based on very long "super-bunches". A 300-m long super-bunch in each of the LHC rings would be compatible with the beam-beam limit, and the luminosity could be increased up to 9×10^{34} cm^{-2}s^{-1}.

Finally, possible steps to increase the LHC performance with major hardware changes in the LHC arcs and/or in the injectors (**Phase 2**) include:

- Modification of the injectors and provisioning of the pre-accelerator with superconducting magnets and injection of protons into the LHC at 1 TeV with a very high brilliance value.
- Installation of new superconducting dipoles in the LHC arcs to reach a beam energy of 14 TeV. Procurement of magnets with a nominal dipole field of between 16 and 16.5 T, providing a safety margin of 12 T. Could operate by 2015.

Chapter 2

Standard Model

The Standard Model (SM) of particle physics [8, 9], developed in the beginning of 1970, is a theory that describes elementary particles of matter and the interactions between them. It is a quantum field theory, and is consistent with both quantum mechanics and special relativity. The SM is currently the best known model for describing the universe and almost all experimental tests of the three forces described by it have agreed with its predictions[1]. The only unconfirmed part of the model is the Higgs mechanism.

The SM contains both fermionic and bosonic fundamental particles and their antiparticles [10, 11]. Fermions are particles that possess half-integer spin and obey the Pauli Exclusion Principle, i.e. fermions have an antisymmetric wave function and cannot share the same quantum state. Bosons possess integer spin and symmetric wave function and thus do not obey the Pauli Exclusion Principle. Particles composed of a number of other particles can be either fermions or bosons, depending on their total spin.

2.1 Fermions

The fermions in the SM are matter particles and are classified into quarks (q) and leptons (l). They come in three mass and flavor dependent generations, presented in Tab. 2.1.

Each generation is divided into two quarks and two leptons. The two quarks may be divided into one with charge +2/3 (up-type) and one with charge -1/3 (down-type); the two leptons may be divided into one with electric charge -1 (electron-like) and one neutral (neutrino). The electron and all the neutrinos are stable. The muon and tau have lifetimes of $\tau_\mu = 3 \times 10^{-6}$ s and $\tau_\tau = 3 \times 10^{-13}$ s, respectively, and can decay into lighter leptons and sometimes into quarks and antiquarks.

Quarks are combined together into color-neutral hadrons and they are further divided into two groups of particles: baryons and mesons. Baryons have half-integer spin and are a bound state of three quarks (qqq) or three antiquarks ($\bar{q}\bar{q}\bar{q}$). Mesons have integer spin and are bound states of quark and antiquark ($q\bar{q}$) [12].

[1] In high energy physics the natural units that have dimension of energy are often preferred to the SI units. In natural units, the fundamental constants are chosen to be $c = \hbar = 1$. If the energy unit of GeV is considered, from basic equations of energy $E = pc = mc^2$, it follows that $[p] = GeV$ and $[m] = GeV$, and from $E = 2\pi\hbar c/\lambda$, it follows that $[length] = GeV^{-1}$. The unit of time, $[time] = GeV^{-1}$, is obtained from $x = ct$. For a cross-section, the unit becomes $[\sigma] = GeV^{-2}$.

	1^{st}Generation		2^{nd} Generation		3^{rd} Generation	
Charge	Flavor	Mass	Flavor	Mass	Flavor	Mass
$+2/3$	Up (u)	$3 \cdot 10^{-3}$	Charm (c)	1.3	Top (t)	175
$-1/3$	Down (d)	$6 \cdot 10^{-3}$	Strange (s)	0.1	Bottom (b)	4.3
-1	Electron (e)	$5 \cdot 10^{-4}$	Muon (μ)	0.106	Tau (τ)	1.777
0	neutrino (ν_e)	$< 10^{-8}$	neutrino (ν_μ)	$< 2 \cdot 10^{-4}$	neutrino (ν_τ)	< 0.02

Table 3. Three generations of the elementary particles in the SM and their associated electric charges and masses in GeV/c^2. Each fermion in the table has a spin of $+1/2$.

2.2 Interactions in the Standard Model

The bosons in the SM are the intermediate interaction particles (force carriers). Excluding the gravitational interaction, all relevant interactions are mediated by the exchange of bosons: photons (γ) for the electromagnetic interaction, $W^\pm$ and Z^0 bosons for the weak interaction and eight species of gluons for the strong interaction. The properties of these bosons of the fundamental interactions are described in Tab. 2.2 [13, 14].

Force	Boson	Mass	Range	Strength
Strong (Nuclear)	8 gluons (g)	Massless	Infinite ($\sim 10^{-15}$ m)	~ 1
Electromagnetic	Photon (γ)	Massless	Infinite	$\sim 10^{-3}$
Weak interaction	W boson ($W^\pm$) Z boson (Z^0)	$M_W = 80.42$ GeV $M_Z = 91.18$ GeV	$\sim 10^{-18}$ m	$\sim 10^{-5}$
Gravity	Graviton (G)	Massless	Infinite	$\sim 10^{-38}$

Table 4. Interactions in the SM and their range and relative strengths at the length of an atomic nucleus (an effective length of nuclear force, $\sim 10^{-15}$ m).

The electromagnetic force acts on charged particles and allows atoms to bond and form molecules. The photon is massless, chargeless, non-self-interacting and has an infinite range.

The weak interaction is carried by massive charged $W^\pm$ and neutral Z^0 bosons and thus the range of the interaction is roughly the size of a quark ($\sim 10^{-18}$ m). The strength of the force decreases rapidly beyond the quark size. The weak interactions act on fermions and are responsible for the radioactive decay of massive fermions. The massive weak force carriers are highly unstable and decay within 10^{-23} s into a lepton and antilepton or a quark and an antiquark.

The strong force acts on quarks and holds them together to form the color-neutral hadrons. The strong interaction is mediated by eight gluons (g) that are massless, electrically neutral and carry a color quantum number. There are eight gluons since they come in eight different colors. The consequence of the gluons being colorful is that they cannot be observed as isolated free particles and they interact not just with the quarks but also with themselves.

The nuclear force is a residual effect of strong and electromagnetic interactions and has the property of asymptotic freedom at infinitely short distances, i.e. the strength of the nuclear force goes to zero at short distances (quarks behave as free particles) and increases as the quarks are being separated [15]. When one tries to separate quarks or gluons, their binding energy increases until it reaches the energy where a new $q\bar{q}$ pair or $g\bar{g}$ pair is produced.

The gravitational interaction is not included in the SM because its strength differs greatly from the other fundamental interactions. A description of a graviton that mediates the gravitation is given in [16].

2.3 Theoretical aspect of the Standard Model

As for the theoretical aspects, the Standard Models is a quantum field theory that is based on the gauge symmetry $SU(3)_C \times SU(2)_L \times U(1)_Y$[2]. This gauge group includes the symmetry group of the strong interactions, $SU(3)_C$ (color symmetry), and the symmetry group of the electroweak interactions, $SU(2)_L \times U(1)_Y$ (weak isospin symmetry). The Lagrangian of each set of mediating bosons in the SM is required to be invariant under a local gauge transformation[3] to guarantee that the values of the physical measurable quantities do not change [17].

The strong interaction of three color charge carrying quarks (q) and their antiquarks ($\bar{q}$) is described by the theory called Quantum ChromoDynamics (QCD). The QCD introduces eight intermediate massless particles (gluons) that are the gauge bosons of the color symmetry group $SU(3)_C$. A basis for the calculations is given by the gauge invariant QCD Lagrangian[4], written as

$$\mathcal{L} = \bar{q}(i\gamma^\mu \partial_\mu - m)q - g(\bar{q}\gamma^\mu T_a q)G^a_\mu - \frac{1}{4}G^a_{\mu\nu}G^{\mu\nu}_a. \tag{4}$$

The Dirac four-spinors q and $\bar{q}$ correspond to the (three) quark and antiquark color fields, respectively, G^a_μ are the (eight) vector gauge gluon fields, $\{T_a \,|\, a = 1, ..., 8\}$ is a set of linearly independent traceless 3×3 matrices, and γ^μ are the Dirac gamma matrices. The field strength tensor $G^a_{\mu\nu}$ is defined as

$$G^a_{\mu\nu} = \partial_\mu G^a_\nu - \partial_\nu G^a_\mu - g f_{abc} G^b_\mu G^c_\nu, \tag{5}$$

where g is a coupling constant of the interacting quarks and gluons and f_{abc} are real structure constants of the group defined from the commutation of T_a

$$[T_a, T_b] = i f_{abc} T_c. \tag{6}$$

In the weak isospin symmetry group $SU(2)_L \times U(1)_Y$, the γ, $W^\pm$ and Z^0 are the four gauge bosons. The group symmetry of the electromagnetic interactions, $U(1)_{em}$, appears

[2] In the gauge symmetry groups the C stands for color, L for lepton isospin and Y for hypercharge.

[3] The local gauge transformation in 1-D is given by $\psi(x) \rightarrow e^{i\alpha(x)}\psi(x)$, where $\alpha(x)$ depends on space and time in a completely arbitrary way.

[4] Classically the Lagrangian (L) is a separation of kinetic (T) and potential (V) energies of the system, $L \equiv T - V$, and it can be obtained as a space integral of the Lagrangian density ($\mathcal{L}$), $L = \int \mathcal{L}\, d^3x$. A common practice is to call $\mathcal{L}$ itself the Lagrangian.

in the SM as a subgroup of $SU(2)_L \times U(1)_Y$ and it is in this sense that the weak and electromagnetic interactions are unified [15]. The Lagrangian for the electroweak interactions is much more complicated than the one for the QCD, but similar terms can be identified as in Eq. 4. The Lagrangian embodies the weak isospin and hypercharge interactions, and the kinetic energy and self-coupling of the (three) vector boson fields W_μ and the kinetic energy of the fourth vector boson field B_μ [17]. Masses of the gauge bosons of the weak interaction, as well as the masses of the leptons and fermions, are obtained via the Higgs mechanism as explained below.

The strength of the interactions is given by the size of coupling constants[5]. The dependence of the physical charge, which is measured experimentally, on the Q^2 (interaction energy) of the experiment is referred to as the "running coupling constant" [17]. This is presented for the strong interaction in Fig. 3 [18].

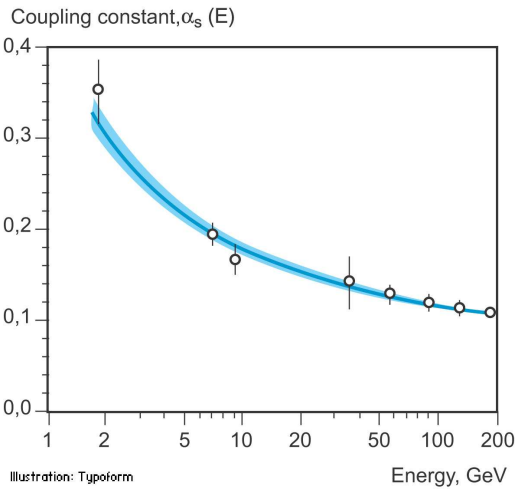

Figure 3. The value of the running coupling constant", α_S, as a function of the energy scale $E\,(=Q)$. The curve that slopes downwards is a prediction of the asymptomatic freedom in QCD and it agrees very closely with the measurements (dotted) [18].

For the electromagnetic interactions, described by quantum electrodynamics (QED), the physical charge is $e(Q^2)$ and the dependence of the coupling constant is defined as $\alpha_{em}(Q^2) \equiv e^2(Q^2)/4\pi$ [17]. At low energies, this reduces to the familiar form of the fine structure constant

$$\alpha_{em}(Q^2 = M_e^2) = \frac{e^2}{4\pi} = \frac{1}{137}, \tag{7}$$

where e is the elementary charge and M_e is the electron rest mass. In the large Q^2 limit the interaction is expressed as

[5]The values of the coupling constants depend on the interaction energy and are constant only at fixed values of Q^2, where $Q^2 \equiv -q^2 = \mu^2$ and q^2 is the four momentum transfer and μ is the renormalization or reference momentum.

$$\alpha_{em}(Q^2) = \frac{\alpha_{em}(\mu^2)}{1 - \frac{\alpha_{em}(\mu^2)}{3\pi}\log(\frac{Q^2}{\mu^2})}. \tag{8}$$

The name of strong interactions is due to their comparativelty stronger strength than the other interactions. The strength is governed by the size of the strong coupling constant g or equivalently $\alpha_S(Q^2) = \frac{g^2(Q^2)}{4\pi}$. The QCD "running coupling constant" is given by

$$\alpha_S(Q^2) = \frac{12\pi}{(33 - 2n_f)\log(\frac{Q^2}{\Lambda^2})}, \tag{9}$$

where n_f is the number of quark flavors at energy Q^2 and Λ^2 is a free parameter defined from values of μ as

$$\Lambda^2 = \mu^2 \exp\left[\frac{-12\pi}{(33 - 2n_f)\alpha_S(\mu^2)}\right]. \tag{10}$$

Values of Eq. 9 vary from large values for low energies, $\alpha_S(Q^2 = M^2_{hadron}) \sim 1$, up to the vanishing asymptotic limit, $\alpha_S(Q^2 \to \text{inf}) \to 0$. This last limit indicates that the quarks behave as free particles when they are observed at infinitely large energies and it is known as the property of asymptotic freedom. The free parameter Λ^2 describes the Q^2 scale where the coupling becomes large and it can not be predicted by theory, but the numerical value has been measured to lie in between 0.1 and 0.5 GeV [17].

The weak interactions at energies much lower than the exchanged gauge boson mass, $Q^2 \ll M^2_{\mathrm{W}}$, has a weak coupling constant g from

$$\frac{G_F}{2} = \frac{g^2(Q^2)}{8M^2_{\mathrm{W}}}, \tag{11}$$

where the effective (weak) strength is given by the dimensionful Fermi constant $G_F = 1.167 \times 10^{-5}\, GeV^{-2}$. The SM coupling constant relations of electroweak interactions are

$$g(Q^2)\sin\Theta_{\mathrm{W}} = g'(Q^2)\cos\Theta_{\mathrm{W}} = e(Q^2), \tag{12}$$

where Θ_{W} is the weak mixing angle that is defined below. The electromagnetic interaction (a $U(1)_{em}$ gauge symmetry with coupling $e(Q^2)$) is between the weak isospin (an $SU(2)_L$ symmetry with coupling $g(Q^2)$) and weak hypercharge (a $U(1)_Y$ symmetry with coupling $g'(Q^2)$) interactions. As the parameter Θ_{W} is to be determined by experiment, the couplings $g(Q^2)$ and $g'(Q^2)$ can be replaced by $e(Q^2)$ and Θ_{W} [17].

2.4 Grand Unification

At higher energy scales, beyond the electroweak energy scale of the order of 100 GeV, the SM becomes insufficient and unsatisfactory [19]. As gravity is not included in the SM, it

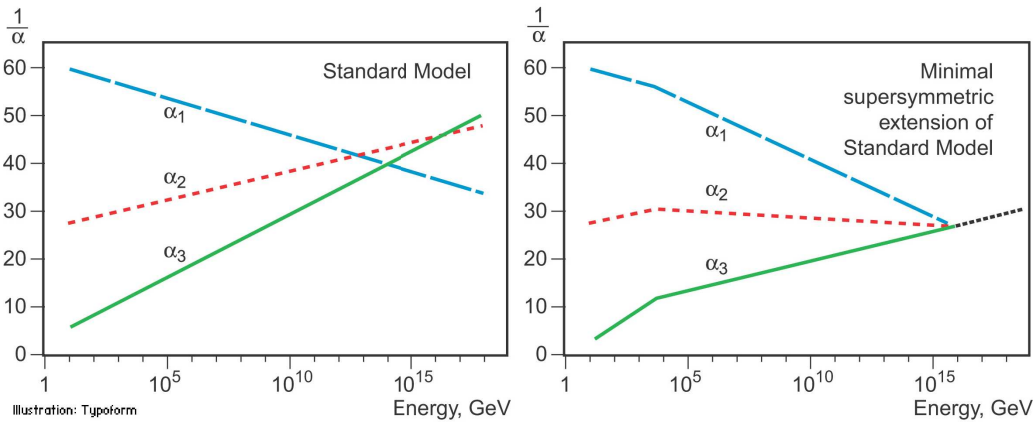

Figure 4. Running coupling constants in the SM (left) and with the introduction of supersymmetry (right). In the SM the three lines, which show the inverse value of the coupling constant for the three fundamental forces, do not meet at one point, but with the introduction of supersymmetry they do [18].

cannot describe phenomena at the Planck energy scale of 10^{19} GeV where gravity becomes significant.

The aim of particle physics is to describe the elementary particles and their interactions with one unified theory. In the Grand Unified Theory (GUT), the symmetry groups of the SM ($SU(3)_C \times SU(2)_L \times U(1)_Y$) would become sub-groups of a larger grand unified group. At sufficiently high energies, all three fundamental interactions would be described by one coupling constant g_G [19].

In the SM, the unification of the coupling constants does not happen as they are extrapolated to high energies, as can be seen in Fig. 4(left). One possibility is to introduce a supersymmetric GUT that presents a new set of particles, so-called supersymmetric particles. In this model the electroweak and strong coupling constants meet at an energy of roughly of 10^{16} GeV, as shown in Fig. 4(right) [18].

Chapter 3

Higgs sector

The fact that weak gauge bosons are massive particles, indicates that $SU(2)_L \times U(1)_Y$ is not a symmetry of the vacuum. In contrast, the photon being massless reflects that $U(1)_{em}$ is a good symmetry of the vacuum. Therefore, the Spontaneous Symmetry Breaking (SSB) pattern in the SM must be: $SU(3)_C \times SU(2)_L \times U(1)_Y \rightarrow SU(3)_C \times U(1)_{em}$ [15].

3.1 The Higgs mechanism

The masses of the heavy weak bosons and the above pattern are implemented in the SM by means of the Higgs mechanism. It adds a doublet of two complex scalar Higgs fields, Φ, into the SM theory and introduces a massive Higgs boson particle H^0, and according to the SSB of the Higgs field, this must be scalar, spin-0 and electrically neutral [12, 15].

The Higgs Lagrangian is defined using the Higgs field as

$$\mathcal{L}_{Higgs} = (\partial_\mu \Phi)^\dagger (\partial^\mu \Phi) - \mu^2 \Phi^\dagger \Phi - \lambda (\Phi^\dagger \Phi)^2, \tag{13}$$

where the negative part is the Higgs potential, V_{Higgs}. The value of λ must be positive to keep the energy of the vacuum bounded from below and the value of μ^2 can be either positive or negative. To introduce SSB in a simple fashion, the value of μ^2 is chosen to be negative and the minimum of the Higgs potential is found at $-\mu^2/\lambda \equiv v^2$. The value v is defined to be the vacuum expectation value of the Higgs field as $|\Phi|_0 = v = \sqrt{-\mu^2/\lambda}$. At tree level, the mass terms are obtained from the Higgs Lagrangian by expanding V_{Higgs} around v and then substituting the expansion of the Higgs field [1] into Eq. 13.

The following mass terms can be identified from the Lagrangian at the tree level:

- The heavy weak boson masses, $M_{\mathrm{W}} = \frac{gv}{2}$ and $M_{\mathrm{Z}} = \frac{\sqrt{g^2+g'^2}v}{2}$, where g and g' are the weak isospin and hypercharge coupling constants, respectively.
- The Higgs boson mass as $M_{\mathrm{H}} = \sqrt{2}\mu$.

[1] The Higgs field expansion is given in the form $\Phi_v \sim v + h(x)$, where the value of the Higgs field depends on the function $h(x)$ around v.

The vacuum expectation value v has been determined experimentally using μ-decay results ($\mu \to \nu_\mu \bar{\nu}_e e$) and theory:

$$\frac{G_F}{\sqrt{2}} = \frac{g^2}{8M_{\mathrm{W}}^2} = \frac{1}{2v^2} \Rightarrow v = (\sqrt{2}G_F)^{-\frac{1}{2}} = 246\,\mathrm{GeV}. \tag{14}$$

The existence of the Higgs field can be summarized to have three main consequences:

1. The $W^\pm$ and Z^0 bosons can acquire masses in the ratio $\frac{M_{\mathrm{W}}}{M_{\mathrm{Z}}} = \cos\Theta_{\mathrm{W}}$, where Θ_{W} is the weak mixing angle.

2. There are electrically neutral quanta H^0 (Higgs bosons) associated with the Higgs field.

3. Interactions with the Higgs field generates lepton and fermion masses. The mass emerges from the interactions of the gauge fields with the non-zero vacuum expectation value of the Higgs field, v, as well as from interactions with the H^0. The mass of each fermion is determined by the corresponding dimensionless Higgs coupling constant, $g_{\mathrm{H}} = (\sqrt{2}G_F M_{\mathrm{f}}^2)^{1/2}$, where M_{f} is the fermion mass [12].

The SM is not able to predict the mass of the Higgs boson and it is as yet unobservable. The non-observation of a Higgs boson signal by the Tevatron and Large Electron Positron (LEP) accelerators imply an experimental lower bound of the Higgs mass of 114.4 GeV at the 95% confidence level (CL).

The mass of the top quark, M_{t}, is a free parameter of the SM and it is correlated to other parameters of the SM via electroweak corrections. By measuring the top quark mass together with the W boson mass, M_{W}, it is possible to make predictions about the mass of the SM Higgs boson. The parameter ρ of the SM relates the W and Z boson masses and the weak mixing angle Θ_{W} as

$$\rho = \frac{M_{\mathrm{W}}^2}{M_{\mathrm{Z}}^2 \cos^2\Theta_{\mathrm{W}}} \equiv 1 + \Delta r, \tag{15}$$

where Δr is a radiative correction term. In perturbation theory it is at first order

$$\Delta r = \frac{3G_F}{8\pi^2\sqrt{2}} M_{\mathrm{t}}^2 + \frac{\sqrt{2}G_F}{16\pi^2} M_{\mathrm{W}}^2 \left(\frac{11}{3} \ln\left(\frac{M_{\mathrm{H}}^2}{M_{\mathrm{W}}^2} \right) + \ldots \right) + \ldots \tag{16}$$

The correction depends quadratically on the top quark mass ($\Delta r \propto M_{\mathrm{t}}^2$) , but only logarithmically on the Higgs boson mass ($\Delta r \propto \ln(M_{\mathrm{H}}/M_{\mathrm{W}})$). The top quark mass dominats the corrections to electroweak processes [20].

Precision measurement of M_t and M_W constrains the mass of the SM Higgs boson, as shown in Fig. 5. Precision measurements of electroweak observables, using an updated measurement of the t quark and W boson masses, indicate that the SM Higgs boson mass has an upper bound of 153 GeV at the 95% CL [21]. Fig. 5 illustrates world average measurements in 2007 of the W boson and t quark masses at the 68% CL. The intersection of the blue ellipse (most likely masses of W and t) with the green band (a single Higgs boson mass) indicates the most likely Higgs boson mass to be about at 115 GeV. It is fascinating

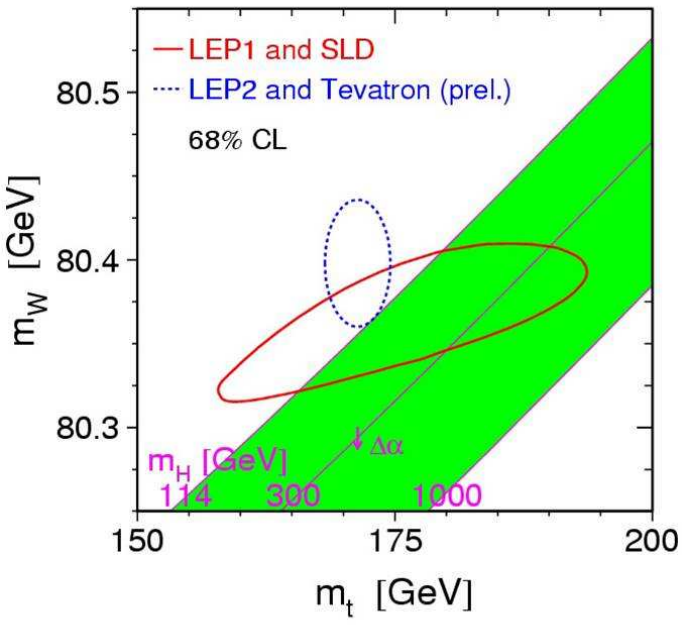

Figure 5. Measured masses (world average) of the W boson and top quark. The blue ellipse shows the most likely values for the masses, based on all available experimental information at the 68% confidence level. Illustration of the Higgs boson mass as a function of top quark and W-boson mass. Each diagonal line represents a single Higgs boson mass; examples chosen are $M_H = 114$, 300 and 1000 GeV. The intersection of this ellipse with the green band indicates the most likely Higgs boson mass [22].

that the upper bound (with 68% CL) coincides with the experimentally excluded lower bound and, moreover, hints of the Higgs signal at 115 GeV were observed at CERN before the LEP shut down in 2002.

Still, experimental evidence of the SM Higgs is lacking and the model remains only a hypothesis. Even if the Higgs mechanism is proven to be right, there is still no answer to many fundamental questions, like the origin of generations, values of the fundamental constants, and the representation of gravity.

3.2 Super symmetry

Super symmetry (SUSY) predicts that for every known particle there is a superparticle partner equal in charge but different in other ways, for example in mass. SUSY postulates a relationship between matter particles (fermions, spin-1/2) and force carriers (bosons, integer spin), which is not present in the SM. It can also encompass the spin-2 fields of Einstein gravity, the gravitons [17]. Each SM fermion has a superpartner of spin-0 and each SM boson a spin-1/2 superpartner.

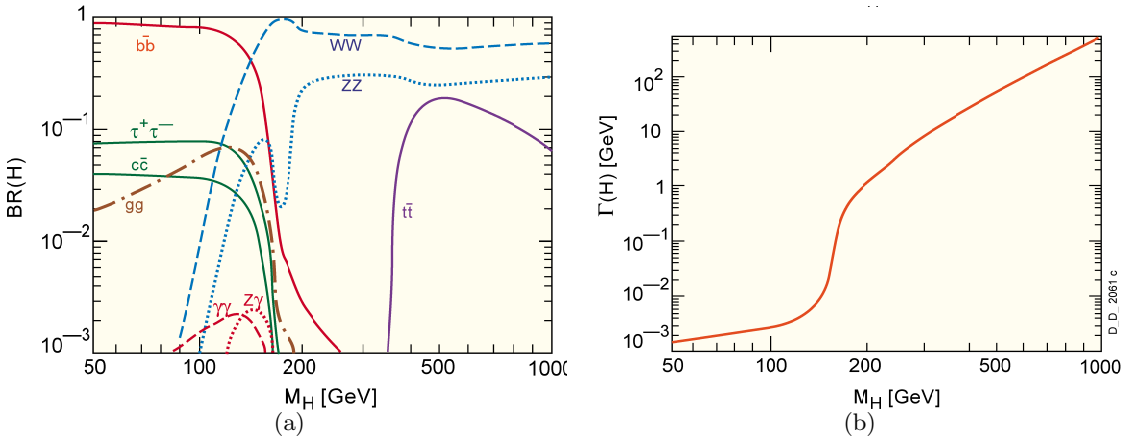

Figure 6. Branching ratios (a) and total decay width in GeV (b) of the SM Higgs boson as functions of the Higgs mass [24].

3.2.1 Extensions of the Higgs sector

The Higgs sector is extended most straightforward by adding another complex Higgs field into the SM theory. Similarly to the Higgs mechanism, two vacuum expectation values, v_1 and v_2, are obtained in the ratio

$$\tan\beta = \frac{v_2}{v_1}. \tag{17}$$

It defines the relative contributions of the two doublets in the physical Higgs bosons and their couplings.

Instead of the one physical Higgs boson in the SM, in the supersymmetric models the Higgs sector contains at least five physical Higgs bosons. The simplest example is the Minimal Supersymmetric Standard Model (MSSM), with the two Higgs fields. It consists of two charged ($H^{\pm}$) and three neutral (h, H, A) states for Higgs, where (h, H) are CP-even and (A) is CP-odd. The properties of the Higgs sector in the MSSM are characterized by the values of two independent parameters, typically chosen to be the pseudoscalar Higgs boson mass, m_A, and the ratio of Eq 17. The pseudoscalar A does not couple to the gauge bosons and its couplings to down-type fermions are directly proportional to $\tan\beta$ (couplings to up-type fermions inversely proportional to $\tan\beta$). Within the MSSM, the mass of the h-boson is bounded to $m_h < 135$ GeV and the experimental (with the confidence level of 95 %) lower limit for a neutral scalar Higgs is $m_h \simeq m_A \sim 92$ GeV [23].

3.3 Light Higgs boson detection in the LHC

The high luminosity experiments are mainly designed to find the traces of the possible Higgs sector and its extensions. The thesis considers only the finding of the light Higgs boson whose mass is between 80 GeV and 130 GeV.

The field of Higgs physics is broad. The Higgs bosons produced in the collisions can decay directly into pairs of massive particles or pairs of massless gluons and photons. Fig. 6(a)

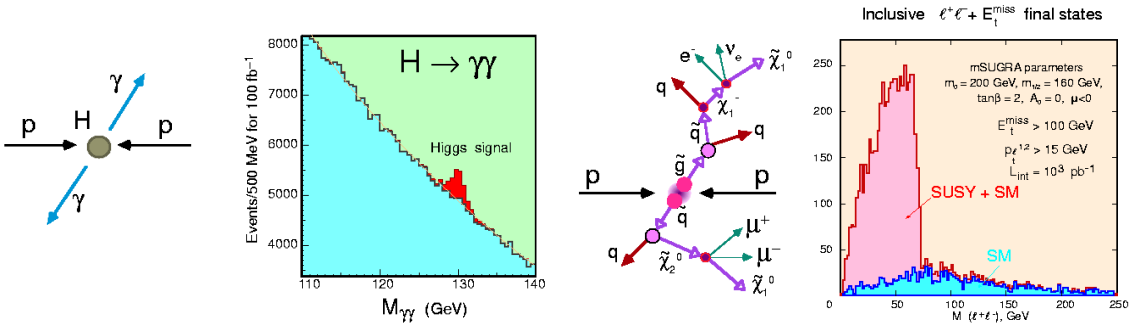

(a) (b)

Figure 7. (a) Exclusive light Higgs boson decay into two photons and (b) a SUSY event with 3 leptons and two jets, and their possible Higgs signals and backgrounds observed in CMS or ATLAS.

shows the different SM Higgs boson decay channels (decay probabilities) in the Higgs mass range from 100 GeV to 750 GeV. Fig. 6(b) shows the total decay width of Fig. 6(a). When the SM Higgs mass exceeds 140 GeV and the W^+W^- decay channel begins to dominate the decay process, the total decay width increases substantially and reach values above 1 GeV.

Even though the $b\bar{b}$ decay channel of the light SM Higgs boson has the largest branching ratio from Fig. 6(a), the Higgs detection in the central LHC detectors (CMS and ATLAS) is most promising via the $H \to \gamma\gamma$ channel, because the other decay channels are associated with large backgrounds of QCD jets. The photons can be detected by electromagnetic calorimeters, which are optimized to measure the energies and angles of such photons with high precision. The detection of the Higgs signal is still not straightforward due to background effects. The cross-section for the background effects compared to inclusive Higgs production $H \to \gamma\gamma$ is about 10^5. The mass distribution of the background will vary smoothly across the mass range from 80 GeV to 130 GeV. The Higgs particle signal will be discovered as a slight bump on top of a well calibrated background as shown in Fig. 7(a) [2, 3].

In the MSSM a scalar SM like Higgs boson with mass below 135 GeV should exist. In the LHC the SUSY particle decays will be detected clearly. Fig. 7(b) shows the signal of the SUSY event with 3 leptons and two jets signature [2, 3].

Presumable, if supersymmetry is discovered it will also imply strong support for string theories that may even unify gravitation with the other three interactions. The SM also needs modification to incorporate the recently discovered properties of neutrinos – that they have a mass different from zero [18].

To take advantage of the dominating Higgs decay modes in Fig. 6(a), their inclusive QCD background decays have to be reduced. This can be achieved by using selection rules, which are obtained with the central exclusive diffraction process. This approach, developed about a decade ago, requires special physics and instrumentation in addition to the four major LHC experiments.

3.4 Physics possibilities in the SLHC

The knowledge gained from the physics covered by the SM and its extensions will be available after a few years of LHC operation. Even before knowing which way the experimental results will lead our thinking, some thoughts on the physics potential of the upgraded LHC, running at a luminosity of 10^{35} cm^{-2}s^{-1}, [7], can be summarized as follow.

- Measurement of some of the triple Gauge boson couplings will reach an accuracy comparable with the size of electroweak, and possibly SUSY, virtual corrections.
- New rare decay modes of the SM Higgs boson will become accessible, for example $H \to \mu^+\mu^-$ and $H \to Z\gamma$. The determination of the Higgs couplings to bottom and top quarks, as well as to electroweak gauge bosons, will reach precisions of 10% or better, over a good fraction of the $m_H < 200$ GeV mass range. In the MSSM, the region of SUSY parameter space where at least two Higgs bosons will be observed is significantly enlarged relative to the LHC reach.
- The first observation of SM Higgs pair production may be possible in the $170 < m_H < 200$ GeV mass range.
- In the absence of a Higgs signal, studies of resonant and non-resonant scattering of electroweak vector boson pairs at high mass will benefit from the larger statistics.
- The mass reach for squarks and gluinos will be extended from ~ 2.5 TeV (standard LHC) to 3 TeV (SLHC). In addition, some exclusive SUSY channels which are rate-limited at the standard LHC could be studied in detail with a tenfold increase in statistics, thereby providing additional information about the underlying theory.
- The mass reach for new gauge bosons, or for signatures of extra-dimension models, will be extended by approximately 30% relative to the LHC; in the case of compositeness, the sensitivity to deviations from the expected behavior of quarks in the SM will be extended from a scale of $\Lambda = 40$ TeV to $\Lambda = 60$ TeV.

Chapter 4

Missing mass method

The main problem with SM light Higgs boson discovery is that either large signals are accompanied by a huge background, or the processes have comparable signal and background rates for which the number of Higgs events is rather small. Besides the conventional processes for the detection of a light Higgs boson, the diffraction processes with a rapidity gap on either side of the Higgs boson will provide a clean environment for its production. Diffractive Higgs production may play an important role in identifying and studying a C- and P-even, light SM Higgs boson at the LHC. In publication I, an analysis was performed to identify the light Higgs boson mass in diffractive process using the missing mass method.

4.1 Diffractive scattering

Diffractive events are characterized by the fact that the incoming protons emerge from the interaction intact, or are excited into a low mass state, with only a small energy loss. Diffractive processes, for proton energy losses up to a few percent, are mediated by an exchange with quantum numbers of the vacuum, the so-called Pomeron ($\mathbb{P}$), now understood in terms of partons from the proton[1] [25]. Two types of processes, the single diffraction (SD) and central exclusive diffraction (CED) are of particular interest for the discovery of new physics. Fig. 8 shows the event topologies of the elastic and diffractive scattering processes and the corresponding ways in which the rapidity gaps and diffractive clusters are manifested in the pseudorapidity-azimuthal angle plane.

Most of the soft inelastic diffraction processes, commonly described via single-pomeron-exchange (SPE) or double-pomeron-exchange (DPE), are peripheral, occurring at collision impact parameters around 1.5 fm. The protons involved may stay intact or dissociate. The events are characterized by the momentum loss[2], ξ, the squared four-momentum transfer t and the azimuthal angle ϕ of the proton and by a rapidity gap[3], $\Delta\eta$.

[1] Pomeron is a leading Regge trajectory with vacuum quantum numbers.

[2] The fraction ξ of the momentum lost by protons in the collision is defined as $\xi = 1 - x_F$, where x_F is the Feynman's variable defined as $x_F = \frac{p_z}{p_{zmax}} \simeq \frac{E+p_z}{(E+p_z)_{max}}$, where $p_T \ll |p_z|$.

[3] Gap in the rapidity distribution of final-state hadrons caused by the lack of colour and the effective spin of the exchanged object and defined as $\Delta\eta \equiv -\ln\xi$.

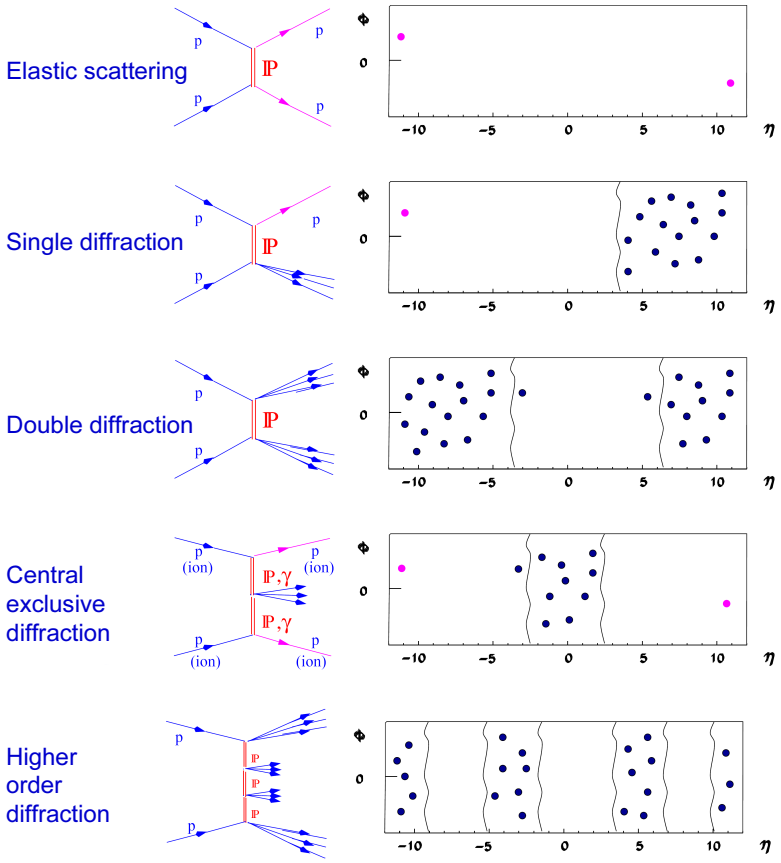

Figure 8. Schematic representation of diffractive process classes and their particle distributions in the pseudorapidity-azimuthal angle plane. The three uppermost ones are single-pomeron-exchange scattering processes.

- **Single diffraction** $(p + p \rightarrow p + X)$
  One leading proton is left intact in the collision and the other one is dissociated into a diffractive cluster in the final state. The leading proton means the scattered proton which has lost some of its momentum to create the mass of the dissociative system and has a low transverse momentum p_T , i.e. the momentum perpendicular to the z-axis.

- **Double diffraction** $(p + p \rightarrow X + Y)$
  Both protons dissociate into diffractive systems with a pseudorapidity gap between them.

- **Central Exclusive Diffraction** $(p + p \rightarrow p + X + p)$
  Two initial protons each emit a Pomeron which collide and create a diffractive system with a pseudorapidity in the central region.

4.2 Central exclusive diffraction process

The cleanest diffractive events are obtained with the central exclusive diffraction process[4] $p + p \to p + X + p$, where X is a central new particle state, which is produced in the $J_z = 0$, C- and P- even state, and the + signs indicate the presence of rapidity gaps [26]. By detecting both leading protons produced in the process, one can reconstruct the mass of the central system with high precision irrespective of its decay mode, as well as investigate its properties such as the spin-parity. This approach augments the standard methods for new particle searches at the LHC due to its sensitivity to CP-violating effects in the couplings of the centrally produced system X to gluons.

In this thesis, Higgs production via the central exclusive process ($p + p \to p + H + p$) with the dominant decay processes of the light Higgs boson ($H \to b\bar{b}$ and $H \to WW/WW^*$) is considered. The Higgs boson may be identified and its mass measured to an accuracy of about 1 GeV by tagging the outgoing protons and using the missing mass method, which is presented below.

Theoretically, the most promising light SM Higgs boson discovery channel is the $H \to b\bar{b}$, whose production cross-section is calculated in [26]. The process allows an independent measurement of the Higgs mass via the $H \to b\bar{b}$ decay with $M_H = M_{b\bar{b}}$, although now the resolution is much poorer with $M_{b\bar{b}} \sim 15 - 20\,\text{GeV}$. The existence of matching peaks, centered about M_H, is a unique feature of the exclusive diffractive Higgs signal. Besides its obvious value in identifying the Higgs and in sharpening the determination of its mass, we will see that the mass equality also plays a key role in reducing background contributions. Another advantage of the $H \to b\bar{b}$ signal is that, at the leading order (LO), the $gg \to b\bar{b}$ background process is suppressed by a $J_z = 0$ selection rule. An analysis, done in [26], for the SM Higgs boson with a mass of 120 GeV is based on perturbative QCD calculations including uncertainties in background and estimates of the rapidity gap survival probability. It gives a prediction for the cross-section

$$\sigma(p + p \to p + H + p) \simeq 3\,\text{fb}\,, \tag{18}$$

with a signal-to-QCD background ratio of

$$\frac{S(H \to b\bar{b})}{B(b\bar{b})} \gtrsim 15 \left(\frac{250MeV}{\Delta M}\right)\,, \tag{19}$$

where ΔM is the mass window for accepted events. For $M_H = 120$ GeV, where the mass resolution is about 1.6%, the mass window chosen is $\Delta M = 4$ GeV [27]. Then Eq. 19 gives $S/B \sim 1$ for the signal-to-background ratio. The analysis did not take into account the pile-up events, the possible coincidence of two SD events that can mimic the CED event and the first level triggering of diffractive Higgs events. These issues have grown to be a major concern in forward physics. By performing modifications to the central trigger system, the signal-to-background ratio of a unity is still possible for the 120 GeV SM Higgs and 1000 for the MSSM lightest Higgs boson [27].

[4]The central exclusive process is a double pomeron exchange process with large rapidity gaps between the central (Higgs decay) and forward regions (intact diffracted protons).

4.3 The missing mass

The missing mass (MM) method can be used to calculate the mass of the centrally produced system with mass M_X in the exclusive reaction $(p + p \rightarrow p \oplus X \oplus p)$, where the leading protons remain intact [28]. For this kind of reaction, the MM method gives a good mass resolution if the momentum of leading protons is measured precisely. The missing mass can be calculated from 4-momenta[5] of the incoming and outgoing protons as

$$MM^2 = (p_1 + p_2 - p_1' - p_2')^2 \,, \tag{20}$$

where p_1 and p_2 are the 4-vectors of the incoming protons and p_1' and p_2' of the outgoing protons. The outgoing scattered beam particles have lost fractions ξ_1 and ξ_2 of their incident momentum, where $\xi_{1,2} = \Delta p_{1,2}/p_{1,2} = 1 - |\overrightarrow{p}'_{1,2}|/|\overrightarrow{p}_{1,2}|$. If the outgoing protons have a very small transverse momentum p_T, Eq. 20 reduces to

$$MM^2 = \xi_1 \cdot \xi_2 \cdot s \,, \tag{21}$$

where s is the square of the center-of-mass energy, 14 TeV in LHC.

4.4 Analysis of the missing mass method

The analysis, performed in Publication I, employs a chain of simulation programs, which include the event generation, simulation of the IP region, the tracking of protons through the LHC beam line, a detector simulation package, and a proton momentum reconstruction algorithm using the detector information.

Event generators

Proton-proton (pp) collisions were simulated using the Monte Carlo (MC) event generators ExHuMe or PHOJET. They produce complete event structures that include all the produced particles and their origin and possible decays.

- **ExHuMe** (Exclusive Hadronic Monte Carlo Event generator)
  ExHuMe is based on the perturbative QCD calculations of the central exclusive process with the centrally produced color singlet system [29, 30].

- **PHOJET**
  A MC event generator which simulates hadronic multiparticle production for hadron-hadron, photon-hadron and photon-photon interactions. It can produce soft and hard type diffractive events as well as elastic and inelastic non-diffractive, together or separately [31].

[5]The four momentum p is defined as $p = (E, \mathbf{p})$, where E is the energy and $\mathbf{p}$ is the momentum of the particle.

Leading proton beam uncertainties

To mimic the condition after a real particle collision, where properties of the scattered protons are not known exactly, uncertainties are added to the outputs of the event generators. The following smeared values are used in further calculations: interaction position of the colliding protons (x^*, y^*, z^*), angles of the scattered (leading) protons with respect to the beam line $(\Theta^*_{x,y})$ and the leading proton energy (E). In the following, the smearing has been performed using independent normalized Gaussian random functions, (r), with expectation values of 0 and a variance of 1.

The event generator assumes that the collisions occur in the origin and thus the smearing has the form

$$\begin{pmatrix} x^* \\ y^* \\ z^* \end{pmatrix} = \begin{pmatrix} \sigma_x \\ \sigma_y \\ \sigma_z \end{pmatrix} \begin{pmatrix} r_x & r_y & r_z \end{pmatrix}, \tag{22}$$

where σ_i, $(i = x, y, z)$, are standard deviations of the IP. The smeared scattering angles were obtained by adding random distortion to the values of the event generators as $\Theta^*_{x,y} = \Theta^{gen}_{x,y} + \sigma_{\Theta_{x,y}} r_{\Theta_{x,y}}$. The uncertainty of the leading proton energy depends linearly on the uncertainty of the beam energy and thus the smeared energy is given by $E = E^{gen}(1 + \sigma_E r)$.

The following uncertainties were used as input data for the study[6]:

- pp interaction region width: $\sigma_{x,y} = 16\,\mu$m and $\sigma_z = 5\,$cm
- beam angular divergence: $\sigma_{\Theta_{x,y}} = 30\,\mu$rad
- beam energy spread: $\sigma_E = 1.1 \times 10^{-4}$.

The two scattered protons and thus ξ_1 and ξ_2 in Eq. 21 are, in general, uncorrelated to each other. The only correlation comes from the transverse position of the IP. For details see Publication I and [32].

Leading proton transport calculation

The transverse displacement $(x(z), y(z))$ of a scattered proton is given by its coordinates $(x^*, y^*, 0)$ and scattering angles $\Theta^*_{x,y}$ at the IP as

$$y(z) = v_y(z) \cdot y^* + L^{eff}_y(z) \cdot \Theta^*_y, \tag{23}$$

$$x(z) = v_x(z) \cdot x^* + L^{eff}_x(z) \cdot \Theta^*_x + \xi \cdot D(z), \tag{24}$$

[6]The reference system (x, y, z) used in the study corresponds to the reference orbit in the accelerator. The z-axis is tangent to the orbit and positive in the beam direction and the x-axis (horizontal) is negative toward the center of the ring.

where $L^{eff}_{x,y}(z)$ is the effective length, $v_{x,y}(z)$ is the magnification and $D(z)$ is the dispersion. The angles $\Theta^*_{x,y}$ are physical scattering angles with the respect to the beam direction and include the beam angular divergence. The protons are traced along the LHC beam line using the MAD (Methodical Accelerator Design) program [33] with the parameters corresponding to LHC optics layout version 6.2 ($\beta^* = 0.5$ m) with a 150 μrad horizontal crossing angle [34]. Although the analysis was carried out for CMS/TOTEM (IP5), the results should be equally valid for ATLAS (IP1). At every accelerator element, each proton that remains within the beam pipe aperture is recorded.

Tagging detector response and acceptances

The tagging detectors will measure (accept) only those protons that do not hit the beam pipe wall and reach the active area of the detector. In analysis of the detector response, only the horizontal scattering plane is considered and the following input parameters are assumed:

- The detector is assumed to be 100% active at a distance Δ from the beam center [35], where $\Delta = k\sigma_x(z) + \delta$, and $k = 10$ describes the number of standard deviations of the horizontal beam width, $\sigma_x(z)$, that is required as a safety margin for each detector location[7]. In the analysis, the physical edge of the detector is assumed to be at a distance of $\delta = 0.5$ mm from the area of the detector that is 100% active.
- For the protons within the active area of a detector, the inaccuracy in the detector's position measurement is introduced by smearing the simulated hit coordinates (x_{sim}) according to a Gaussian distribution as $x = x_{sim} + \sigma_x r$, where $\sigma_x = 10\,\mu$m and the normalized Gaussian random function.
- Similarly the beam position uncertainty at each detector location is accounted for by smearing the hit coordinates with $\sigma_{beam} = 5\,\mu$m.

The acceptance dependences on ξ of protons moving in the clockwise and counter-clockwise directions along the LHC beam line are shown in Fig. 9(a) for the 215 and 420 detector locations. The ξ-acceptances indicate that the leading proton from the central exclusive diffraction is seen in the detector when $0.025 \leq \xi_{215} \leq 0.20$ for 215 m location and $0.002 \leq \xi_{420} \leq 0.015$ for 420 m location. It should be noted that the acceptance ranges do not overlap when the LHC optics layout version 6.2 is used. In [36], the LHC optics layout version 6.5 [37] and MAD-X [38] have been used and slightly overlapping acceptances were obtained, as shown in Fig. 9(b). This update slightly improved the mass acceptance and resolution results, which are presented in Sec. 4.6, but the change is not significant. The updated results are not presented here and can be found in [27, 36].

4.5 Momentum reconstruction

The observed proton transverse (x) coordinate, given in Eq. 24, depends on three initial parameters of the scattered proton at the IP: fractional momentum loss (ξ), initial scat-

[7] The LHC collimators extend to $6\sigma_x(z)$. The safety margin can be assumed to be anywhere between 10 and 15.

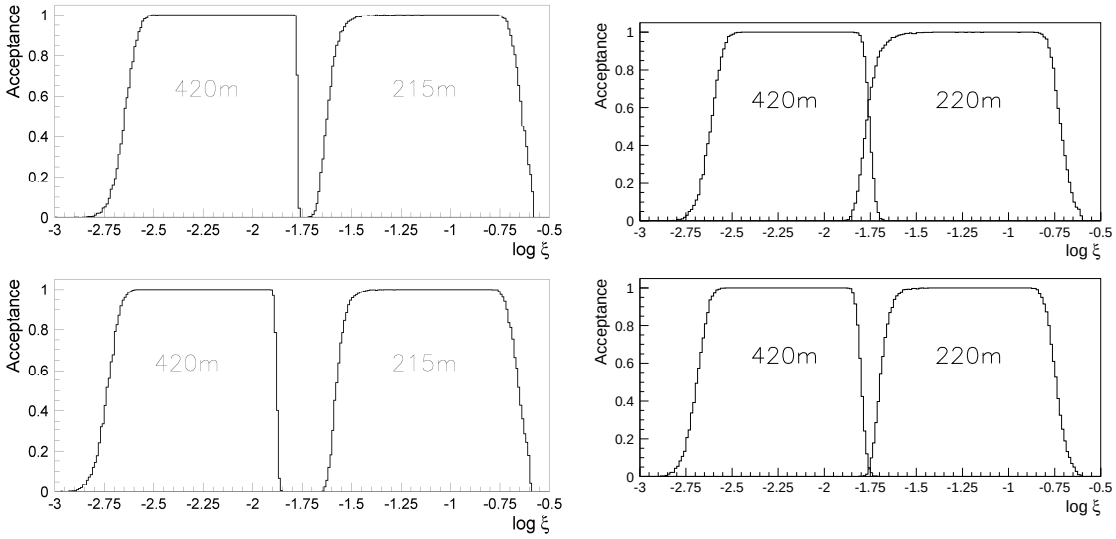

Figure 9. Proton momentum loss, ξ, acceptances, using LHC optics layout version (a) 6.2 and (b) 6.5, for the set of detectors at 420 m and at 215 m (labelled 220 m in (b)) from the IP. The upper plots are for protons circulating clockwise and the lower ones for protons circulating counter-clockwise along the LHC beam line.

tering angle (Θ_x^*) and its position of origin (x^*). In the reconstruction procedure, two x-measurements from a detector doublet are used to determine ξ and Θ_x^* neglecting the x^* dependence, whose effect is treated as an independent source of uncertainty.

Two detector locations were chosen to extend the acceptance in proton fractional momentum loss (ξ). Based on the approved LHC instrumentation [5], two detector locations were chosen (each consisting of at least a doublet of proton tagging detectors):

- 215 and 225 meters from the IP (referred to later as 215 m location),
- 420 and 430 meters from the IP (referred to later as 420 m location).

The second location (420 m) is in the cryogenic section of the machine and requires special design consideration, discussed in detail in section 5.2.

Each detector doublet ($i = 215, 420$) yields two observables: the average horizontal proton coordinate with respect to the beam axis, $< x >_i = (x_{1,i} + x_{2,i})/2$, and their difference $\Delta x_i = x_{2,i} - x_{1,i} = \Theta_{x,i}\Delta z_i$. For both 215 m and 420 m locations the detector doublet spacing of $\Delta z_i = 10\,\mathrm{m}$ was used. The measured values of $< x >_i$ and Δx_i are related to the proton fractional momentum loss, ξ, and the scattering angle Θ_x^* at the IP. An unfolding procedure is used to obtain these parameters from the measured values in a given detector doublet (i). First, a linear coordinate transformation is defined that causes the $< x >_i - \Delta x_i$ pairs to be more uniformly spread. The dependence of ξ on these transformed coordinates is parameterized by fitting a function to the observed average ξ-values in the plane of the transformed coordinates.

The parameters for the unfolding were determined in a simulation where no detector or beam related uncertainties were applied. The relative error of the resulting proton fractional momentum loss determination was found to be within 0.2% of nominal values over the whole ξ-range that is within the acceptance of each detector location.

4.5.1 Feasibility of the method

The feasibility of the method was studied by including the separate uncertainties that were presented in section 4.4. The detailed results are presented in Publication I and a summary of these is given in Tab. 4.5.1.

Uncertainty	215 m	420 m
Transverse IP position	$0.5 - 1.8\,\%$	$0.6 - 7.5\,\%$
Detector resolution	$0.8 - 1.4\,\%$	$0.3 - 6.0\,\%$
Beam energy	$< 0.5\,\%$	$0.5 - 4.0\,\%$
Beam angular divergence	$< 0.5\,\%$	$< 0.5\,\%$
Beam position resolution	$< 0.5\,\%$	$< 0.5\,\%$

Table 5. Summary of the relative ξ-resolution for the 215 m and 420 m locations.

At both detector locations, major contributors to the overall ξ resolution are the uncertainty of the transverse IP position and the resolution of the proton tagging detector. In addition, the beam energy uncertainty contributes to the resolution at the 420 m location at low ξ-values. For higher ξ-values at 420 m, i.e. $\xi_{420} > 0.005$, the overall ξ-resolution remains below 5 %.

4.6 Higgs mass resolution

To reconstruct the Higgs mass using Eq. 21, each leading proton is required to be within the acceptance of either the 215 m or 420 m locations. The acceptance as a function of the mass of the centrally produced system is shown in Fig. 10(a). In the light Higgs mass range, 60 GeV$< M <$200 GeV, there is no acceptance for detecting both protons at the 215 m location. The case where both protons are within the acceptance of the 420 m locations is drawn independently.

The Higgs mass resolutions for events with protons within the acceptance of the 420 m location on both sides, and for events with one proton within the acceptance of the 215 m location on one side and the other proton within the acceptance of the 420 m location on the other side (labelled asym.) are plotted in Fig. 10(b).

The reconstructed Higgs mass resolution decreases with increasing mass of the centrally produced system. It can be concluded that with the missing mass method and a pair of leading proton detectors at 420 m location on both sides of the IP, a Higgs boson within a mass range of 120-200 GeV could be measured with a mass resolution of the order of 1 GeV. In addition, it would enable large statistics of pure gluon jets to be collected, thereby using the LHC as a gluon factory. A feasibility study for placing the detectors at the 420 m location is introduced in section 5.2.

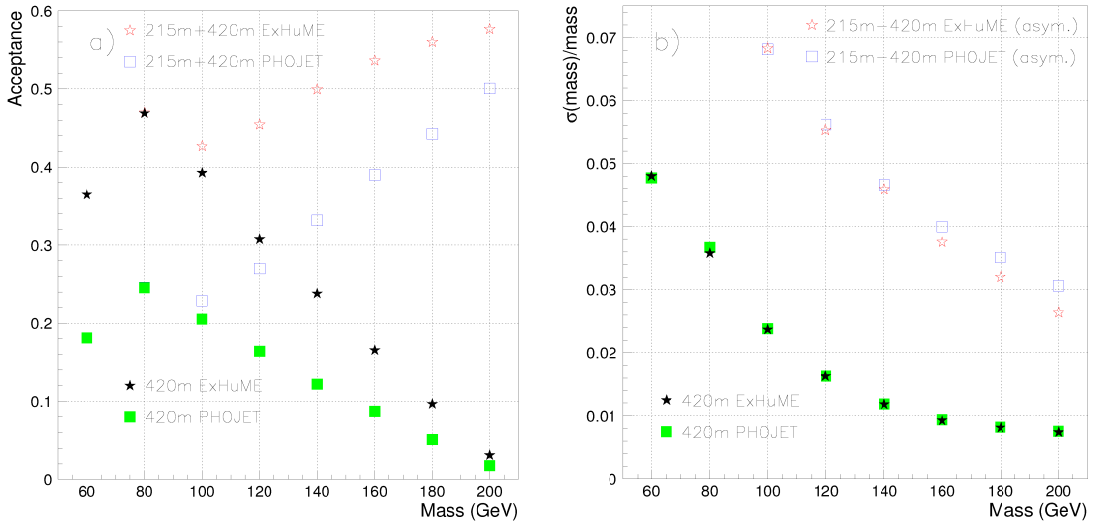

(a) (b)

Figure 10. (a) Mass acceptance for events with protons within the acceptance of a set of detectors at 420 m on both sides of the interaction point (420m) and for events with protons within the combined acceptance of the two sets of detectors at 215 m and 420 m on both sides of the interaction point (215m+420m). (b) Mass resolution for events with protons within the acceptance of the 420 m location on both sides of the interaction point (420m) and for events with one proton within the acceptance of the 215 m location on one side of the IP and the other proton within the acceptance of the 420 m location on the other side (215m+420m (asym.)).

Chapter 5

Forward physics experiments at the LHC

The TOTEM and FP420 experiments are extensions of the originally planned LHC, and the first of them was approved officially only in 2004. These are experiments that look forward to new physics through clean diffraction processes and can help to calibrate the parameters of the LHC.

5.1 TOTEM experiment

The TOTEM[1] experiment [5, 39, 40] will measure the total pp cross-section, elastic pp scattering and diffractive phenomena at early stages of the LHC runs by using special beam optics. The TOTEM will have dedicated runs with special high-β^* beam optics and a reduced number of proton bunches resulting in a low effective luminosity between $1.6 \times 10^{28}\,\mathrm{cm}^{-2}\mathrm{s}^{-1}$ and $2.4 \times 10^{29}\,\mathrm{cm}^{-2}\mathrm{s}^{-1}$.

The main objectives of the TOTEM are

- Elastic proton scattering over a wide range in momentum transfer[2] up to $-t \approx 10\,\mathrm{GeV}^2$.
- The total pp cross-section, σ_{tot}, with an absolute error of 1 mb using the Optical theorem with luminosity independent method. This requires the simultaneous measurement of the elastic pp scattering down to the four-momentum transfer of $-t \approx 10^{-3}\,\mathrm{GeV}^2$ and of the total inelastic pp interaction rate with an adequate acceptance in the forward region.
- Diffractive dissociation, including single, double and central diffraction topologies using the forward inelastic detectors in combination with the measurement of the forward protons.

[1] TOTEM is a acronym for TOTal and Elastic Measurement.

[2] Four-momentum transfer squared $-t \equiv -(p' - p)^2 \approx p^2\theta^2$, where p' and p are the four momentums of the incoming and outgoing particles or systems of particles, respectively, and θ is the forward angle of the outgoing particle. The last approximation is true only for the elastic scattering.

- Hard diffraction processes with particle jets with transverse momentum starting at as low as possible, $|p_T| > 15 - 30\,\mathrm{GeV}$, in combination with the CMS detector.

The TOTEM is situated at IP5 of the LHC (Fig. 1) and complements the CMS detector with the forward trackers T1 and T2 inside the CMS and with a system of Roman Pot (RP) stations at distances of 147 m, (180 m) and 220 m from the IP [41]. The layout of the TOTEM experiment is shown in Fig. 11. The T1 telescopes on both sides of the interaction point will consist of five planes of Cathode Strip Chambers (CSC) covering the pseudorapidity (defined in Appendix A) range of $3.1 < |\eta| < 4.9$. For T2, extending the acceptance into the range of $5.3 < |\eta| < 6.7$, the Gas Electron Multiplier (GEM) technology is used. The RP detector system is optimized to measure proton scattering at small angles down to a few μrad, which corresponds to the pseudorapidity range of $9.5 < |\eta| < 13$.

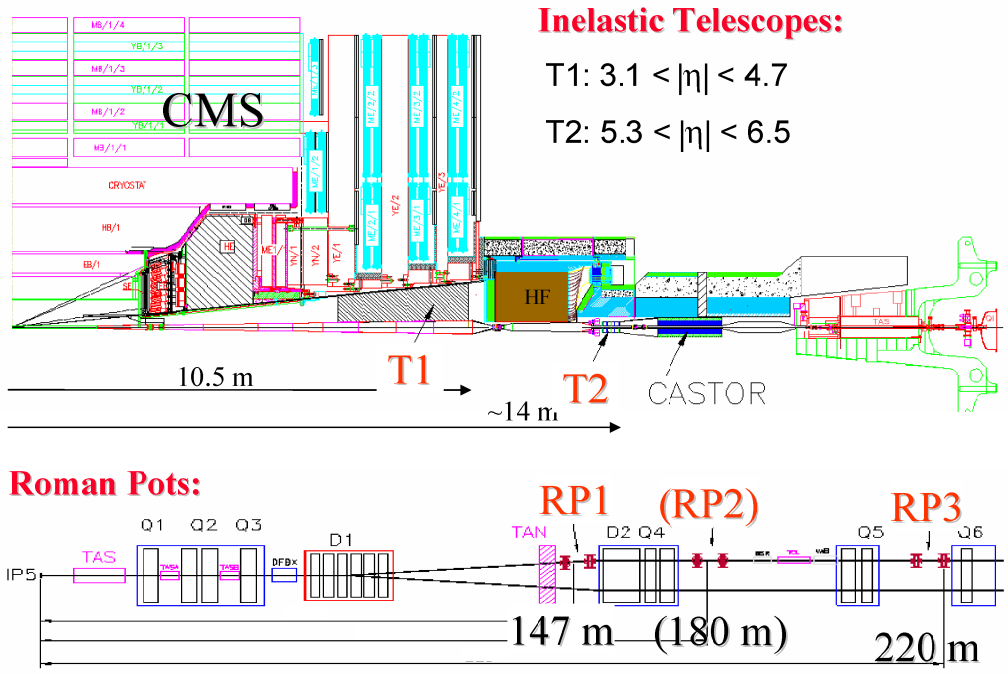

Figure 11. LHC accelerator and experiments

The CMS and TOTEM experiments will be able to take data together, with TOTEM acting technically as a subdetector of CMS with the capability to contribute to the level-1 trigger. The trigger signal from the Roman Pots at 220 m arrives at the CMS global trigger still within its latency time. With the Roman Pots further away, level-1 triggering would not be possible. The combined CMS+TOTEM experiment has a unique rapidity coverage together with an excellent acceptance for leading protons as shown in Fig. 12. A part of the only coverage gap around $\eta = 8$ could be filled with an additional leading proton detector at a later time. Examples of this are μstation or μpot, which are presented in chapter 6, that could be placed on both sides at 19 m from the IP [42].

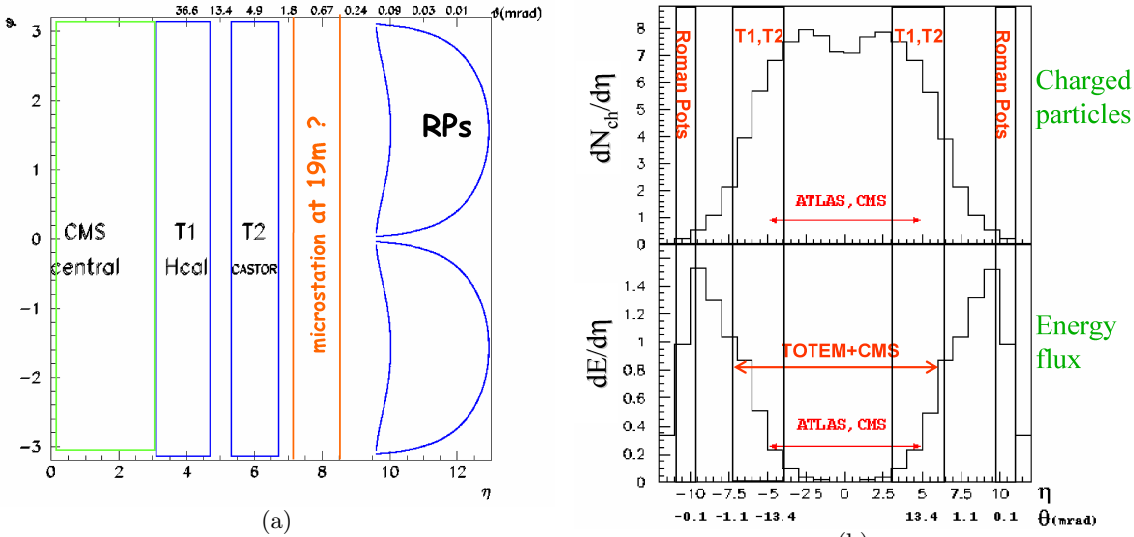

(a) (b)

Figure 12. (a) Acceptance coverage of CMS and TOTEM detectors and a possible coverage range of μstations or μpots at $\beta^* = 1540$ m. (b) Charged particle and momentum flux of the particles from the collision and the pseudorapidity coverage of TOTEM and CMS detectors at high β^*.

5.1.1 Elastic scattering

The elastic scattering over a large t-range is of primary importance in distinguishing between different models of soft proton interactions which exhibit significantly different cross-sections at large energies and large t-values. Data on elastic scattering at low t will be extrapolated to $t = 0$ in order to measure the total cross-section with the luminosity independent method. For an accurate extrapolation, measuring to values of the momentum transfer as low as $-t \approx 10^{-3}\,\mathrm{GeV}^2$ is required.

The differential cross-section of elastic pp interactions at the LHC ($\sqrt{s} = 14\,\mathrm{TeV}$) predicted by the BSW model [43,44] is shown in Fig. 13(a). Several t-regions with different scattering behaviors can be identified. For $|t| < 10^{-3}\,\mathrm{GeV}^2$, Coulomb scattering is dominant, whereas for $|t| > 10^{-3}\,\mathrm{GeV}^2$, nuclear scattering via Pomeron exchange takes over, with nuclear-

Running scenario	**1**	**2**
β^* [m]	1540	18
Number of bunches	43	2808
Protons per bunch	$0.3 \cdot 10^{11}$	$1.15 \cdot 10^{11}$
Beam size at IP [μm]	454	95
Luminosity [$\mathrm{cm}^{-2}s^{-1}$]	$1.6 \cdot 10^{28}$	$3.6 \cdot 10^{32}$
$\|t\|$-range [GeV^2]	$0.002 - 1.5$	$0.6 - 8$

Table 6. TOTEM running scenarious with high (1) and low (2) β^* optics as shown in Fig. 13(a).

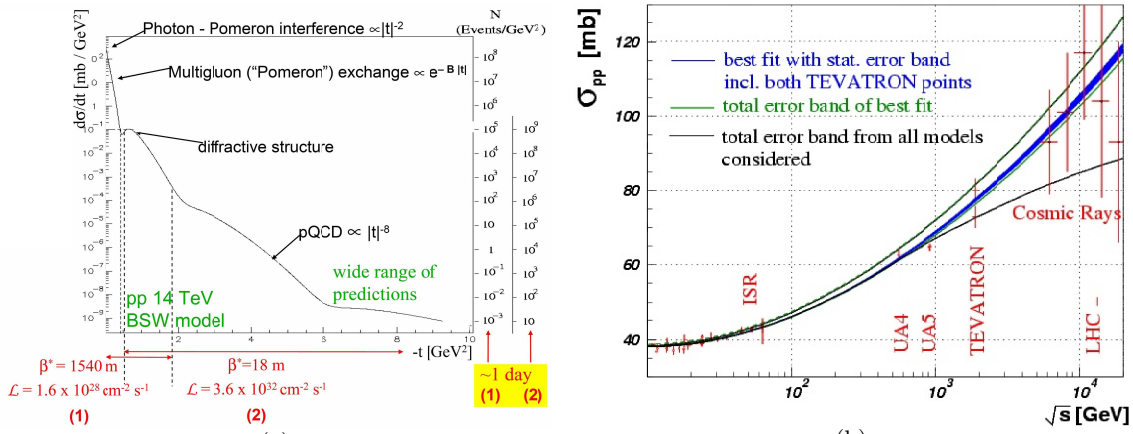

Figure 13. (a) prediction for elastic pp scattering cross-section at LHC with one-day statistics for the running scenarios defined in Tab. 5.1.1. (b) COMPETE fits to all available pp and $p\overline{p}$ scattering data with statistical (blue solid) and total (dashed) error bands, the latter taking into account the Tevatron ambiguity. The outermost curves (dotted) give the total error band from all parameterizations considered.

Coulomb interference in between, thus allowing a measurement of the ρ ratio[3]. At large t-values ($|t| > 1\,\mathrm{GeV}^2$), perturbative QCD with e.g. triple-gluon exchange might describe the central elastic collisions of the proton. Many different models try to describe the elastic scattering at large t-values, which are associated with small interquark tranverse distances within the proton, and thus high precision measurements up to ($|t| \approx 10\,\mathrm{GeV}^2$) will help to understand the structure of the proton.

The elastic scattering distribution extends over 11 orders of magnitude and has therefore to be measured with several different optics scenarios (β^*-values), as described in Tab. 5.1.1.

Fig. 13(a) shows how a decrease of β^* shifts the observable $|t|$-range to larger values and simultaneously increases the luminosity and compensates the drastic decrease of the cross-section.

5.1.2 Total cross-section

As a result of the total cross-section measurement, the TOTEM experiment will provide an absolute calibration of the machine luminosity. Fig. 13(b) summarizes the existing data from low energies up to collider and cosmic-ray energies and shows how the total pp cross-section increases with increasing center of mass energy. An overall fit, $\sigma_{tot} \propto \log^{\gamma}(s)$ with $\gamma = 2.0$, of the center of mass energy dependence of the total cross-section gives the following values for σ_{tot} and for the ratio ρ at the LHC energy $\sqrt{s} = 14\,\mathrm{TeV}$:

$$\sigma_{tot} = 111.5 \pm 1.2\,\mathrm{mb};\ \ \rho = 0.1361 \pm 0.0015. \tag{25}$$

[3]Ratio $\rho \equiv \mathrm{Re}(M(s,t=0))/\mathrm{Im}(M(s,t=0))$ is the ratio of the real to the imaginary part of the elastic forward scattering amplitude.

The total pp cross-section is related to the relativistic scattering amplitude through the optical Theorem:

$$\sigma_{tot} = \frac{16\pi}{s}\mathrm{Im}(F(s, t = 0)), \tag{26}$$

where $\sqrt{s}$ is the center of mass energy[4] and $F(s,t)$ has further terms for the Coulomb and hadronic amplitudes. Use of Eq. 26 leads to the following equation[5]:

$$L\sigma_{tot}^2 = \frac{16\pi}{1+\rho^2} \cdot \frac{dN_{el}}{dt}|_{t=0}, \tag{27}$$

and with Eq. 1 ($L\sigma_{tot} = N_{el} + N_{inel}$) the total pp cross-section is obtained as

$$\sigma_{tot} = \frac{16\pi}{1+\rho^2} \cdot \frac{dN_{el}/dt|_{t=0}}{N_{el} + N_{inel}}, \tag{28}$$

where N_{el} and N_{inel} are total elastic and inelastic rates. Eq. 28 allows a luminosity independent determination based on the total elastic and inelastic rates ($N_{el} + N_{inel}$) and the extrapolation of the pp elastic scattering to the optical point $t = 0$ ($dN_{el}/dt|_{t=0}$), assuming the simple exponential dependence $e^{-B|t|}$ which is known to describe the data well in the very small t region. Hence a simultaneous measurement of the total inelastic rate and the elastic scattering at the lowest possible $|t|$-values is needed. The luminosity is given by

$$L = \frac{1+\rho^2}{16\pi} \cdot \frac{(N_{el} + N_{inel})^2}{dN_{el}/dt|_{t=0}}. \tag{29}$$

In Eqs. 28 and 29, the ratio ρ must be known with great precision to accurately determine the total cross-section and luminosity.

TOTEM/CMS will be able to study a wide variety of processes, previously inaccessible, that will challenge all existing ideas about diffraction, and hopefully point the way towards a better understanding of diffractive phenomena.

5.2 FP420 experiment

The FP420 is an R&D collaboration formed to investigate the feasibility of installing forward proton tagging detectors in a 15 m-long region 420 m from the IP of ATLAS and/or CMS [45]. These detectors are envisaged to be sub-detector upgrades to the central detectors, which could be installed at a suitable time after the initial phase of LHC running. The outgoing protons that have lost a small fraction of their initial momentum emerge from the beam envelope in the high dispersion 420 m region when the LHC runs with standard high-luminosity optics. This is visualized in Fig. 14, which shows a simulation of a proton transverse deviation with various fractional momentum losses. The 420 m detectors cover

[4] The center of mass energy squared is defined as $s = (p_1 + p_2)^2 = (p_1' + p_2')^2$, where p_1, p_2 and p_1', p_2' are the four-momentums of the incoming and outgoing elastically scattered protons.

[5] $\frac{d\sigma}{dt} = \frac{16\pi}{s^2}|F(s,t)|^2$ and $|F|^2 = (\mathrm{Re}^2(F) + \mathrm{Im}^2(F)) = \mathrm{Im}^2(F)(\rho^2 + 1)$.

the region of fractional proton momentum loss $0.002 < \xi_{420} < 0.015$, giving access to central systems in the mass range 30 GeV $< M <$ 200 GeV. This complements and extends the reach of the proposed RP detectors at 220 m at ATLAS and CMS/TOTEM, which have no acceptance for central systems below 200 GeV with double proton tags in normal high luminosity LHC running.

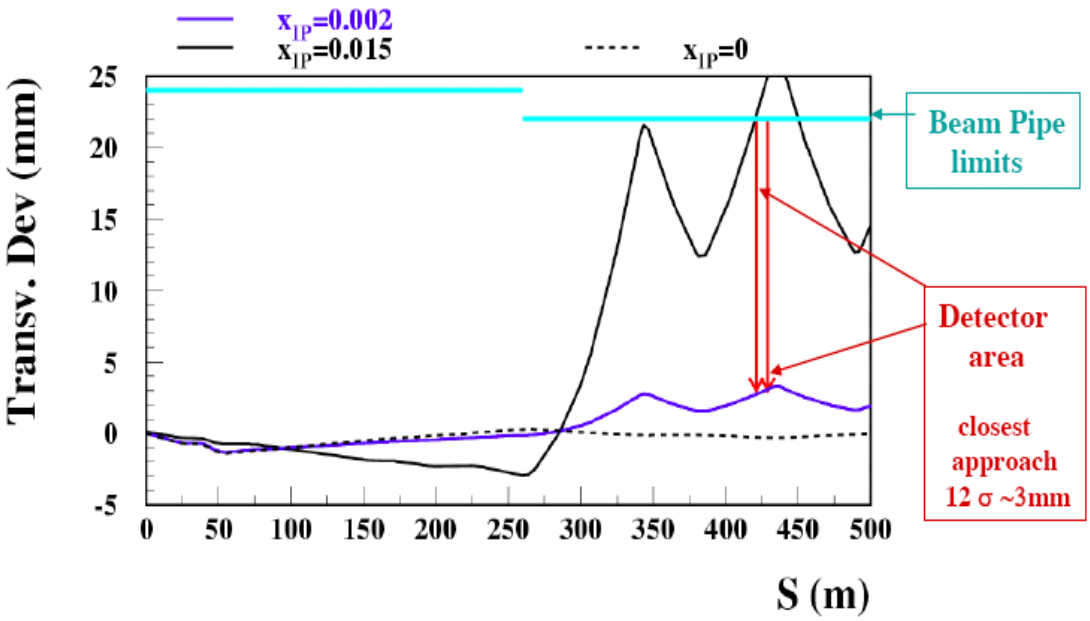

Figure 14. Simulation of the leading protons transverse deviations (y-axes) in mm with fractional momentum losses of $\xi = 0$ (dashed), $\xi = 0.002$ (purple) and $\xi = 0.015$ (black) at the IP. The x-axis gives the distance form the IP. Also shown are the beam pipe limits and detector area at the 420 m location (red) with the closest approach to the beam of 12σ.

The main motivation [26, 45] and objectives of the FP420 are

- Reconstruction of mass of the centrally produced system to an accuracy of about 1 GeV, irrespective of the decay products, by double-tagging the protons at 420 m on both sides of the IP (see below and chapter 4).
- Establishment of the quantum numbers of the SM Higgs boson at low luminosity ($\sim 30\,\mathrm{fb}^{-1}$). An absolute determination of the quantum numbers of any produced resonance is possible by measurements of the correlations between outgoing proton momentum – the central system is in spin 0^{++}, C- and P- even parity state.
- Observation of the CP violation in the Higgs sector that is seen directly as azimuthal asymmetries in the tagged protons (a measurement previously proposed only at a future linear collider).
- To be the discovery channel in certain regions of the MSSM at low luminosity. The central exclusive production of the lightest MSSM Higgs Boson is significantly enhanced, and in these scenarios the muon triggers alone will deliver sufficient events

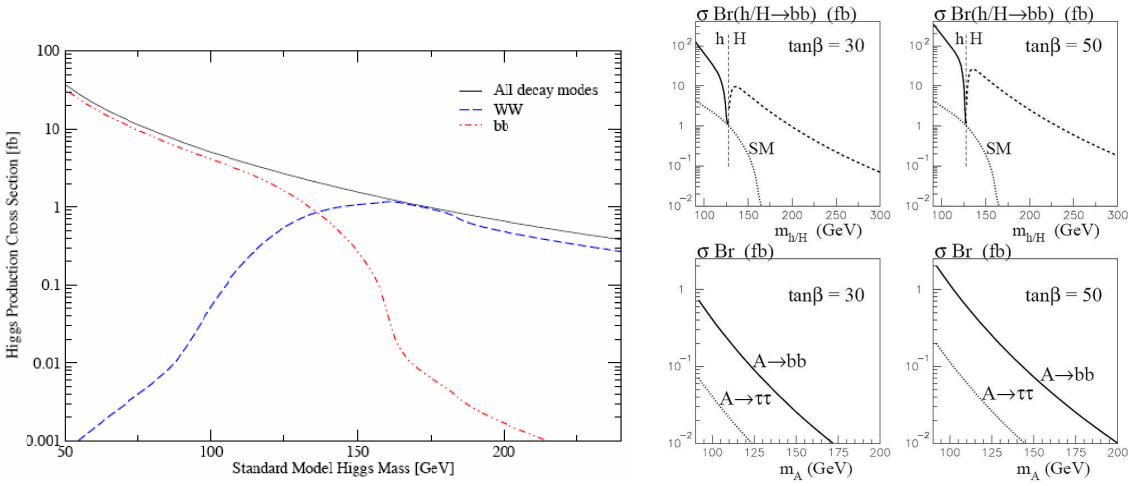

(a) (b)

Figure 15. (a) The cross-section times branching ratio for the central exclusive production of the SM Higgs boson as a function of Higgs mass in the WW and $b\bar{b}$ decay channels. (b) The cross-sections, times the appropriate $b\bar{b}$ and $\tau^+\tau^-$. branching fractions, predicted for central exclusive diffractive production of $h(0^+)$, $H(0^+)$ and $A(0^-)$ MSSM Higgs bosons (for $\tan\beta = 30$ and 50) at the LHC. The dotted curve in the upper plots shows the cross-section for the production of a SM Higgs boson. The vertical line separates the mass regime of light $h(0^+)$ and heavy $H(0^+)$ bosons [23].

that double proton tagging may be the discovery channel. At high luminosity ($\sim 100\,\mathrm{fb}^{-1}$), a direct observation of CP-violation in some SUSY Higgs scenarios and disentanglement of a wide range of SUSY scenarios, even at nearly degenerate Higgs sectors.

- Possibility to turn LHC into a glue-glue and $\gamma\gamma$ collider, where the energy of the gluons is known to within 2 GeV.

In consequence of the selection rules and QCD background reduction, the central exclusive process is predicted to enable direct access into the dominating light SM Higgs boson decay channels at the low LHC luminosity. Fig. 15(a) shows the cross-section of the two dominating light SM Higgs boson decay channels for the central exclusive production (compare to Fig. 6(a)).

The $H \to b\bar{b}$ channel should be observable with a large cross-section and signal-to-noise ratio, as presented in section 4.2. Assuming a Gaussian mass resolution of the tagging detectors of width ~ 1 GeV, it is estimated that 11 signal events and a signal-to-background ratio of order 1 for Higgs boson masses in the range from 80 GeV to 130 GeV can be achieved with a luminosity of $30\,\mathrm{fb}^{-1}$ [28]. However, since the mass resolution of the proton taggers is used to suppress the background, any degradation in the expected resolution will diminish the signal-to-background ratio. In addition, the triggering at level-1 at ATLAS and CMS presents a difficulty because the 420 m detectors are beyond the distance at which signals arrive at the central detectors in time for a level-1 trigger decision. In order to access the

$b\bar{b}$ decay channel, a good understanding of the tagging detectors and a clever triggering at level-1 must be achieved [46].

The simplest decay channel from an experimental perspective is the $H \to WW/WW^*$ decay mode, in which one or both of the W bosons decays leptonically. This channel does not suffer from either of the $b\bar{b}$ channel problems. Suppression of the dominant backgrounds does not rely primarily on the mass resolution of the detectors and level-1 triggering is not a problem in the leptonic and semi-leptonic decay channels. However, the advantages of forward proton tagging, mentioned above, are still explicit. With standard single and double lepton trigger thresholds at ATLAS and CMS, approximately 5 events are expected with double proton tags for Higgs boson masses in the range from 140 GeV to 200 GeV with $30\,\mathrm{fb}^{-1}$ of LHC luminosity, and even 10 events with slightly reduced trigger thresholds [46].

In the large $\tan\beta$ region of MSSM parameter space, the light Higgs observation in $b\bar{b}$ decay is much more favorable than in the SM Higgs case. It is expected to have close to 1000 exclusively produced double-tagged h and H bosons with 220 m and 420 m detectors in $30\,\mathrm{fb}^{-1}$ of LHC luminosity, for $M_{h,H} \sim 125$ GeV and $\tan\beta = 50$, where the QCD background becomes practically negligible. The predicted signal-to-background ratios are in excess of 20 for the lightest Higgs mass of ~ 130 GeV [23].

5.2.1 Acceptance and mass resolution

The closest possible safe distance of approach to the beam at 420 m, assuming ideal beam conditions, is $\sim 3\,\mathrm{mm}$ (12σ). Fig. 16(left) shows the acceptance for 420 m - 420 m tags as a function of the distance of approach of the silicon detectors. The difference between ATLAS and CMS is due to the difference in the plane of the crossing angle of the beams at IP1 and IP5. The effect of this difference persists up to 220 m, but is washed out by 420 m. If the beam conditions are good and a 3 mm approach is possible, detecting one of the outgoing protons in a 220 m detector can double the acceptance for 120 GeV central systems at ATLAS, and the acceptance for higher masses is significantly increased at both interaction points [47].

Fig. 16(right) shows the mass resolution on the central system of FP420 as a function of the mass of the SM Higgs boson, for 420 m - 420 m and 220 m - 420 m proton tags. The plot is obtained using the Missing Mass method with LHC optics layout version 6.4 [48] – compare with Fig. 10(b). The achievable resolution is better than 1.5 GeV if both protons are detected at 420 m. If one proton is detected at 220 m, the resolution is reduced to $\sim 3\,\mathrm{GeV}$ for a 120 GeV central system at ATLAS, and $\sim 3.5\,\mathrm{GeV}$ at CMS. Therefore, FP420 achieves the best mass resolution and maximum robustness to poor beam conditions.

5.2.2 Instrumentation

The current LHC design has a 15 m long "interconnection cryostat" at 420 m that connects the superconducting arcs of the accelerator with the warmer interaction regions. The cryostat provides continuity not only of the beams, but also of the insulation vacuum, electrical power, cryogenic circuits and thermal and radiation shielding of the accelerator. The FP420 module is essentially a 15 m long tracking detector that will replace the interconnection cryostat shown in Fig. 17 [47].

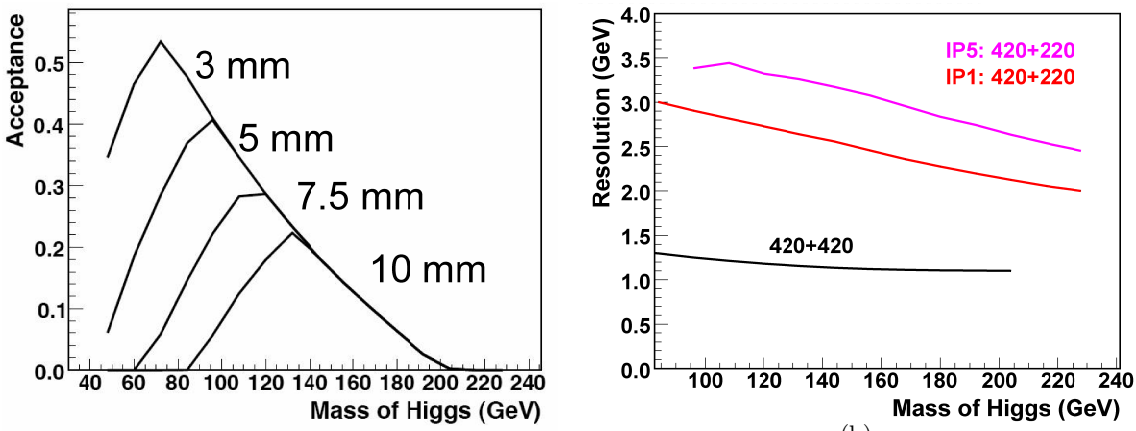

(a) (b)

Figure 16. (Left) Acceptance as a function of Higgs boson mass for the detection of both protons at 420 m at varying distances from the beam. (Right) The mass resolution as a function of Higgs boson mass for the case where both protons are detected at 420 m (black line), one proton is detected at 420 m and the other at 220 m at ATLAS (IP1) (red line) or at CMS (IP5) (purple line) [47].

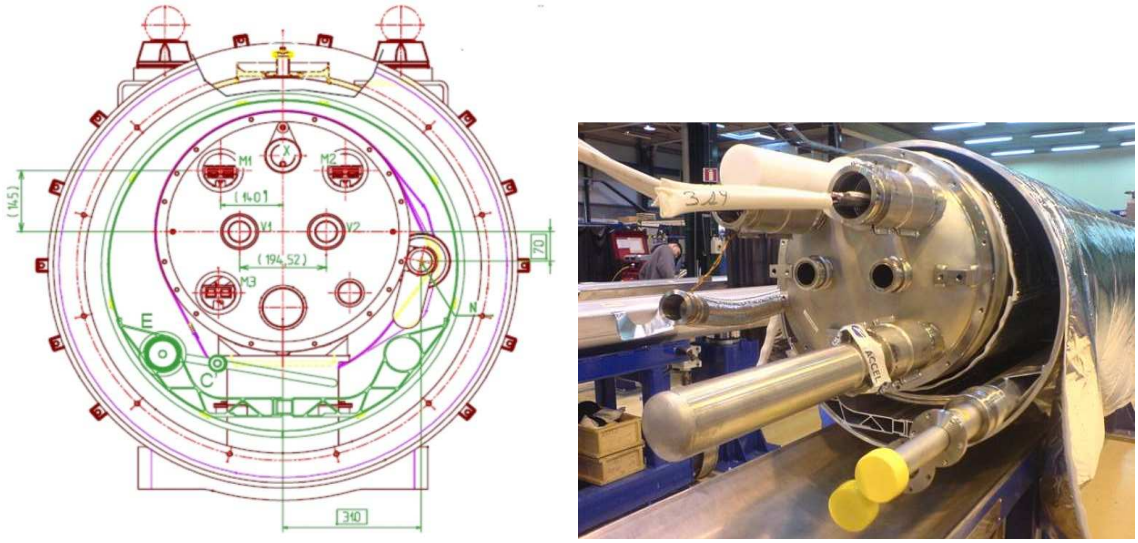

(a) (b)

Figure 17. The 420 m connection cryostat cross sectional blueprint (a) and photograph (b) at LHC start-up. The leading protons from the central exclusive production can be detected by positioning suitable detectors between the beam pipes seen in the middle.

The protons of interest emerge between the two beam pipes V1 and V2 in the middle in Fig. 17(a). V2 is the outgoing beam pipe closest to the wall of the LHC tunnel. In order to tag the leading protons, silicon detector clusters are placed at least at each end of the FP420 module shown in Fig. 17(b). The detectors must move into position of closest safe approach to the beam ($\sim 3\,\mathrm{mm}$) when the LHC running conditions become stable after injection and acceleration of proton bunches to 7 TeV.

The three bus bars, labelled M1, M2 and M3, must be continuous and maintained at 1.9 K. These carry the currents for the LHC magnets. The heat exchanger (X), up in the middle, contains 2-phase liquid helium and must remain parallel to the floor throughout the region. In the LHC start up, the beam pipes are within the cold volume at 1.9 K. It is desirable to raise the beam pipes to room temperature in this region to enable easy running of detectors and electronics. The end pieces of FP420 must match exactly the cross-section of the present interconnection cryostat, and must return the beam pipes to 1.9 K for re-connection into the LHC [47].

The FP420 detectors must be aligned internally and relative to the beam to better than $50\,\mu$m precision, which is required to obtain ~ 1 GeV mass resolution of the central system. The detector position relative to the beam can be measured using either beam position monitors (BPMs) fixed at a known distance from the silicon detectors, or by making use of a high-rate physics process which produces protons of a known momentum loss in the FP420 acceptance range. This method has the advantage that the magnetic field between the central detectors and FP420 does not have to be precisely known a-priori. A measurement of the time of arrival of the protons at FP420 in the 10 ps range allows for matching of the detected protons with a central vertex. This method is also desirable to reject non-physics backgrounds and overlap events at high luminosities.

Chapter 6

Forward detector systems

It is an enormous engineering challenge to approach the beam by the tagging sensor closer than 1 mm distance in the primary vacuum of the machine. In the TOTEM and FP420 experiments the leading proton tagging is planned to be done by using solid state sensors with the following detector systems.

6.1 Roman Pots

It is accepted to use two Roman Pot (RP) stations located symmetrically on both sides of the IP at 147 m and 220 m locations. Each station is composed of two units, separated by a distance of 4 m, with each unit consisting of two pots that move vertically and one that moves horizontally by stepping motors. Fig. 18(a) shows the vertical RP with its main components. The RP allows the detectors to function close to the beam outside the primary vacuum of the machine – the pots are pulled into the main vacuum chamber with a force of ~ 1 kN. A compensation system is required to neutralize this force on the pot and to simplify its operations. Fig. 18(b) shows a cross-section of the vertical RP of Fig. 18(a) [5].

A thin window ($\sim 200\,\mu$m) between the beam and the detectors made of stainless steel foil provides the separation from the primary vacuum of the machine and is also required to provide adequate shielding of the electronics against the radio frequency pick-up induced by the electromagnetic fields generated by the high intensity bunched beam structure. The RPs will be placed in the shadow of the LHC collimators to profit both from their protection against accidental beam losses and from their cleaning efficiency to reduce the background. In particular, the minimum distance of the RP window from the beam is defined in the vertical plane by the beam halo profile, and in the horizontal plane by the settings of the absorbers, which protect the machine in case of asynchronous beam abort. Fig. 19 illustrates the closest safe approach to the beam. Both constraints limit the approach to the $10\,\sigma$ beam envelope: for the TOTEM high-β^* optics, this corresponds to a vertical distance of ~ 1 mm. In order to meet both the physics performance and the safety requirements, the mechanical stability of the detectors and their mountings in the pot need to be within at most $\sim 20\,\mu$m [5].

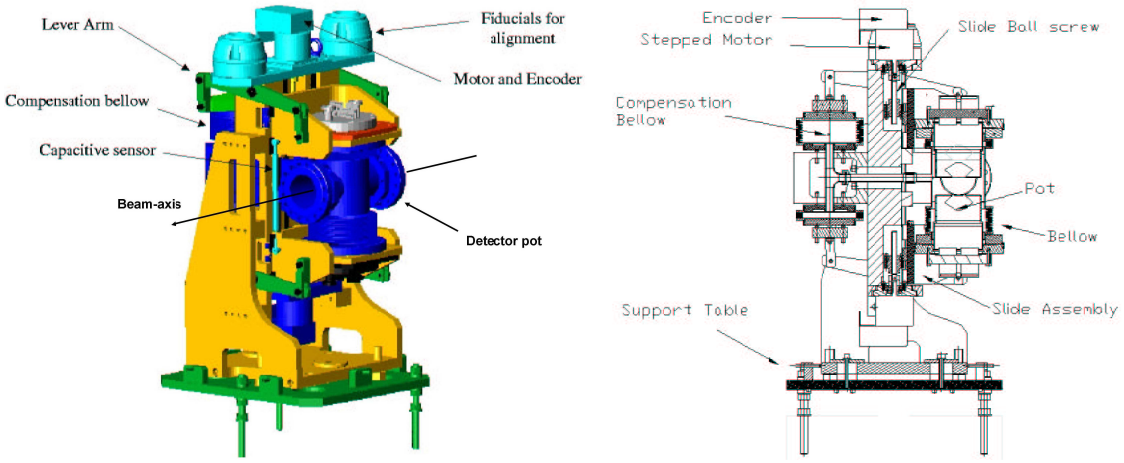

(a) (b)

Figure 18. (a) Vertical Roman Pot device and (b) its cross-section with named main components [5].

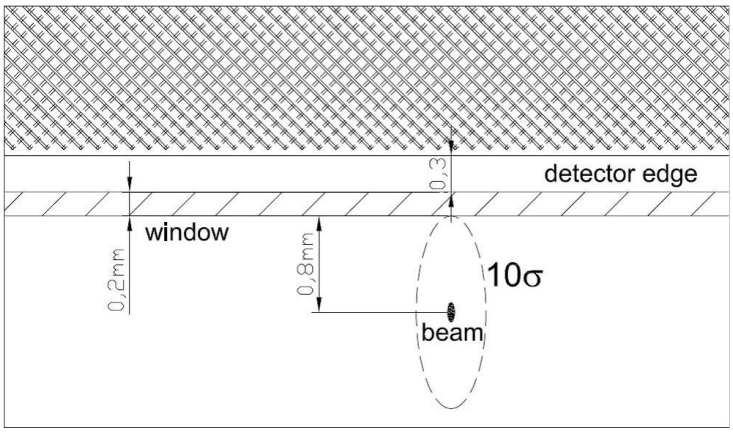

Figure 19. Transverse distance of detector from the beam, showing the window of thickness $\sim 200\,\mu$m placed at $10\,\sigma$ (0.8 mm) from the beam [5].

6.2 μstation and Longpot design

The conventional RP design turns out to be impractical due to given space limitations at the 420 m location, where the spacing between the beam pipes is only 194 mm. For beam injection, the active areas of the detectors at 420 m must be kept at $\sim 20-30$ mm away from the beam. When the beams are stable, the detectors must be moved to within ~ 3 mm of the beam, depending on background conditions. The FP420 groups are investigating several possible designs for detector housings, including a μstation or Longpot concepts first developed for the LHC environment by the Helsinki group [5, 47]. In these solutions, each silicon detector and timing detector has an individual movement mechanism similar to a traditional RP design. The designs have the advantage of redundancy, in that a failure of one unit does not compromise FP420 operations. Access to the detectors is also

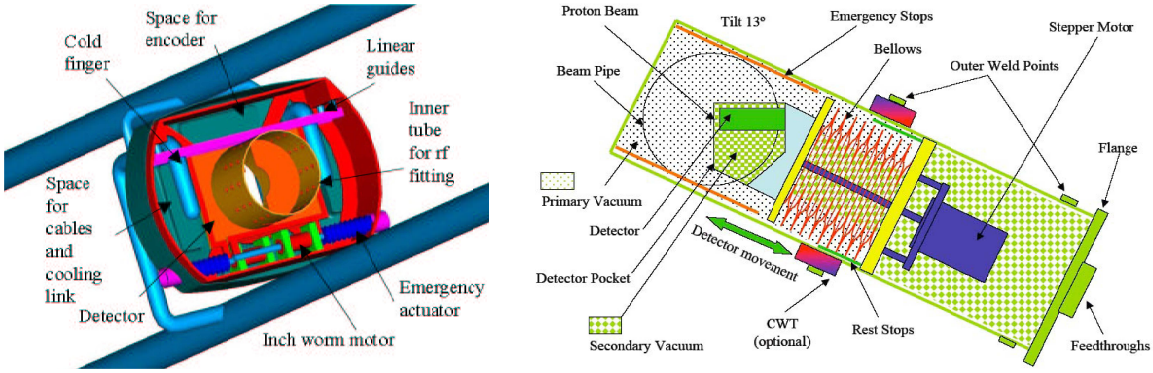

(a) (b)

Figure 20. (a) Schematic figure of the μstation with its connection to the cooling system [5]. (b) Cross-section of the Longpot design with the primary and secondary vacuums drawn [47].

potentially easier through the secondary vacuum arrangement as shown in Figs. 20(a) [5] and 20(b) [47].

The μstation detector unit is assembled on the beam pipe and consists of five subsystems: the vacuum chamber, the support structure, the detector element, the driving mechanism and the cooling system. The unit includes moving silicon strip sensor planes with their support and cooling system inside a vacuum chamber welved to the beam pipe. The sensor planes with high positioning resolution ($\sim 10\,\mu$m) can approach the beam with two linear stepping motors mounted side by side.

In the Longpot design, the stepper motor with all its connection cables is used inside the secondary vacuum. This arrangement allows the maintenance and repair of the detector unit easily without breaking the primary vacuum. In addition, emergency stops are included on each side of the detector element.

6.3 Detector requirements

As motivated in the last two chapters, the detection of the leading protons at very small scattering angles ($|\eta| \approx 10$) with a good spatial resolution is essential for study of the hadronic diffraction and new physics. The forward detector edges have to approach as close as possible to the beam to obtain a good acceptance for the protons with a small fraction of the momentum lost (ξ-values).

The main detector requirements are [5, 45]:

- A dimension of the active detector area of order of $\sim 3 \times 3\,\mathrm{cm}^2$.
- A good spatial resolution of order of $\sim 10\,\mu$m is required to obtain the mass of the central system with an accuracy of order of 1 GeV by using the Missing Mass method.
- A minimized dead space at the detector edge (edgeless design) in order to approach the beam as close as possible with a full detection efficiency. For the TOTEM detectors at

220 m, the full efficiency up to less than 50 μm from their physical edge is required [49]. In the FP420, it is desirable that the dead space is even smaller, say 10% smaller than that (50 μm) of the TOTEM design.

- An improved detector radiation hardness *i.e.* the ability to withstand a total (10 yr) particle fluence of $\sim 10^{15}\, n_{eq}/\mathrm{cm}^2$ corresponding to a radiation dose of about 50 Mrad. For the SLHC, the radiation hardness requirements are extended up to $\sim 10^{16}\, n_{eq}/\mathrm{cm}^2$.

6.4 Radiation hardness

Proper operation of a semiconductor detector depends on the quality of the crystal lattice. A poor quality crystal with many defects can lead to high leakage currents and incomplete charge collection due to trapped charge carriers [50]. The hard radiation environment causes damage to the radiation sensors via two basic mechanisms:

- **Bulk damage** is caused by the non-ionizing interactions of the high energy particles, such as hadrons or γ-rays, which displace lattice atoms from their lattice sites. A single displacement produces a Frenckel pair, which is a pair of an interstitial atom and a left-over vacancy. For neutrons and electrons in silicon, the threshold energies for the Frenckel pair formation are 170 eV and 260 keV, respectively. The low energy recoil atoms, just above the threshold, will most probably create point effects and the ones with high energy can displace more atoms from their lattice sites before stopping. These displaced atoms can still have energy for further displacements introducing a cascade of displacements, which forms defect clusters at the end of the track of the primary atom displaced. The threshold energies in silicon for the cluster production are $\sim$ 35 keV for neutrons and $\sim$ 8 MeV for the electrons [51]. Fig. 21(a) shows a simulat of creation of clusters in silicon.

- **Surface damage** is caused by the ionizing radiation that creates holes (build-up charge) in the surface oxide layers of the sensor. The holes get trapped in the oxide or interact with the atoms at the surface interface to form interface states. The trapping results in an increase of positive charge in the oxide and therefore degrades the oxide quality, while the interface states produce new energy levels in the forbidden band gap [52].

In general, the bulk damage leads to degradation of the energy resolution of the sensor due to fluctuations in the amount of charge lost, and the surface damage leads to an increase in the leakage current and thus also contributes to the energy resolution [50]. The bulk damage is a limiting factor for the use of silicon detectors in the intense radiation fields that are present in the LHC and especially in the SLHC.

The point defects, interstitials and vacancies, are essentially unstable and mobile at room temperature and most of the vacancies recombine with the interstitials. When the point defect energy levels are in the forbidden gap they are generally acceptor-like or donor-like traps. In thermal equilibrium the Fermi level, whose position in the bandgap depends on the type of material (resistivity) and temperature, determines the electric state of the

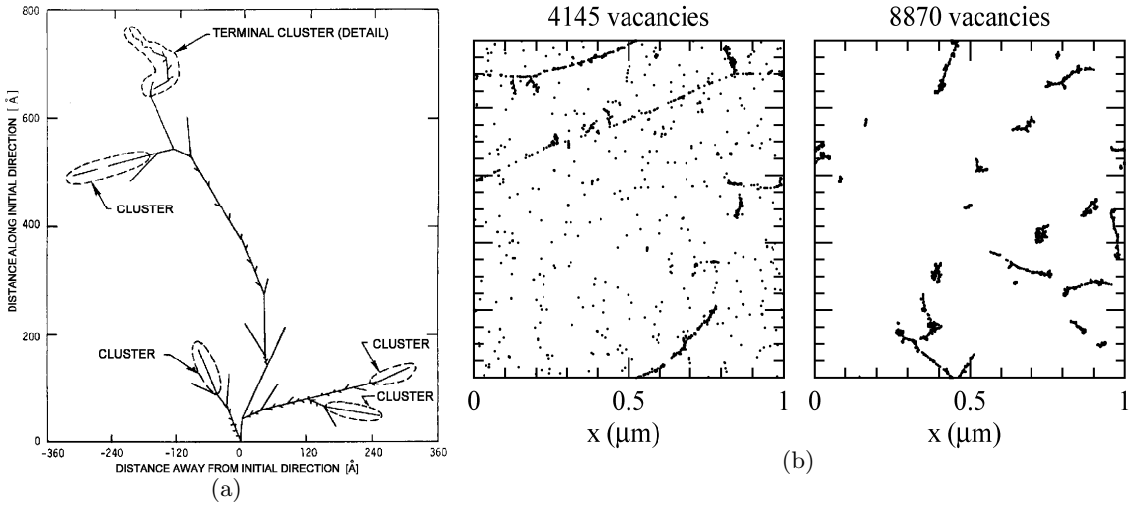

Figure 21. (a) Monte Carlo simulation of a recoil-atom track with a primary energy of 50 keV [53]. (b) Initial distribution of vacancies produced by 24 GeV protons (left) and 1 MeV neutrons (right). The plots are projections over 1 μm of depth z and correspond to a fluence of $10^{14}\,\mathrm{cm}^{-2}$ [54].

defects. If the defects are ionized at room temperature they are in general called shallow levels. When the acceptors or donors are filled with a hole or an electron, respectively, they are called deep levels or carrier traps.

Very little is known about the topology of clusters, which are a composition of vacancies and interstitials, as well as the nature of defects inside the clusters and their electrical properties. The clusters are thought to be responsible for the significant differences seen in the damage produced by light particles and heavy particles. Light particles such as photons, as well as low-energy electrons, produce only point defects; low-energy protons (< 50 MeV) produce both clusters and point defects; high-energy protons produce mostly clusters and neutron irradiation mainly clusters [54].

6.4.1 NIEL hypothesis

The Non Ionizing Energy Loss hypothesis (NIEL) allows the comparison of different particle irradiations with a different energy spectrum in terms of the amount of damage or displacement generated [55]. The NIEL states that for each type of incident particle, the amount of displacements-damages induced in the material scales linearly with the amount of energy imparted in the collision. To scale the damage, one generally refers to 1 MeV neutrons, and a given fluence Φ of a given particle can be correlated to an equivalent fluence of 1 MeV neutrons $\Phi_{eq}^{1\,\mathrm{MeV}}$ by

$$\Phi_{eq}^{1\,\mathrm{MeV}} = k\Phi, \tag{30}$$

where k is the hardness factor. On the basis of the NIEL scaling, the damage efficiency of any particle with a given kinetic energy E can be described by the hardness factor k,

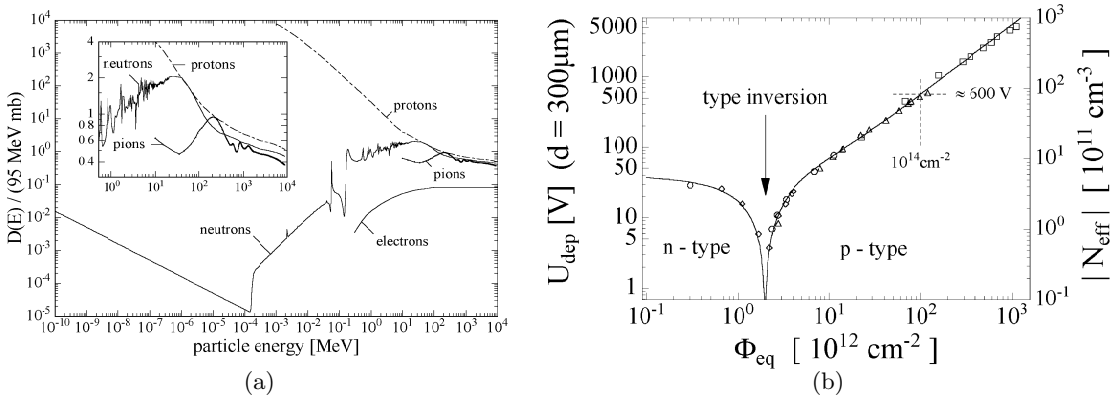

(a) (b)

Figure 22. (a) Displacement damage function $D(E)$ normalized to 95 MeVmb for neutrons, protons, pions and electrons [55]. (b) Change in the depletion voltage with respect to the absolute effective doping concentration, measured right after the irradiation [56].

defined as

$$k(e) = \frac{D(E)}{D_n(E = 1\,\mathrm{MeV})}, \tag{31}$$

where D is the displacement damage cross-section of the particle and D_n the displacement damage cross-section for 1 MeV neutrons. By the ASTM standard, D_n is set as a normalizing value $D_n(E = 1\,\mathrm{MeV}) = 95$ MeVmb. That is, any particle fluence can be reduced to an equivalent 1 MeV neutron fluence producing the same bulk damage in the specific material. From Fig. 21(b), the NIEL scaled hardness factor k for 24 GeV protons can be calculated to be ~ 0.5. The full energy range displacement damage function of different particles is shown in Fig. 22(a).

6.4.2 Radiation damage effects to the radiation detectors

The full depletion voltage V_{fd}, *i.e.* to fully extend the electric field throughout the depth d of an asymmetric junction diode, is related to the effective doping concentration N_{eff} of the bulk by

$$V_{fd} = \frac{e}{2\epsilon\epsilon_0}|N_{eff}|d^2, \tag{32}$$

where e denotes the elementary charge and $\epsilon\epsilon_0$ the permittivity of the semiconductor. With defects introduced by radiation, the value of N_{eff} changes, changing V_{fd}. Eq. 32 holds not only for the original n-type silicon with N_{eff} governed by an abundance of donors, but also after severe irradiation when the effective doping concentration changes its sign, due both to a "donor removal" and to the increasing generation of acceptor-like defects. This is later referred to as the space charge sign inversion (SCSI). In any case $|N_{eff}| = |N_d - N_a|$, with N_d being the donor-concentration and N_a that of the acceptors. The devices experience first a period in which N_{eff} is reduced, called annealing, then a reversal of this effect resulting in a further increase in N_{eff}, called reverse annealing. The irradiation induced type inversion of originally n-type silicon is shown in Fig. 22(b).

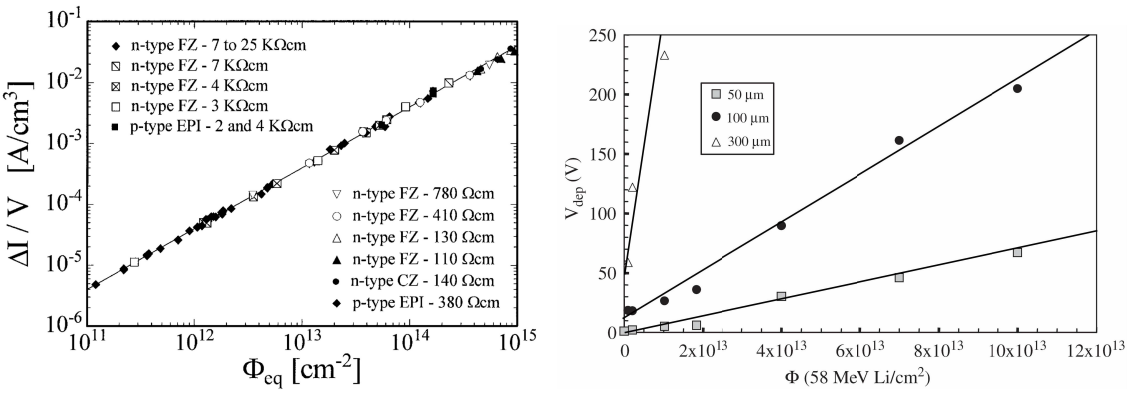

(a) (b)

Figure 23. (a) Fluence dependence of leakage current for detectors produced by various process technologies from different silicon materials. Labels "FZ" stand for Float Zone silicon process, "CZ" for Czochralski silicon process and "EPI" for epitaxially grown silicon process [51]. (b) Depletion voltage as function of the 58 MeV Li-ion fluence for diodes of different thickness: 50 μm (squares), 100 μm (circles) and 300 μm (triangles). The trend lines are drawn posteriorly in the figure [57].

The leakage current originated from the depleted bulk of the reverse biased planar diode is approximated by

$$I = \frac{en_iV}{\tau_g}, \tag{33}$$

where n_i is the intrinsic carrier density and τ_g is the generation lifetime of the semiconductor. The bulk damage induced increase of the reverse current exhibits a simple dependence on particle fluence and temperature. It is entirely due to the generation of electron/hole-pairs in the silicon bulk. The generation centers also serve as recombination centers or traps for electrons and holes.

The reverse current I at full depletion is directly proportional to the sensitive volume V of the bulk and to the equivalent fluence Φ_{eq} that the detector has received:

$$I = \alpha\Phi_{eq}V, \tag{34}$$

where α is a current related damage rate. The linear increase of the leakage current as function of fluence is presented in Fig. 23(a). Combining Eqs. 33 and 34, the effective damage constant β (trapping time damage constant) is defined as

$$\frac{1}{\tau_{n,p}} = \frac{\alpha}{en_i}\Phi_{eq} = \beta_{n,p}\Phi_{eq}, \tag{35}$$

where the effective trapping time and damage constants are defined separately for electrons (n) and holes (p) [57]. Eq. 35 shows that the trapping time decreases as a function of the fluence, and since also the charge carrier mean free paths ($L_{n,p} = v_{n,p} \cdot \tau_{n,p}$) reduce. At SLHC fluences, with electron and hole saturation velocities, the carrier mean free paths

are saturated even below 30 μm, *i.e.* the charge collection efficiency cannot be improved by increasing the electric field in the diode.

The advantages of thin detectors (thickness of the active volume $d < 300\,\mu$m) are the lower leakage current (from Eq. 33, $I \propto d$) and depletion voltage (from Eq. 32, $V_{fd} \propto d^2$) after irradiation. Moreover at the SLHC fluences, charge collection is limited by the carrier mean free path ($\sim 30\,\mu$m), rather than by the thickness of the active volume, which can be decreased without affecting the charge collection efficiency (CCE). The advantage of substrate thinning in order to limit the depletion voltage increase after SCSI is clearly shown in Fig. 23(b). The 58 MeV Li-ion radiation source has been considered in order to reach a high level of bulk damage in the silicon substrate at moderate irradiation fluences [57].

Chapter 7

3D detector concept

The bipolar transistor, invented by a research team at Bell Laboratories in 1947, and the discoveries of other semiconductor devices during the early 1950s and 1960s, created an avalanche of semiconductor device research and fabrication. In the 1980s, important milestones were reached in the development of radiation detection. In 1980, the first high precision microstrip detector was manufactured using the surface barrier technique [58]. At the same time, the planar fabrication technology of the passivated planar silicon diode structure allowed low leakage currents and well-defined electrical contacts [59]. Development of Very Large Scale Integration (VLSI) equipped silicon detectors with advanced readout electronics. The integrated design has a wide range of applications, such as vertex detectors in collider experiments or silicon pixel devices used in medical X-ray imaging.

For more than two decades, sensors and their readout chips have been fabricated using planar technology [59], in which all the fabricated structures lie within a few microns of either surface. These sensors employ silicon diodes with electrodes in the form of closely spaced strips or pixels, with p-type electrodes on one surface and n-type ones on the other side. When reverse biased, they form a depleted diode with an electric field between the p- and n-electrodes for charge collection of incident ionizing radiation.

7.1 Full 3D detector design

S. Parker proposed a 3-dimensional (3D) detector in 1995 [60] and C. Kenney detectors with active edges in 1997 [61]. This technology, which combines micro-machining and standard VLSI processing, takes full advantage of the development of high precision etching techniques in silicon. Contrary to the standard planar silicon configuration, in 3D design the electrodes are processed inside the bulk of the silicon wafer instead of being implanted on its surface. Fig. 24(a) depicts an example of a 3D detector with an active edge and Fig. 24(b) the general structure and operation of the planar and 3D detector concepts.

As a consequence of the novel approach, the spacing of the electrodes is not limited by the thickness of the wafer and can be determined by the required spatial resolution of each application. The spacing of electrodes of 50 μm can be reached and with the intrinsic benefits of the 3D design:

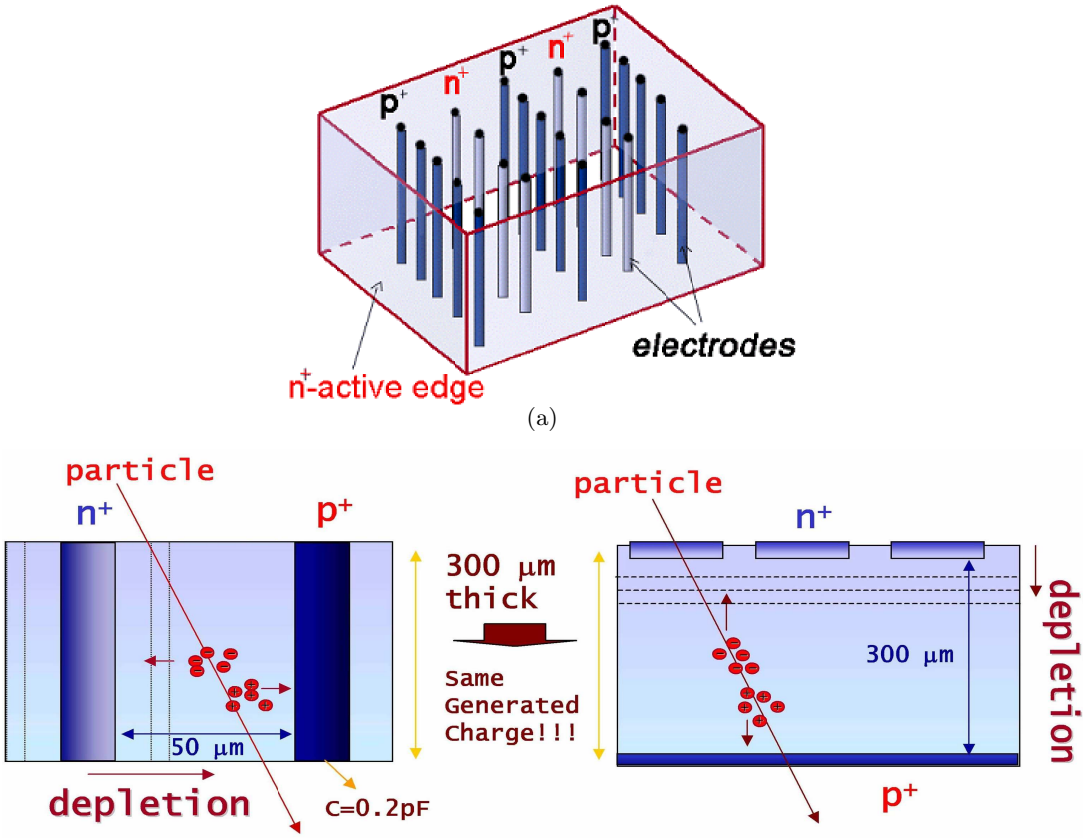

Figure 24. (a) Example of a 3D detector with an active edge surrounding the bulk. The vertical electrodes are ordered in columns. (b) A cross-section of the 3D detector (left) compared with a standard planar detector (right). The same charge generated by a traversing ionizing particle is collected by a 3D detector over a much shorter distance over a shorter time interval, and with the full depletion bias voltage about one order of magnitude lower [62].

- a factor 10 faster pulse and a higher average electric field for any given maximum applied field;
- a low depletion voltage enable sensors to be used in portable devices and improve the signal-to-noise ratio due to low power consumption and leakage current, respectively;
- the sensitive volume of the detector can be increased by adding the detector thickness and without augmenting the depletion voltage;
- a moderate full depletion voltage, high charge collection efficiency and capability for room temperature operation after heavy irradiation is maintained;
- an advanced fabrication process provides high charge collection efficiency close to the edge of the sensor, "edgeless design".

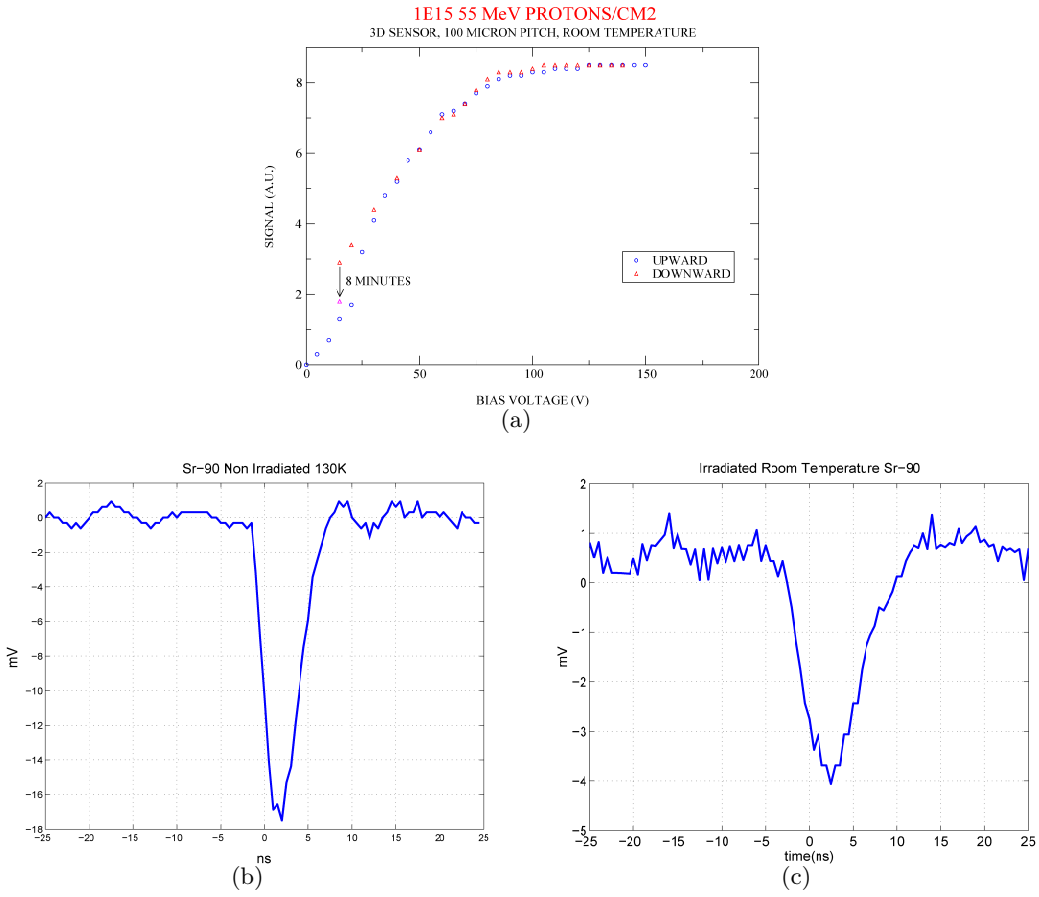

Figure 25. (a) Measured depletion voltage of $\sim$ 105 V after irradiation by 10^{15} 55 MeV protons/cm^2 (equivalent to 1.8×10^{15} neutrons/cm^2) in sensors without added oxygen and without annealing [62]. Oscilloscope traces of ionizing particle signals in two 3D detectors operated at 130 K and 300 K before (b) and after (c) heavy irradiation. The bias voltage is 40 V in both cases, and the rise times are 1.5 ns with a pulse duration of 5 ns, and 3.5 ns with a pulse duration of 10 ns [62].

In Publications II and III, finite element (FE) device simulations of a 3D detector structure were performed. The electrical and charge collection characteristics were shown to be similar to what is suggested in the early papers [60, 61]. In Publication III, the charge collection process in the peculiar 3D electrode structure was found to be delayed due to an induced internal resistance-capacitance (RC) constant.

A full depletion voltage of 105 V has been measured for a 3D test device after hard irradiation with 55 MeV protons at a fluence of 10^{15} protons/cm^2 as shown in Fig. 25(a). The 3D detectors are expected to survive beyond 5×10^{15} neutrons/cm^2, particularly if oxygen enriched substrates and electron signal readout are employed [62].

At present, the charge collection efficiency has been measured to be 60% for a detector irradiated up to 10^{15} protons/cm^2 with a bias of 40 V [62]. Figs. 25(b) and 25(c) show signals from a minimum ionising particle before and after such a fluence and ensure that the 3D detectors are well operational in a hostile radiation environment.

7.2 Planar-3D detectors

Commonly the separation of planar detectors is done by sawing along the edge of the detector. The result of the dicing is depicted in Fig. 26(a). The detectors are designed to keep the electric field away from the diced sensor edges, that are electrically conducting due to numerous unfilled crystal bonds. A large inactive space is required to keep the field region away from any cracks and chips caused by the saw blade. The space is typically some tens of microns from the saw edge. Some space must also be reserved for the guard rings, which lower the voltage in a controlled fashion and intercept leakage currents coming from the detector edge.

By adding a few 3D process steps such as deep-etching, dopant inclusion and diffusion into the planar process, the dead space and cracks in the sensor edges can be avoided. The final dicing of the sensors is done by etching instead of sawing. This allows the edges of the sensor to form an extension of the backside electrode, as schematically shown in Fig. 26(b). In this configuration, dead space is not needed to avoid extension of the electric field lines to the saw edge. The advantages are that the surface leakage current is greatly suppressed and the dead space is reduced to no more than a few microns as shown in Fig. 26(c). In a recent study [63], the sensor was found to be fully active from about 5 μm from the physical edge. A drawback of the planar-3D design is that the bottom edge corner is very difficult to deplete with the planar structure.

7.3 Semi-3D detector design

Publication IV introduces the structure, fabrication process and preliminary characterization of a novel semi-3D detector proposed for particle tracking in high irradiation environments. Publication V presents more advanced characterization results and compares them with the simulations. Expected properties of the semi-3D design are verified.

The structures were fabricated on the n-type high resistivity Float Zone (FZ) silicon wafers with resistivity above 6 kΩcm and crystal orientation $< 111 >$. For comparison, a few Czochralski (CZ) silicon wafers with the resistivity of 1 kΩcm and $< 100 >$ orientation were included in the process. These were the first 3D detector structures ever fabricated at VTT. Consequently, the second fabrication run of the semi-3D detectors was done only on the FZ-silicon wafers and was devoted to studying the design's imaging properties. As presented in Publication VI, the semi-3D structure with a pixel pitch of 55 μm was fabricated and bump-bonded to a Medipix2 readout chip. This section represents the semi-3D structures and describes some aspects of the fabrication process that are not present in the publications. The following chapters describe the characterization methods and summarize the most important results of publications II-VI.

The basic idea of a semi-3D detector design is to increase radiation tolerance, to lower power consumption and to simplify the 3D fabrication process, while keeping the spatial resolution and radiation attenuation depth similar to the planar or full 3D detectors. The expected increase of the radiation hardness with the proposed design is based on the fact that thinner detectors tolerate more irradiation than thicker ones, as described in Section 6.4.

Fig. 27(a) shows a block diagram of a pixel of the first fabricated semi-3D test structures, where each pixel is connected in series with the neighboring ones. The pixel pitch, depth

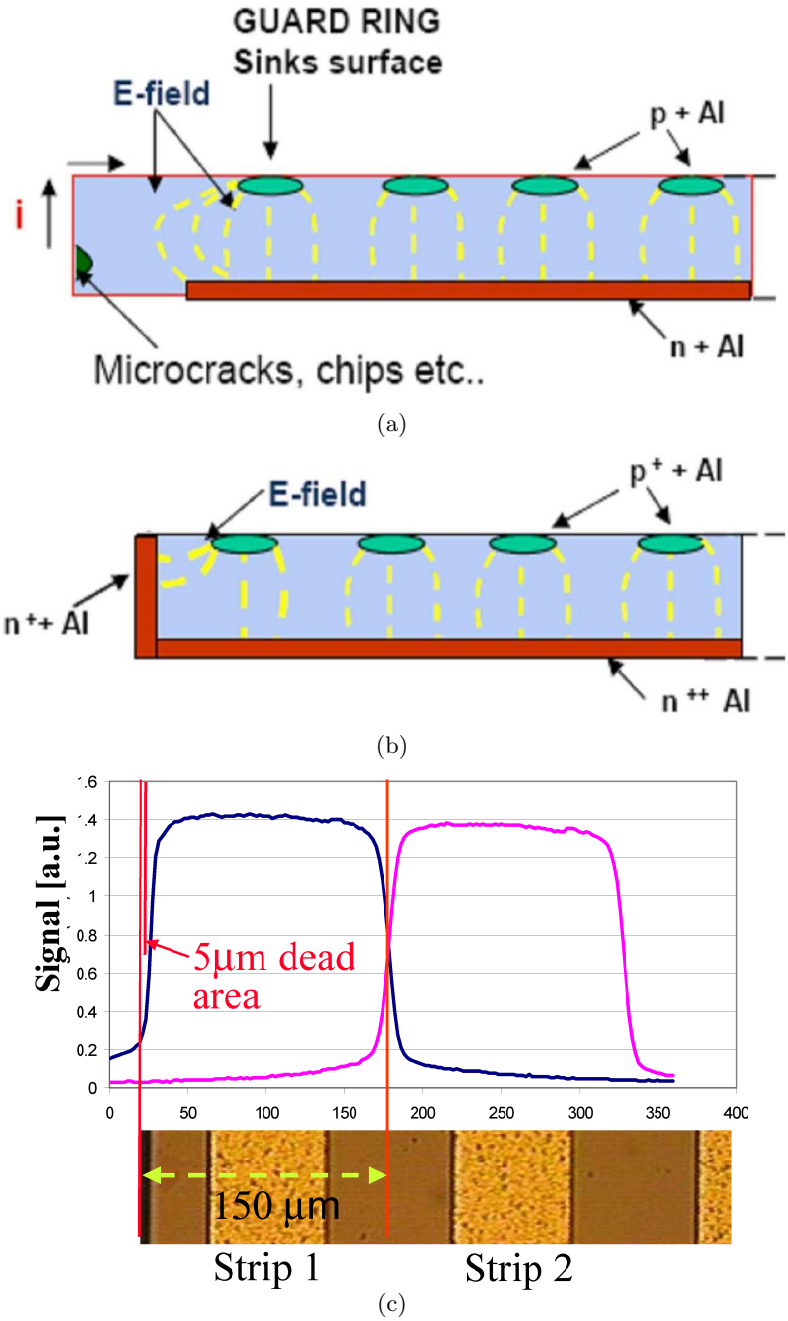

Figure 26. (a) Schematic cross-sectional view of the edge of a planar sensor. An insensitive region is required for the guard rings and to eliminate the bulk electric field that could reach the saw edge. (b) A planar-3D detector, where the final dicing of the sensor is done by anisotropic etching, avoids the problems of (a). (c) Signal from the edge and next-to-edge channels as the sensor is scanned across an X-ray micro-beam. The rapid turn-on at the left edge is clearly seen. The tails come partly from the back-scattering of penetrating X-rays, and at the channel 12 border, partly from diffusion along the charge collection path [63].

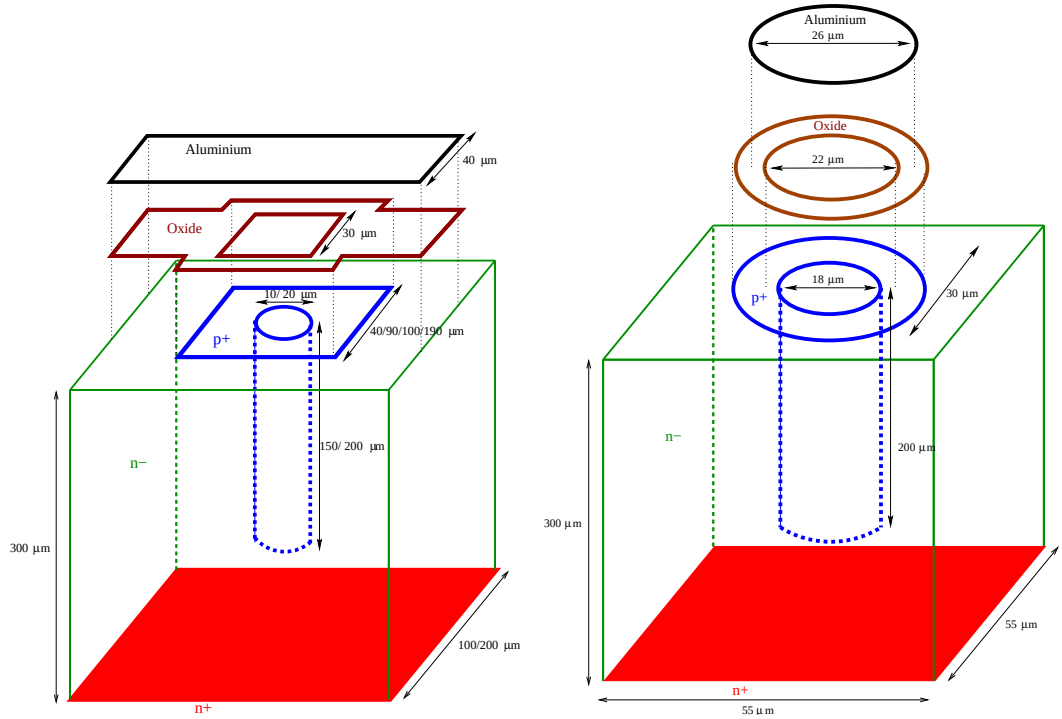

Figure 27. (a) Block diagram of a pixel of a semi-3D strip detector designed at VTT. Each pixel is connected in series by an aluminum strip. (b) Block diagram of a semi-3D pixel detector to be connected with Medipix2 readout chip.

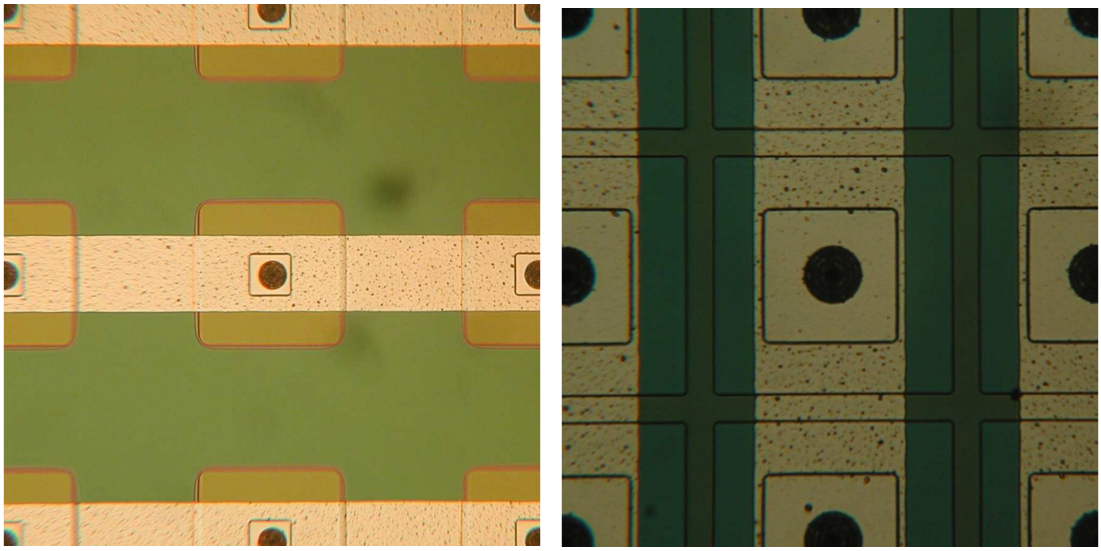

(a) (b)

Figure 28. Photographs of pixels of a semi-3D strip detector fabricated at VTT. Each pixel with pitch of 100 μm is connected in series by an aluminum strip. (a) The pillar electrode diameter is 10 μm (150 μm electrode depth) and the implant size is 40 μm. (b) The pillar electrode diameter is 20 μm (200 μm electrode depth) and the implant size is 90 μm.

and implant size of the p-type electrode were varied as shown in the figure. The electrode depths of 200 μm and 150 μm correspond to electrode diameters of 20 μm and 10 μm, the ICP-etching depth-to-diameter aspect ratios are 10:1 and 15:1. The present devices were not optimized for any particular application, but the work merely presents a demonstration of the technology. The area of the fabricated test structures ranged from 0.5×0.5 mm^2 (5 pixels with pitch of 100 μm per one column) to 2×2 cm^2 (100 pixels with pitch of 200 μm per one column).

Fig. 27(b) depicts a block diagram of a semi-3D pixel that can be connected to the Medipix2 readout chip by bump bonding. No variations in the pitch (fixed by the readout chip), electrode depth or implant size were done. The depth-to-diameter aspect ratio of the electrode holes in the design is about 11:1, and thus a lot of space within the pixel is reserved for the electrodes. Fig. 28 shows photographs of fabricated pixels of the layout in Fig. 27(a) with a pixel pitch of 100 μm and electrode diameter of 10 μm (150 μm electrode depth). In Fig. 28(a) the implant size is 40 μm and in Fig. 28(b) 90 μm.

Even bigger semi-3D structures than 2 cm^2 have been successfully fabricated at VTT. Detectors as big as 3.4×3.4 cm^2 for the TOTEM experiment were made as shown in Fig. 29. Photographs of the fabricated AC-coupled semi-3D strip detector are shown in Figs. 29(c) and 29(d). The layout is similar as shown in Fig. 32(a) but the n-type electrode pillars and active edge are omitted and a uniform n-type doping is introduced on the backside of the device. The omitted active edge is also seen in Fig. 29(c) as an absence of the current terminating ring, which in a testing situation might cause high leakage currents from the saw edge. The detector design has not been characterized yet.

For fabrication of large area semi-3D devices with a high fabrication yield, the crucial steps

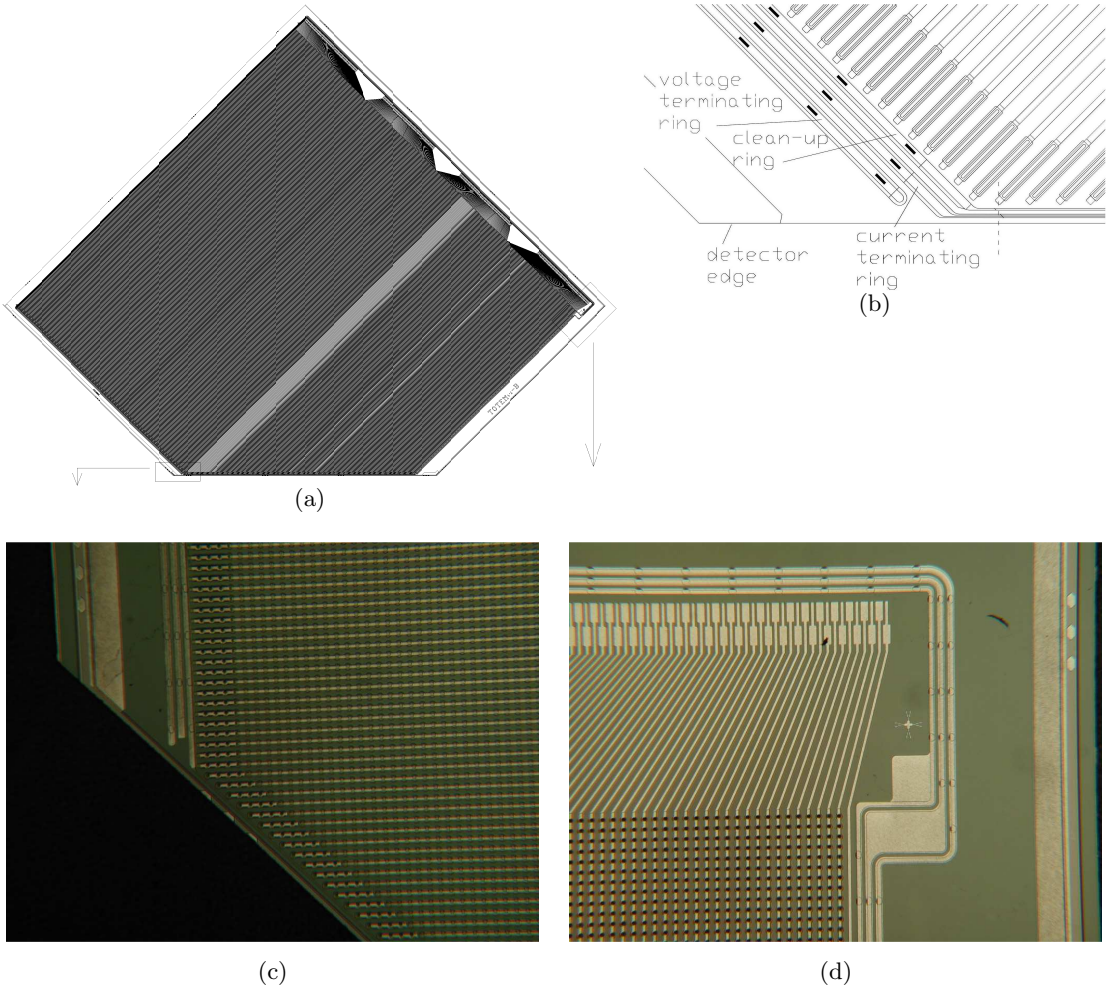

Figure 29. (a) Full layout of the TOTEM (3.4×3.4 cm^2) planar microstrip detector. A pitch adapter is integrated on the detector and the 512 strips spaced at a pitch of 66 μm are ordered in 4 groups of 128 strips for bonding on the APV read-out chips. The pitch adaptation from the strip pitch of 66 μm to the pitch of 48 μm of the front-end electronics is done on the detector. (b) Enlargement of the original layout of the current terminating structure at the detector bottom edge. (c) Photograph of the part shown in (b) of a fabricated semi-3D detector. The absence of the current terminating ring is visualized. (d) Photograph from the top right-hand corner of (a) shows a group of semi-3D strips, their bonding pads and the bonding pads of both the unused current terminating ring and the clean-up ring.

are the ICP-etching and hole filling. The ICP-etching depth-to-diameter aspect ratios used in fabrication of the introduced detectors are not close to the limits of the capabilities of the etching method.

Chapter 8

3D detector fabrication

8.1 The planar process

The basic process steps used in the fabrication of silicon microstrip detectors with standard planar technology are shown in Fig. 30. The process starts with oxidation of polished and thoroughly cleaned silicon wafers (a) at temperatures above 1000°C. The main effect of the oxidation is the elimination of surface leakage current, and is also called passivation. The oxide layer protects the wafer during the processing and, later on, the detector itself from contaminations (b).

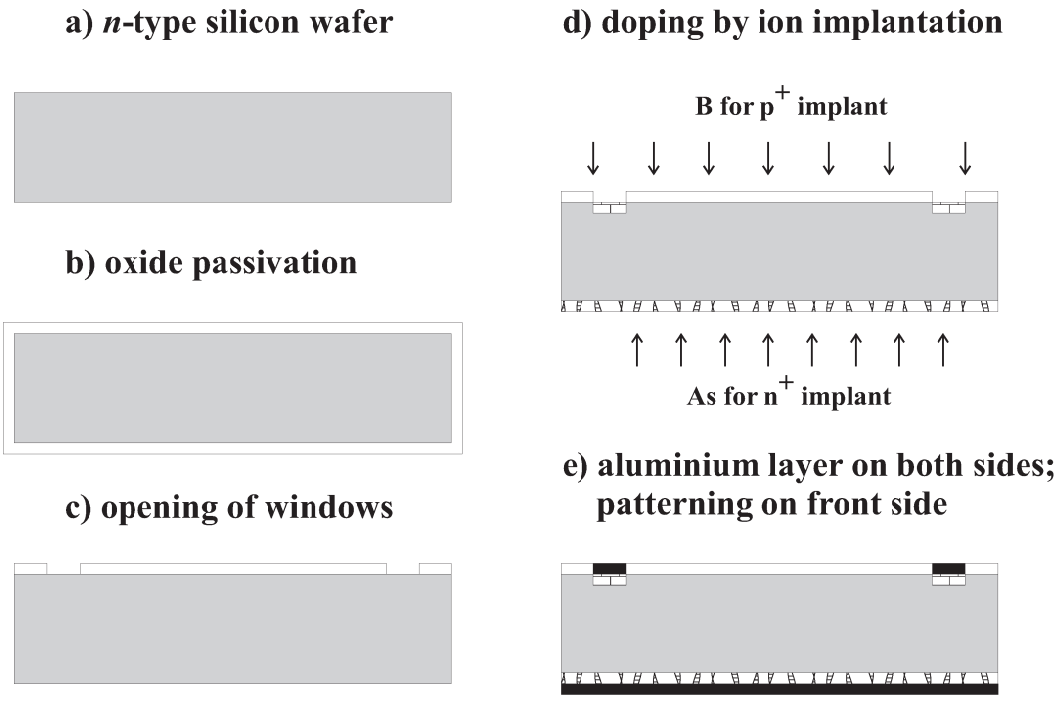

Figure 30. Steps in fabrication of passivated planar silicon diode detectors [59]. Also phosphorus (P) is commonly used for n-type doping in (d).

Next a photoresist is applied on the surface of a wafer and ultraviolet light is exposed on

the wafer through a mask for the desired patterning. Using a developer the exposed part of the resist is dissolved. Windows into the oxide are opened in this way for an upcoming doping process. The patterned oxide mask protects the rest of the surface (c). Phosphorus or arsenic are used for the n-type doping (contact) and for the p-type doping; the implanted ion is boron (d). After implantation, the wafers are annealed at high temperature to anneal the radiation damage in the implanted layers and to diffuse the dopants. The depth of the doped regions typically does not exceed 1 μm. The final full wafer process step is the creation of a metal pattern by photolithography. Typically aluminum or gold are used to obtain good electrical contacts (e). The final sensors are cut from the wafer by a diamond saw.

8.2 3D detector fabrication

The fabrication of 3D detectors uses the ability to bond wafers together, to etch deep holes with vertical side walls and arbitrary cross-sections, to dope the walls, and to fill them uniformly from top to bottom. Doped holes are necessary because diffusion of deposited dopant molecules on the top or bottom surfaces cannot produce narrow columns, and the range of implanted ions is far too short. To use photoresist after the fabrication requires the holes to be filled [60]. Fig. 31 shows the process steps for producing full 3D detectors with active edge and sensor separation by anisotropic etching.

Excluding process steps such as cleaning, photoresists deposition, oxidation and other sub-steps, the following general steps are identified:

1. **preprocessing:** backplane doping, support wafer bonding, thinning, planarization, cleaning, alignment mark mask and etch;
2. **mask 1:** n-type electrode and edge pattern mask and wafer etch-through (a);
3. n^+-type silicon deposition, hole fill and dopant diffusion (b);
4. etching or polishing of the extra deposited silicon from the surface;
5. **mask 2:** p-type electrode pattern mask and wafer etch-through (c);
6. p^+-type silicon deposition, hole fill and dopant diffusion (d);
7. etching or polishing of the extra deposited silicon from the surface;
8. **mask 3:** contact pattern mask and etch (e);
9. aluminum deposition (e);
10. **mask 4:** metal pattern mask and etch (e);
11. **mask 5:** edge pattern mask and sensor dicing by etch-through (e);
12. removal of the supporting wafer and bonding oxide by etching, thus separating the individual sensors (f).

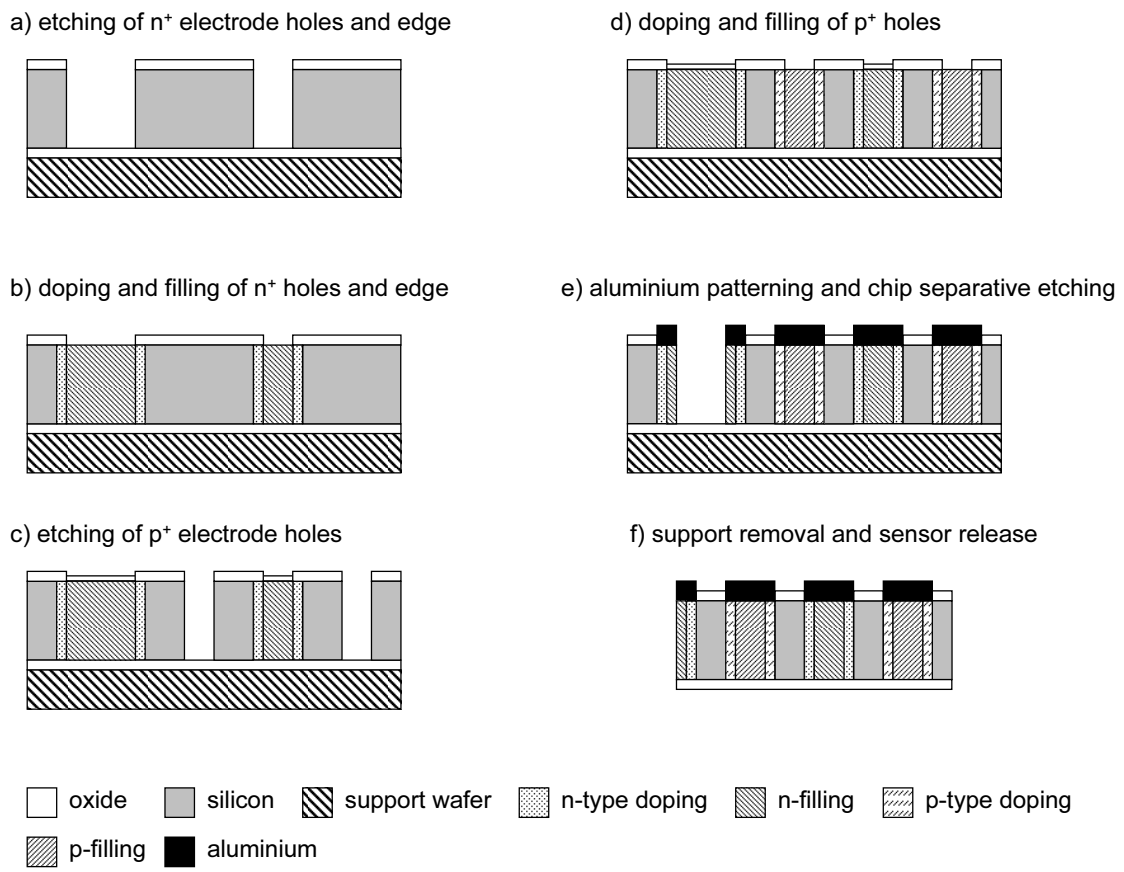

Figure 31. Possible process steps for making a full 3D detector with active edge using a support wafer.

Recently it has been proposed that an additional side wall thermal oxide layer could be used at the edge, between the single- and polycrystalline silicon, as a vertical etch stop [63]. The oxide would be grown after the edge doping before the polysilicon filling.

Another attractive possibility for 3D structure fabrication is to use a single wafer and not to etch the edge trench totally through the wafer. Also the electrode holes can be fabricated in such a way that they penetrate only to a partial depth of the wafer. These are called double-sided 3D detectors. Characterization of a double-sided 3D pixel detector by simulations has recently been described in [64] and their processing is currently in progress [65] in CNM Barcelona. The structure is planned to be connected to the Medipix2 readout chip [66]. Another example of a double-sided 3D strip detector with an active edge is shown in Fig. 32(a). The detectors were proposed for the TOTEM experiment and the fabrication took place in 2005 at VTT.

Making the active edge on the single wafer is not easy, because the wafer easily breaks at the edge. Thus complete trench filling should be performed right after etching to make the wafers durable for the subsequent process steps. Figs. 32(b) and 32(c) show photographs of a double-sided 3D strip detector with an active edge. Unfortunately, the wafers were broken during fabrication due to incomplete filling of an n-type polysilicon.

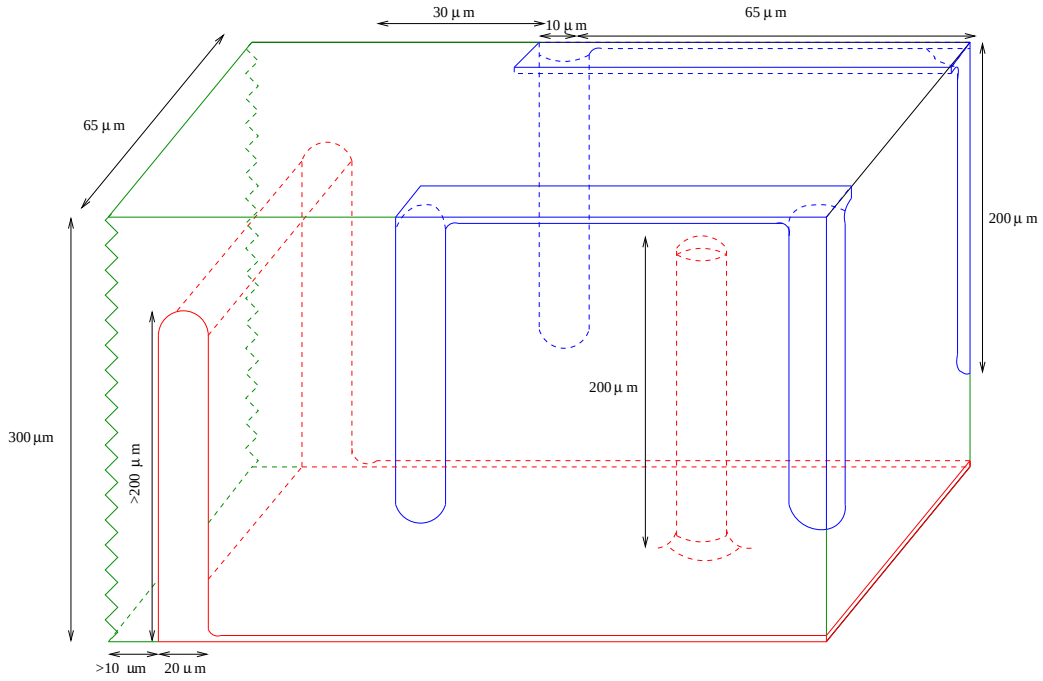

(a)

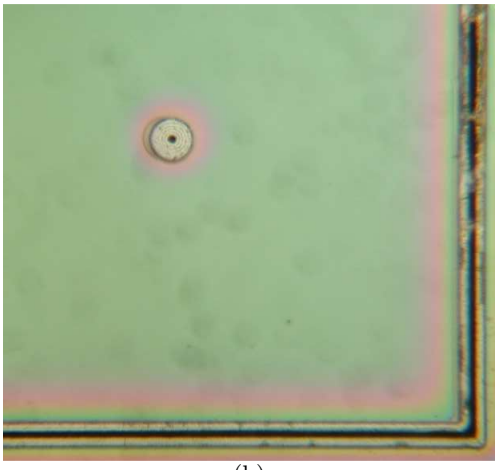

(b)

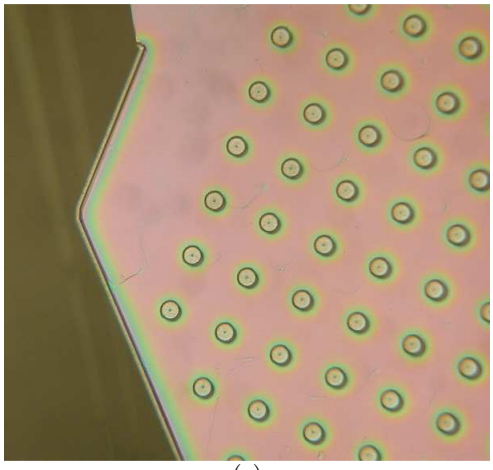

(c)

Figure 32. (a) Double-sided 3D strip detector with an active edge designed for the TOTEM experiment. The bottom of the detector is completely covered by the n-type polysilicon. (b) Photograph of the design shown in (a), from the bottom corner region after n-type polysilicon filling, planarization and wafer breakdown. The picture shows the n-type active edge and the closest n-type electrode pin. (c) Larger photograph of the active edge with plenty of n-type electrodes.

8.2.1 Hole making

The most time consuming and technically challenging task in 3D detector fabrication is the making of vertical electrode holes. Uniformity, depth-to-diameter aspect ratio and quality of the sidewalls are critical parameters that define the properties of the device function. For silicon (and other semiconductor materials) there are three possible techniques for hole making. Their advantages and problems are summarized in Tab. 8.2.1 and explained briefly below [67].

- **Dry etching:** A very powerful technique for its uniformity. A large area of substrate can be etched simultaneously with an etch rate of a few μm per minute, depending on the desired aspect ratio. A major potential limitation in using dry etching is the sidewall damage induced by ion channeling, but in silicon the defects may be annealed out at high temperature. However, this might become a problem for III-V semiconductors such as gallium arsenide (GaAs) due to its compound nature and low melting temperature. Defects and damage can increase the scattering of mobile charges and reduce carrier lifetimes within the material. Another disadvantage is the limited depth-to-diameter aspect ratio. Aspect ratios in silicon as high as 30:1 have been reported in [65]. Figs. 33(a) and 33(d) show top and cross-sectional views of the etched 10 μm holes in silicon, respectively. The holes are made uniformly and without clear damage to the surface or sidewalls [67].

- **Laser drilling:** This technique allows hole drilling with a depth-to-diameter aspect ratio up to 50:1. The main advantage is that laser drilling is independent of the material used. This may be very important for the creation of 3D detectors in new types of semiconductor materials such as CdTe and CdZnTe, which have been extensively studied for medical imaging applications. The technique is limited by its serial process nature; each hole must be drilled separately, while in other techniques the arrays are etched simultaneously. Etching a hole by laser drilling requires 3-5 seconds to be fully completed. Drilling a complete array on a wafer can take hundreds of hours. The drawbacks of the technique are non-uniformity of the hole dimensions, tapering of the holes along its depth and severe sidewall damage. Figs. 33(b) and 33(e) show top and cross-sectional views of the drills 10 μm holes in silicon, respectively. The surface and sidewall damage is clearly present [67].

- **Electrochemical etching:** A very useful technique for obtaining high aspect ratio holes with minimal damage to the sidewall surface. The etching process, different from dry etching and laser drilling, is a chemical reaction together with an electric field that etches the material. In this way, no damage due to channeling or shock waves is induced in the material. Furthermore, high aspect ratios are expected up to 100:1. The electrochemical etching is suitable for both silicon and gallium arsenide with no wafer size limitation. The limitations of the technique are that the shape of the holes is not circular due to the orientation plane of the KOH-etching[1], and there are surface undulations due to the HF-etching. The first distorts the uniformity of the electric field around the holes and thus modifies the charge collection in the detector. The second may be solved by polishing the surface after etching. Figs. 33(c) and 33(f)

[1] Potassium hydroxide, commonly called caustic potash with the formula KOH.

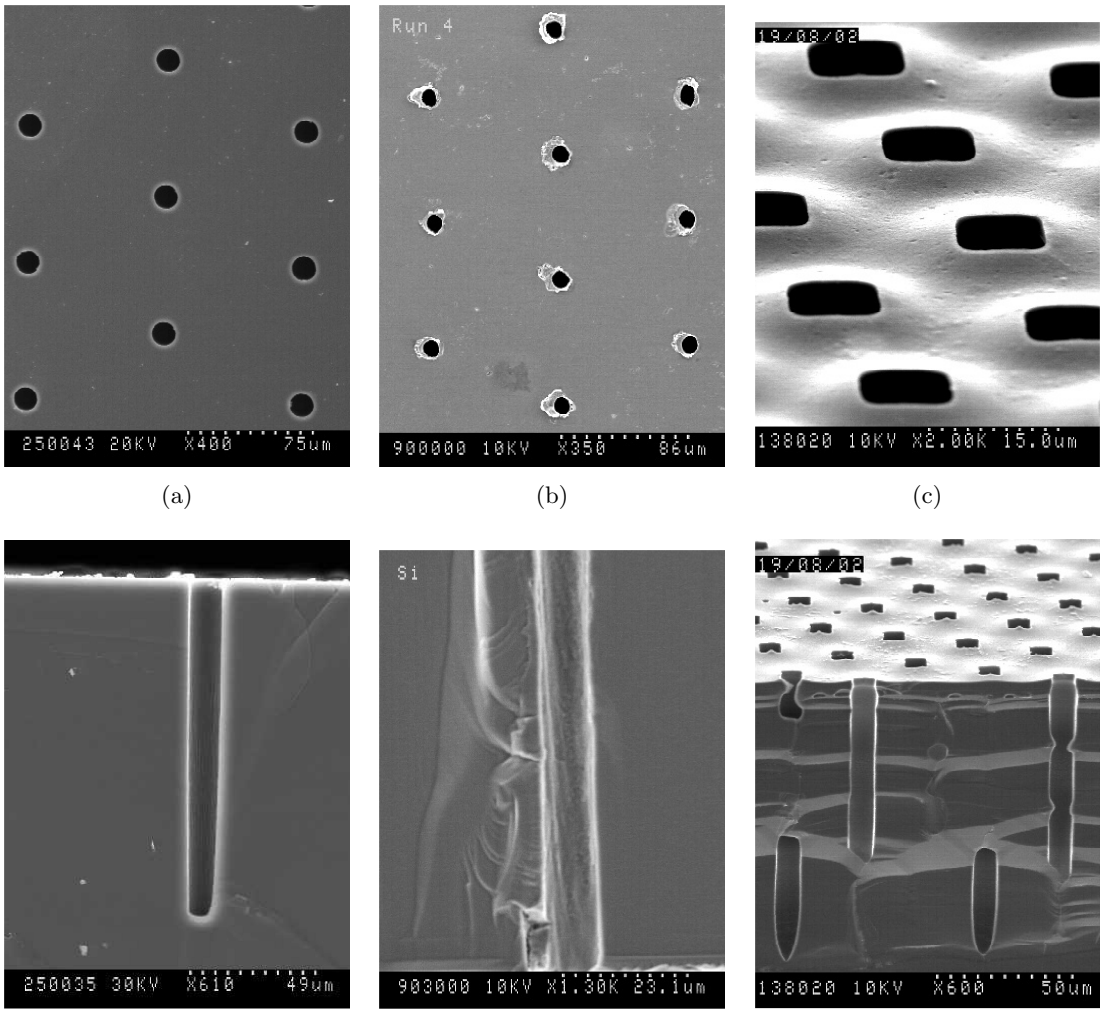

(a) (b) (c)

(d) (e) (f)

Figure 33. Surface view of a hexagonal matrix of holes with diameter 10 μm obtained in silicon by (a) dry etching, (b) laser drilling in optimum laser conditions, (c) electrochemical etching [67]. Cross-sectional view of holes with diameter 10 μm obtained in silicon by (d) dry etching, (e) laser drilling in optimum laser conditions, (f) electrochemical etching [67].

	Advantages	Disadvantages	Etch time
Dry ethcing	- Standard photolithography - Repeatability	- Sidewall damage - Limited aspect ratio - Process available for Si and GaAs	1-4 μm/min
Laser drilling	- Simple photolithography - Any material - High aspect ratio	- Sidewall damage - Repeatability - Slow array process - Tapering with depth	1 hole/3-5 s
Electrochemical etching	- No sidewall damage - Very high aspect ratio	- Bumpy surface - Square holes - Process known for Si and GaAs	0.6 μm/min

Table 7. Currently available techniques for electrode hole making, their properties, advantages and disadvantages [67].

show top and cross-sectional views of the etched 10 μm holes in silicon, respectively. The problematic squared holes and bumpy surface are clearly visible [67].

In this thesis, only the dry etching technique has been considered and presented in more detail. In publications IV, V and VI, hole making was done using Inductively Coupled Plasma (ICP) etching.

8.2.2 Dry etching of holes

The dry etching process follows patterning of the wafer surface by photolithography. Dry etching is commonly preferred to wet chemical etching because of its high anisotropy, greater control and uniformity, the availability of selective etches and ready automation. Plasma is a fully or partially ionized gas composed of ions and electrons. It is produced when an electric field of sufficient magnitude is applied to a gas, causing the gas to break down and become ionized. The electron concentrations in the plasma for dry etching are relatively low, typically on the order of 10^9 to 10^{12} cm^{-3}. At standard pressure, the concentration of gas molecules is roughly 10^4 to 10^7 times higher than the electron concentrations. The average temperature of the gas is in the range 50 to 100°C, therefore dry etching is a low temperature process.

An ICP-etching machine, developed by Surface Technology Systems (STS), is illustrated in Fig. 34 [68]. The machine operation during silicon etching is based on a fluorine chemistry process which alternates etch and passivation steps. The etching and passivation gases are SF_6 and C_4F_8, respectively. The inductively coupled plasma forms fluorine ions from SF_6 and with the aid of an electric field drives them straight down onto the wafer, eventually forming the gas SiF_4 in unmasked parts of the wafer [61]. The etching and passivation steps are described below and shown in Fig. 35 [67, 68].

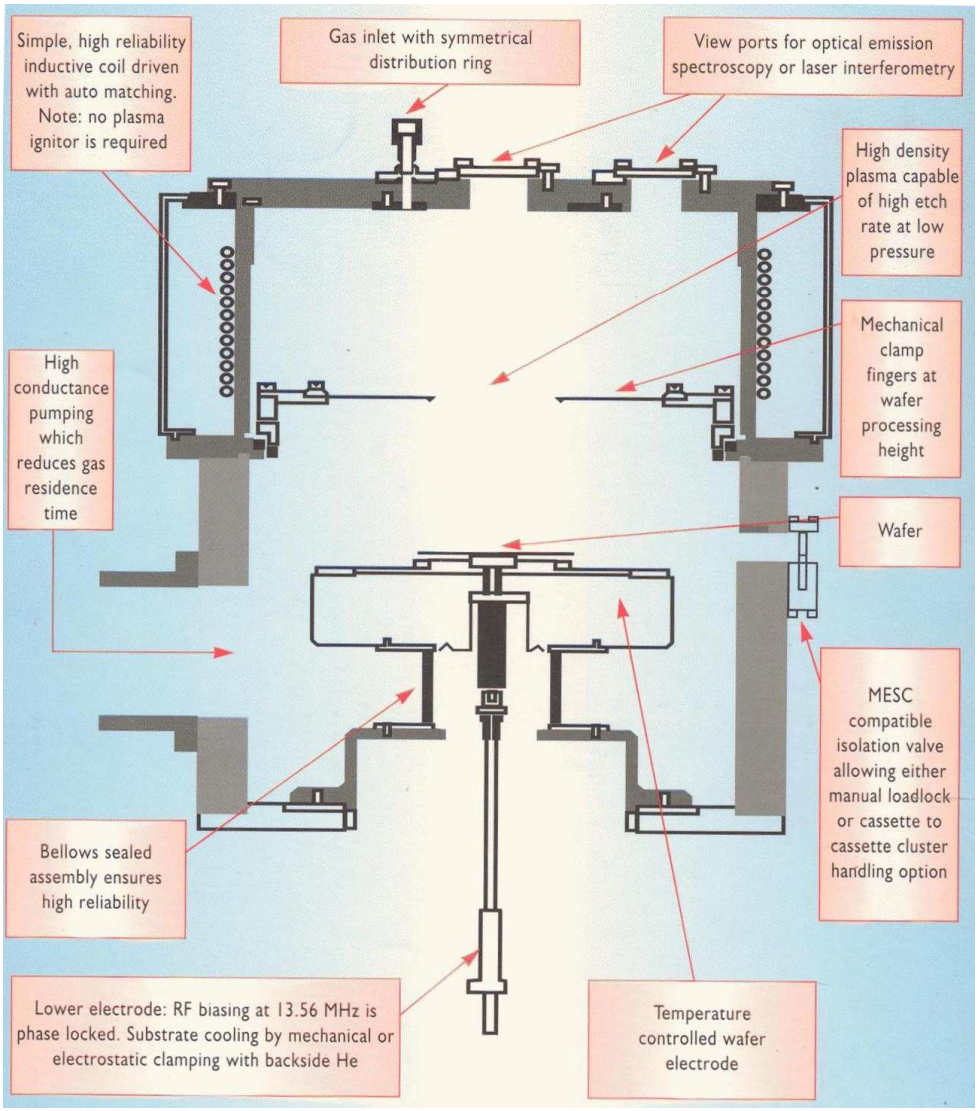

Figure 34. Illustration of Surface Technology Systems' advanced ICP etcher and its parts [68].

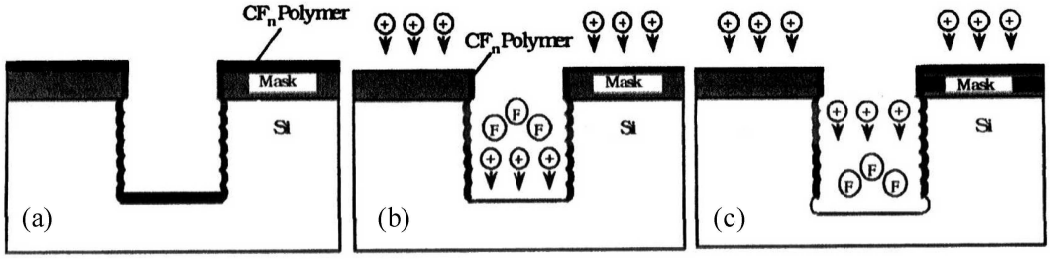

Figure 35. ICP-etching process steps [67].

- **Passivation Step:**
  At the beginning of each cycle, as shown in Fig. 35(a), a C_4F_8-based plasma is used to conformally deposit a few monolayers of Teflon-like fluorocarbon polymer across all surfaces exposed to the plasma.

- **Etch Step 1:**
  The plasma gas is then switched to SF_6 to create a plasma chemistry that isotropically etches silicon. Through the application of a voltage bias to the plate, ions from the plasma bombard the surface of the wafer, removing the polymer as shown in Fig. 35(b). Increased ion energy in the vertical direction results in a much higher etching rate of fluorocarbon from planes parallel to the surface.

- **Etch Step 2:**
  Following selective polymer removal, the silicon surface at the base of the trench is exposed to reactive fluorine-based species that isotropically etch the unprotected silicon, as shown in Fig. 35(c). The remaining fluorocarbon polymer protects the vertical walls of the trench from etching.

- **Repeat steps**

To fabricate high aspect ratio holes in silicon, many different parameters can be varied in the dry etching process, the most important of which include [67]:

1. the gas flow rate, which is essential to keep a fresh supply of etchants in the reaction chamber and also to remove waste products;

2. the pressure of the chamber, which controls how much gas is present in the chamber at any time and affects the plasma density;

3. the RF power, which determines the energy of the ions when they hit the substrate.

The most fundamental issue is the physical constraint of the transport of species into and out of the pore. As the pore becomes deeper, it gets harder to get ions and radicals to the base. Similarly removing the etch product, SiF_4, out of the pore (against the flow of the etchants,) gets harder with increasing depth. This causes slowing of the etch rate and eventual cessation of etching. The most effective way to improve the efficiency of the transport process is to reduce the processing pressure and increase the RF power. Both of these changes adversely effect the selectivity, thus some trade-off is required to achieve deep pores.

For making the edge active structures, the trench width must be chosen so that its vertical etch rate is close to that of the holes. Since both the fluorine and the etching products can enter and leave trenches more easily, the width will normally be smaller than the hole diameter [60]

8.2.3 Hole doping and filling

After creating the array of holes in the substrate, electrodes are formed within the holes to create a radiation detector diode. Two types of contacts can be formed: ohmic (p^+-n junctions) and Schottky contacts.

The Schottky contacts can be satisfactorily formed by evaporating multiple layers of metal onto the semiconductor surface and/or by using a metallic seed layer followed by conformal electroplating to completely fill the holes. In the case of silicon, the ohmic contacts are commonly preferred to the Schottky contacts due to their lower leakage current. To make ohmic contacts in silicon, boron (B) is the most popular dopant for introducing a p-type impurity, while phosphorus (P) and arsenic (Ar) are used as n-type dopants.

The ohmic contacts in silicon can be achived in three ways:

1. **Direct diffusion of impurities** is typically in a furnace by exposing an inert gas that contains the dopant in the holes. The temperature of the process usually ranges between 700 and 1100°C for silicon [69].

2. **Deposition of doped polysilicon** relies on mixing gases like silane (SiH_4), for polycrystalline silicon formation, and dopant gases such as B_2O_3 and B_2H_6 (diborane) for p^+-type doping, and P_2O_5 and PH_3 (phosphine) n^+-type doping. Poly silicon deposited by low-pressure chemical vapor deposition (LPCVD) uses capture and surface decomposition of silane. A conformal coat is formed due to the large mean free path of the silane with respect to the dimensions of the hole, and because the probability of attachment is kept small by the choice of gas temperature. When a silane molecule does interact, this is almost as likely to happen at the bottom as it does at the top of the hole [61].

3. **Spin on glass doping** is done by having a doped liquid source spun onto the surface of the wafer, which is then pulled by capillary forces into the holes. Dopant liquid sources such as borosilica film and phosphorosilica film solution with a concentration of 5×10^{20} cm^{-3} have been used [67]. The liquid is applied by spinning (for 30 s at 2000 r.p.m.) to the oxide coated (SiO_2) substrate that ensures no diffusion into the bulk, only into the holes. Afterwards, the sample is baked to harden the liquid to a semihard thin film.

The holes must be filled with polycrystalline silicon or by other means, so the photoresist could later be spun evenly over the wafer surface for further processing. Also, the poly prevents the photoresist from being trapped in the holes, which is important since it must be removed from the wafer before any high-temperature furnace steps. In addition, if the lifetime in the poly is at least several nanoseconds long, it should be possible to make electrode diameters small enough that one sign of charge generated by ionizing radiation will diffuse out of the electrode into depleted silicon, allowing both signs of the charge to be collected. The charge carrier lifetimes in the electrodes can be increased by recrystallization of the poly silicon at elevated temperatures. It also decreases the mechanical stress caused by the polycrystalline electrodes. If a single crystal silicon could be grown, a radial gradient of dopant density would produce charge collection fields within the electrodes. Fabricating such electrodes has not yet been attempted [61].

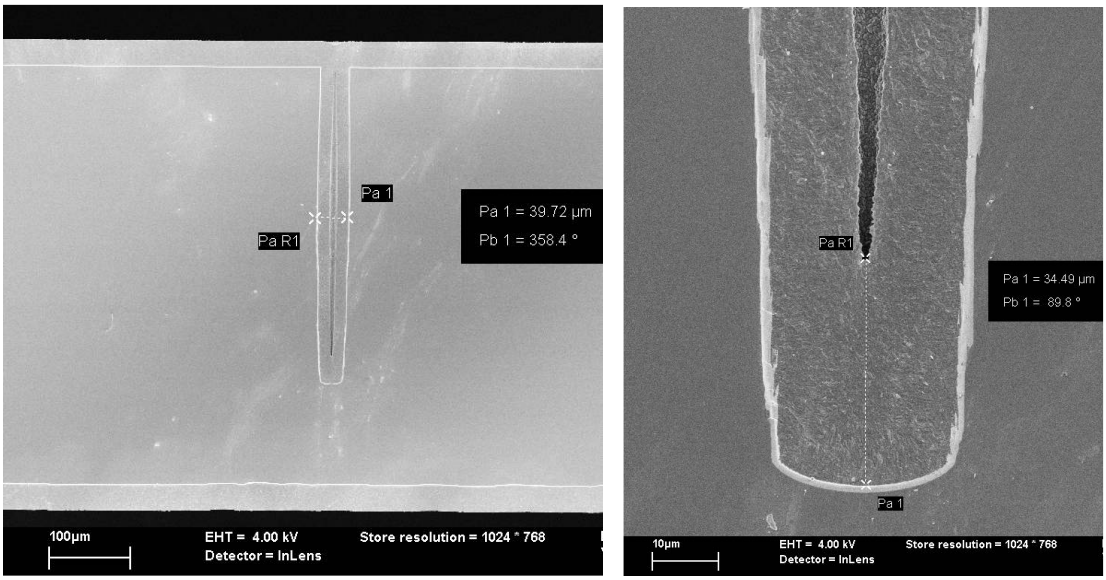

(a) (b)

Figure 36. SEM pictures of an etched hole of 380 μm depth, oxidized with 2 μm thick thermal SiO_2 and filled by deposition of a 30 μm thick polycrystalline silicon. The etched hole has a convex shape with diameters of 40 μm midway, 36 μm at the top and 29 μm at the bottom. (a) Shows the filled hole with a void in the centre of the hole. (b) Shows a detailed picture of the bottom of the hole and void.

Fig. 36 shows scanning electron microscope (SEM) photographs of cross-sections of a fabricated electrode after hole filling with a polycrystalline silicon. In Fig. 36(a), the depth of the electrode is 380 μm and the diameter midway in the hole is 40 μm, thus the depth-to-diameter aspect ratio is about 10:1. The polycrystalline silicon is unable to fill the hole uniformly and a void is left inside the electrode. Fig 36(b) shows a void in detail. The LPCVD method favors polycrystalline formation at the bottom and top, because the etched holes have slightly a larger diameter midway in the hole than at the bottom or top.

Chapter 9

3D detector characterization by using simulation

Device models of semiconductors based on numerical solutions of differential equations were started by H. K. Gummel in 1964 on 1-dimensional steady state analysis of bipolar transistors [70]. In 1969, 2D models appeared with the analysis of a junction field-effect transistor [71]. Also bipolar transistors were simulated in 1D and 2D [72]. It took more than a decade before one of the first 3D models was published in 1981. This model used finite element analysis in 3D to study the basic characteristics of semiconductor devices [73].

Until recently, it was considered sufficiently accurate to simulate planar radiation detector structures with 2D device simulators, since the third dimension was of secondary importance in detector performance. After introduction of 3D detector structures and their fabrication process, inclusion of the third dimension in simulations has become very important in understanding the performance of the devices.

9.1 Simulation method

Publications II and III contain physical simulations done by ISE-TCAD [74], a commercial 2D/3D TCAD simulation software. The software is based on a finite element method (FEM), where the calculation volume and partial differential equations (PDE) are discretized and the numerical calculations are performed element-wise. The discretization procedure converts the original continuous model to a discrete non-linear algebraic system that has approximately the same behavior. The non-linear algebraic system is solved using an iterative procedure that refines successive estimates of the solution. Physical boundary conditions of the calculation volume give initial values for the iteration procedure. The iteration continues until the corrections are small enough to satisfy the convergence criteria and then the solutions are assigned for the discretized nodes.

9.1.1 Basic semiconductor equations

The equations that describe the current flow in a semiconductor and determine the electrical performance of the device are Poisson's equation and the continuity equations for electrons and holes. Poisson's equation is given by

$$\epsilon \nabla \Phi = -\rho = -e\left(p - n + N_{eff}\right), \tag{36}$$

which relates the total space charge ρ to the electrostatic potential Φ, and the continuity equations by

$$\frac{\partial n}{\partial t} = \frac{1}{e}\nabla \cdot \overline{J}_n + G_n - R_n, \tag{37}$$

$$\frac{\partial p}{\partial t} = \frac{1}{e}\nabla \cdot \overline{J}_p + G_p - R_p, \tag{38}$$

where n and p are the electron and hole densities, $\overline{J}_n$ and $\overline{J}_p$ are the electron and hole current densities, G_n and G_p are the generation rates for electrons and holes, and R_n and R_p are the recombination rates for electrons and holes, respectively [74]. The current densities are further writen out as

$$\overline{J}_n = e\mu_n n \overline{E}_{eff,n} + eD_n \nabla n, \tag{39}$$

$$\overline{J}_p = e\mu_p p \overline{E}_{eff,p} - eD_p \nabla p, \tag{40}$$

where $\overline{E}_{eff,n}$ and $\overline{E}_{eff,p}$ are the effective electric fields for electrons and holes, respectively. The discretization method of the above equations is explained in detail in Appendix B.

9.1.2 Boundary conditions

Two different boundary conditions were used in the simulations. The n^+ and p^+ ohmic contacts were treated with Dirichlet boundary conditions, which set the electrostatic potential to the applied bias, and assume charge neutrality and equilibrium at the electrodes. Along the remaining boundaries, ideal Neumann (reflective) boundary conditions were used

$$\begin{aligned} \overline{J_n} \cdot \overline{n} &= 0, \\ \overline{J_p} \cdot \overline{n} &= 0, \end{aligned} \tag{41}$$

where $\overline{J_n}$ and $\overline{J_p}$ are the current densities of electrons and holes, respectively, and $\overline{n}$ is a vector normal to the boundary. These conditions ensure that no current can flow in or out of the device through these edges [74].

9.1.3 Numerical solvers

After discretization, the PDEs are solved iteratively with a Newton method. A quasi-stationary simulation is used to ramp the bias voltage such that at each bias step the simulation is restarted after alternation of the parameter values and the boundary conditions. For charge collection characterization, the PDEs are first solved with the same procedure and are then integrated in the time domain. The software applies the trapezoidal

rule/backward-differentiation-formula (TRBDF) composite method, which uses only the solution at one previous time level [74]. The numerical solvers are explained in detail in Appendices C and D.

9.1.4 Physical models

The physical models used throughout the characterization were taken from the physical model library of ISE-TCAD, [74], and the following models were accounted for:

- **bandgap narrowing:** defines the effective intrinsic density in silicon;
- **doping dependent mobility:** defines the mobility of the charge carriers;
- **high field saturation:** defines the velocity of the charge carriers in a high electric field;
- **scattering:** includes charge carrier scattering with other carriers, surface phonons and surface impurities;
- **recombination process:** includes doping-dependent ShockleyHallRead (SHR) recombination, Auger recombination and surface recombination processes;
- **impact ionization:** defines the ionization rate of the charge carriers in a high electric field.

Charge collection characteristics were studied with a single event generation method, provided by ISE-TCAD, that introduces a minimum ionizing particle (MIP), which penetrates through the silicon wafer and creates about 80 electron–hole –pairs/μm uniformly along its path with a lateral spread of 5 μm, defined by a complementary error function.

9.2 Simulation of a full 3D detector

Publications II and III studied the characteristics of a so called rectangular 3D detector design, where in an n-type bulk, a p-type electrode is surrounded by eight n-type electrodes as shown in Fig. 37. The pixel structure was proposed in the original paper by S. Parker [60]. Only a quarter of a full pixel in Fig. 37 was electrically characterized by simulations in publication II. The 2D and 3D simulations done for the structure were found to give similar results and their discrepancies arose from different implementation of the doping profiles of the electrodes. It was shown that the electrical characteristics at full depletion can be well approximated theoretically. The leakage current and capacitance of the detector pixel, shown in Fig. 37, were calculated to be ~ 1 nA and ~ 80 fF, respectively. For comparison, a planar detector with similar dimensions has about the same leakage current but the capacitance is about 10 times smaller because the electrodes are spaced firther apart.

Publication III dealt with charge collection (CC) characterization of a pixel shown in Fig. 37. Charge sharing with the neighboring pixels was studied by introducing MIPs along the dashed line in 10 different locations. Throughout this thesis each MIP crossed the pixel structure perpendicular to the surface, as indicated with a bold arrow.

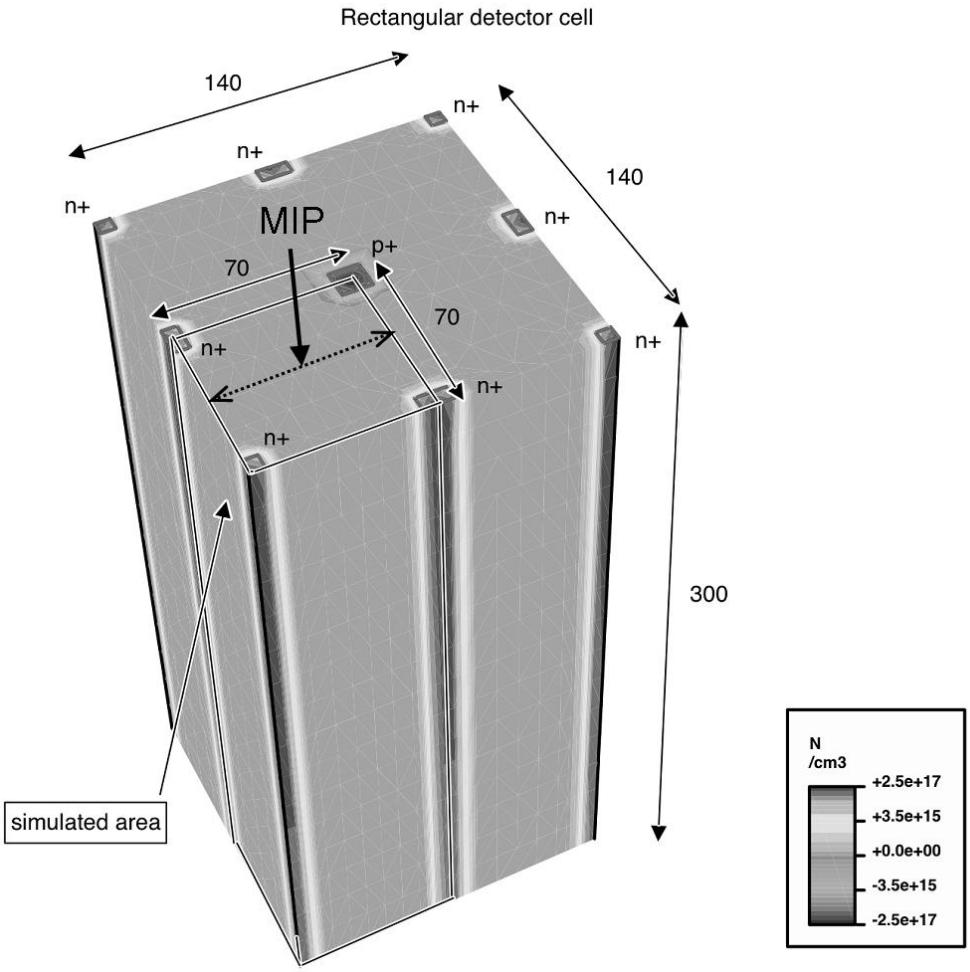

Figure 37. Depiction of total doping concentration of the 3D rectangular pixel structure. Dimensions of the pixel are given in microns (μm). The bold arrow shows the direction of the MIP and the dashed line, extending from inside to the outer edge of the pixel, the entrance locations for the charge-sharing examination. The exact entrance locations are shown on the X-axis in Fig. 38(a).

As depicted in Fig. 38(a) (dashed curves), the charge is shared only within a few microns from the pixel edge. Excluding the edge volume, the signal charges are collected by the venter p-type electrode with high efficiency and in less than 10 ns at 20 V. The time interval between recording the peak of the charge pulse and collecting 90% of the charge signal is due to spreading of the clouds of the charge carriers during the CC process.

The CC time of a 3D detector pixel was observed to depend on the resistance-capacitance (RC) product of the pixel and on the depth of the primary interaction by the incident particle. In publication III, it was shown that the RC product depends on the detector thickness, h, as: $t \sim h^2$. The dependence has been analyzed by simulating the CC time as a function of detector thickness as shown in Fig. 38(b). An ionizing radiation creates charge carriers (electron hole pairs) in the detector bulk. When moving towards the detector electrodes, the charge carriers induce a current flow into the electrodes. The opposite

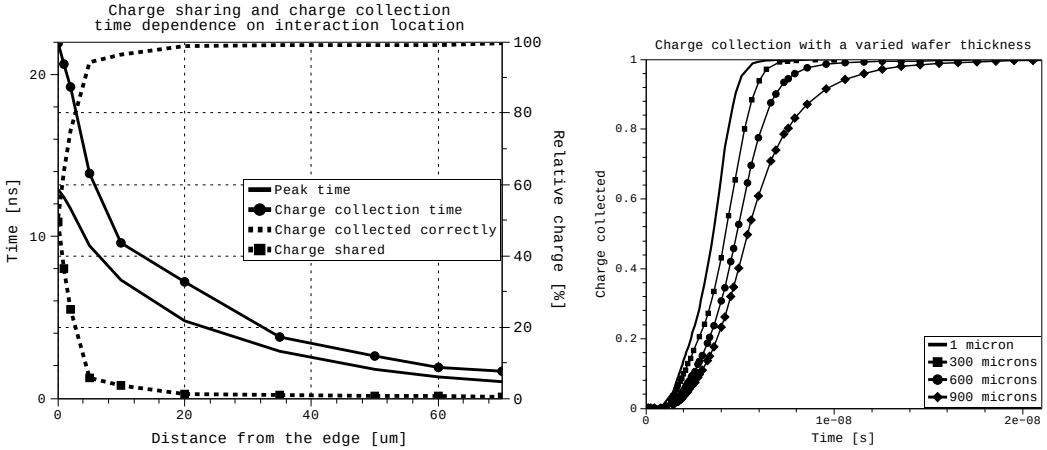

(a) (b)

Figure 38. (a) Dependence of CC time and charge sharing on the interaction location of the incident radiation. The X-axis shows the entrance locations of the MIP from the pixel edge in microns (μm); the peak time of the current response signal and the CC time are given on the left Y-axis and the charge collected correctly by the pixel and the charge shared by the neighboring pixels are given on the right Y-axis in percentages (%). (b) Charge collection with detector thicknesses of 1, 300, 600 and 900 μm.

sign electric charge is drawn from the circuit through contacts until the full depth of the interaction is reached, *i.e.* the current flows into the electrodes up the interaction distance. Movement of charge within the electrodes causes a serial resistance, created by the detector structure, to depend on the interaction depth. The phenomenon is illustrated in Fig. 39(a), where the current is seen to be drawn deeper into the bulk for the deep interactions (MIPs entering the detector from the bottom side). A higher serial resistance is created in this case and, therefore, a delay in CC follows as seen in Fig. 39(b). For the 3D detectors manufactured with very high depth-to-diameter aspect ratios, the delay phenomenon in the CC time has to be accounted for.

The LHC and its upgrade SLHC require features of 3D detectors due to their increasing requirements in radiation hardness, charge collection resolution and speed. Combining the results from publications II and III, the rectangular 3D detector design was proven to be well suited for particle tracking in a hostile radiation environment: a suitable geometry for low charge sharing; high charge collection efficiency that provides large signals with low noise; and a high charge collection speed due to the short electrode spacing that lowers the trapping probability of the charge carriers and increases the radiation tolerance of the detector.

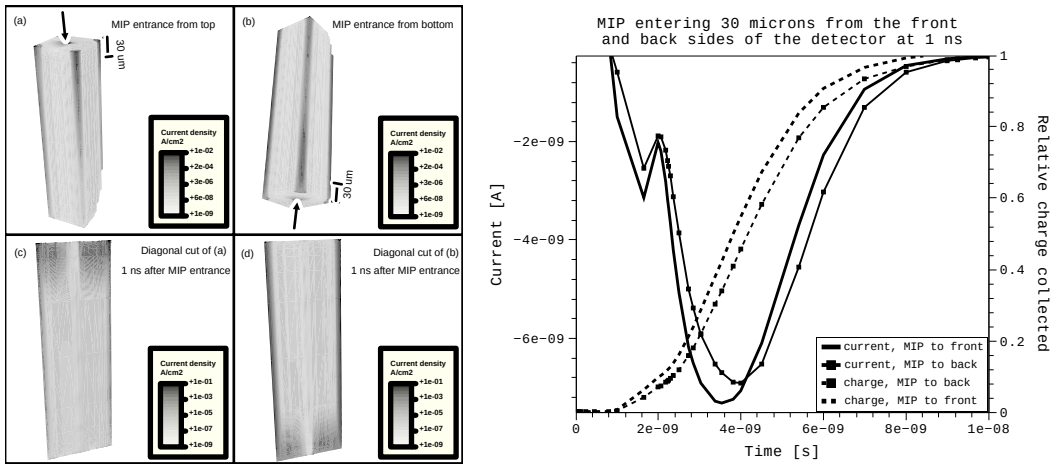

(a) (b)

Figure 39. Demonstration of CC time dependence on the interaction depth of the incident ionizing radiation. An MIP hitting the center of the quarter pixel from the top and bottom and penetrating 30 μm. (a) Induced current densities at the entrance of the MIP (top) and 1 ns later (bottom). The bottom figures are diagonal cross-sectional cuts of the quarter pixel. (b) Induced current response pulses and their integrals, *i.e.* charge collection curves.

Chapter 10

Semi-3D detector characterization

This chapter describes the characterization methods of fabricated semi-3D detectors and summarizes the results of publications IV-VI.

10.1 Electrical characterization of a semi-3D detector

The electrical characterization, current-voltage (IV) and capacitance-voltage (CV), of the semi-3D test structure presented in the previous chapter in Fig. 27(a) were done at VTT. The results of publication IV are preliminary because the measurements were done in a covered probe station by biasing the bottom of the wafer and measuring the current or capacitance from a strip. The neighboring strips were unbiased and floating, which allows them to set to a voltage determined by the applied bias via the punch-through method. The capacitance was measured using a small signal analysis, where a small test signal with a high frequency is inserted into the detector and the response is measured with an oscilloscope. In publications IV and V, the capacitances were measured from the 100 pixel strips using a 10 kHz and 1 MHz probe signals with the amplitude of 50 mV, respectively.

In publication V, the measurements where done in a laboratory at the university of Helsinki. This time also the strips neighboring the measured one where grounded. In this way the neighborhood of the measured strip is stabilized and the neighboring grounded strips collect most of the surface current. The stabilized neighborhood of the center strip also allows direct comparison of measurements with simulations.

In the simulations presented in publication V, the purity of the fabricated silicon wafers was taken into account by a long charge carrier lifetime, $\tau_{n,p} = 10^{-2}$ s, and by a fixed surface charge of 10^{11} cm^{-2} in the oxide–silicon interface. The results show good agreement with the measurements for the capacitance and leakage current of a single semi-3D pixel, as shown in Figs. 40(a) and 40(b), respectively.

In Fig. 40, the essential point is that the pixel obtains the full depletion (saturation of the capacitance) at about 30 V with a measured value of 3 fF/pixel and with a leakage current of $\sim$ 0.3 pA. Both of these measured values are comparable to those reported for a similar structure that has been fabricated on a p-type bulk with n-type column electrodes. Moreover, the measured capacitances and leakage currents are roughly one

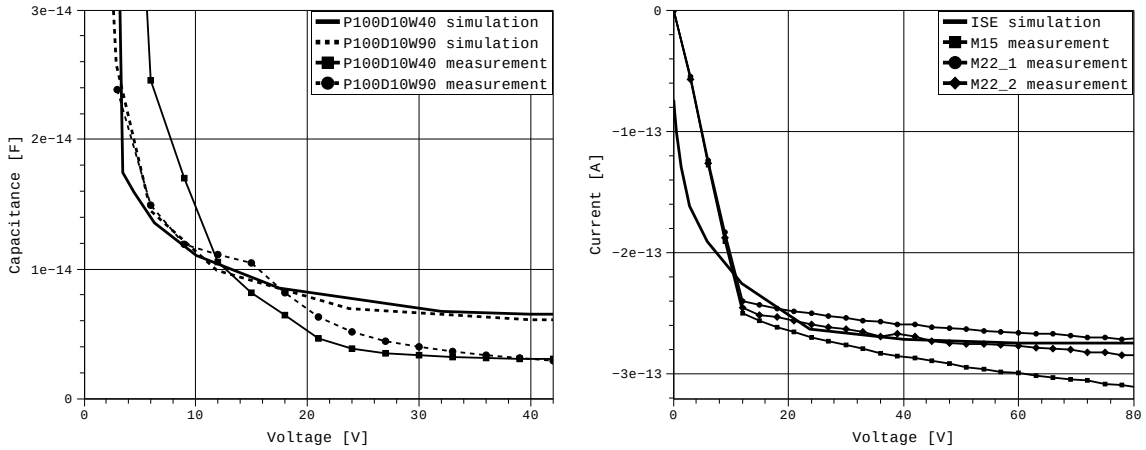

(a) (b)

Figure 40. (a) Simulated and measured capacitances per pixel for implant sizes of 40 and 90 μm with a pixel pitch of 100 mm and an electrode diameter of 10 μm. (b) Simulated and measured leakage currents per pixel of a 100 μm pitch structure with an electrode diameter of 10 μm and a surface implant width of 90 μm.

order of magnitude smaller in publication V than in IV due to corrected measurement setup.

Fig. 41 shows the influence of the surface implant design on the leakage current in the structure with a pixel pitch of 100 μm and pillar diameter of 10 μm. The experimental results on strips with 100 pixels on an FZ and CZ wafers are displayed. The leakage currents in the FZ devices in Fig. 41(a) with the wide surface implant (90 μm) show nice saturation, whereas the devices with the narrow surface implant (40 μm) exhibit a nearly linear current growth. The difference is due to the different influence of the currents generated near the oxide–silicon interface. The striking difference in the CZ current compared to the FZ currents is the clear breakdown around 70 V as shown in Fig. 41(b). Moreover, the current values are larger and the influence of the surface implant is not clearly seen.

Fig. 42 shows the leakage currents for a pixel pitch of 200 μm with varied pillar diameters and implant sizes. The current curves for the diameter size of 10 μm behave similarly as for the 100 μm pitch. Surprisingly, for the diameter of 20 μm, the currents are larger even though the depletion volume is smaller. This can be interpreted to be caused by a high electric field and current generation at the end of the electrodes, which in this case are only 100 μm away from the back plane. Still, for the small implant width (100 μm) the currents increase linearly after full depletion and saturate for the large ones (190 μm).

10.2 Radiation hardness

The irradiation was performed for publication IV with 24 GeV high-energy protons at fluences of 1.4×10^{15}, 4.0×10^{15}, 6.0×10^{15} and 1.0×10^{16} cm^{-2} at the CERN Irrad1 facility operating with a PS accelerator [75]. During irradiation the samples were not cooled or biased. Each sample had an area of 1 cm^2 with a pitch of 100 μm, surface implant

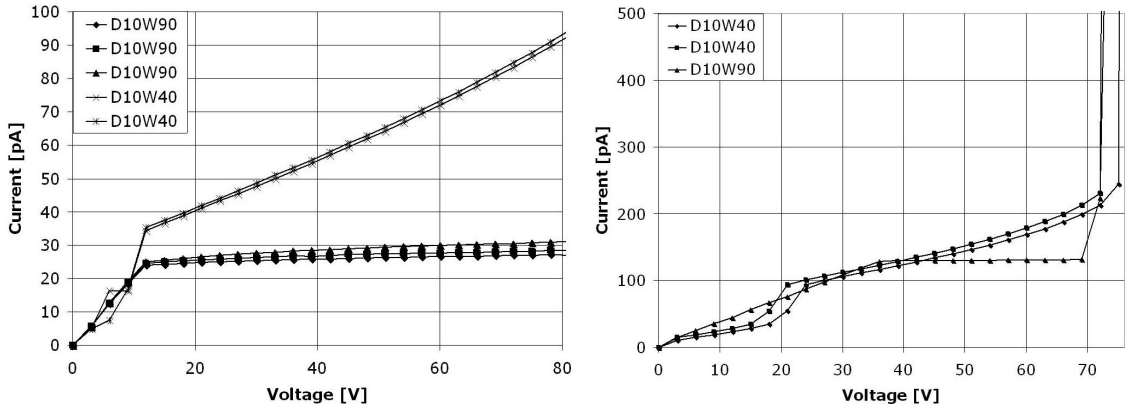

(a) (b)

Figure 41. (a) Measured leakage currents of structures of 100 pixels with pitch 100 μm and diameter 10 μm. Influence of surface implant width on leakage currents. (b) Similar leakage currents of structures fabricated on CZ silicon to those presented in (a).

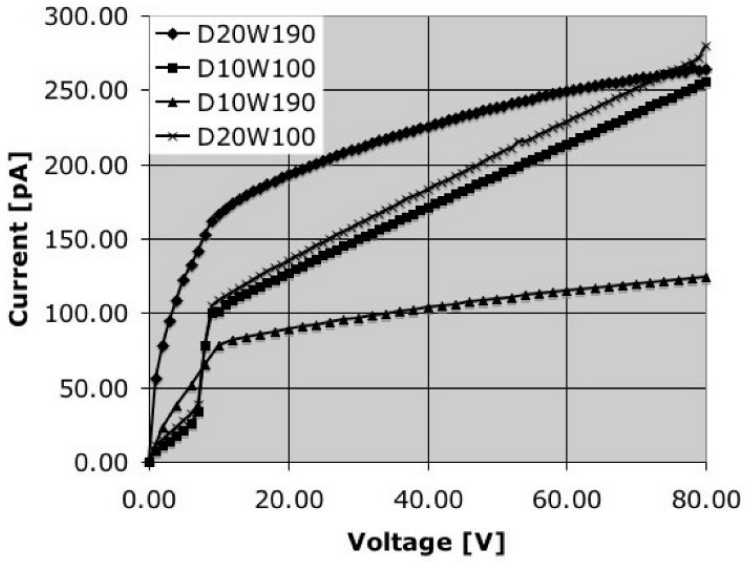

Figure 42. Measured leakage currents for a pixel pitch of 200 μm with pillar diameters of 10 μm and 20 μm and implant widths of 100 μm and 190 μm.

width of 40 μm, and hole diameter of 10 μm. After irradiation, the samples were stored at temperature below -10°C and annealed at 80°C for 4 minutes before measurements. The measured values are obtained from a single strip with 100 pixels. The values of full depletion, shown in Fig. 43(a), were determined from CV measurements performed at 10 kHz and at room temperature. No reliable data was obtained after irradiation with a fluence of 1.0×10^{16} cm^{-2}.

Fig. 43(a) shows the full depletion voltage of irradiated FZ and CZ semi-3D detectors as a function of 1 MeV equivalent neutron fluence. The fluencies were obtained for 24 GeV

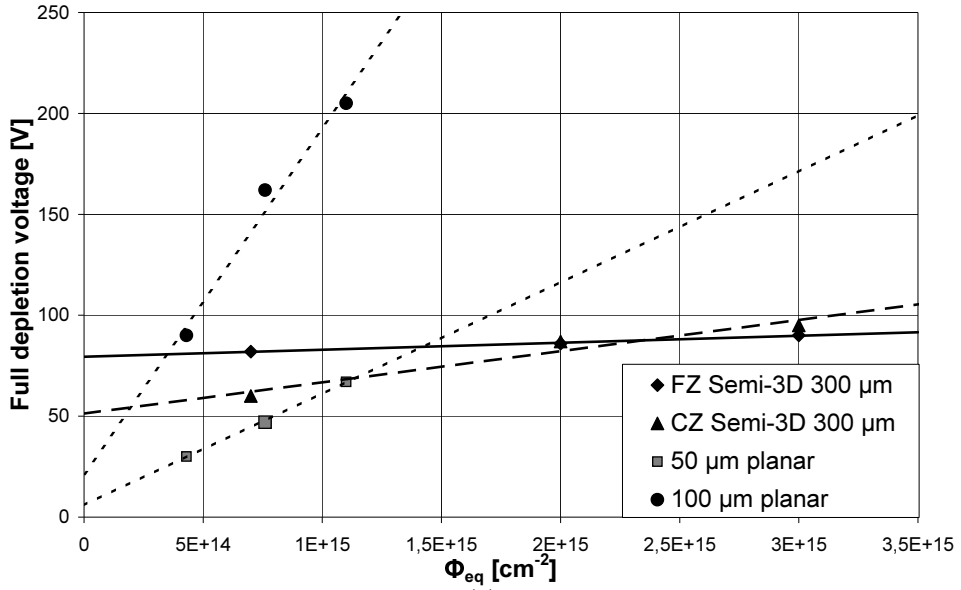

(a)

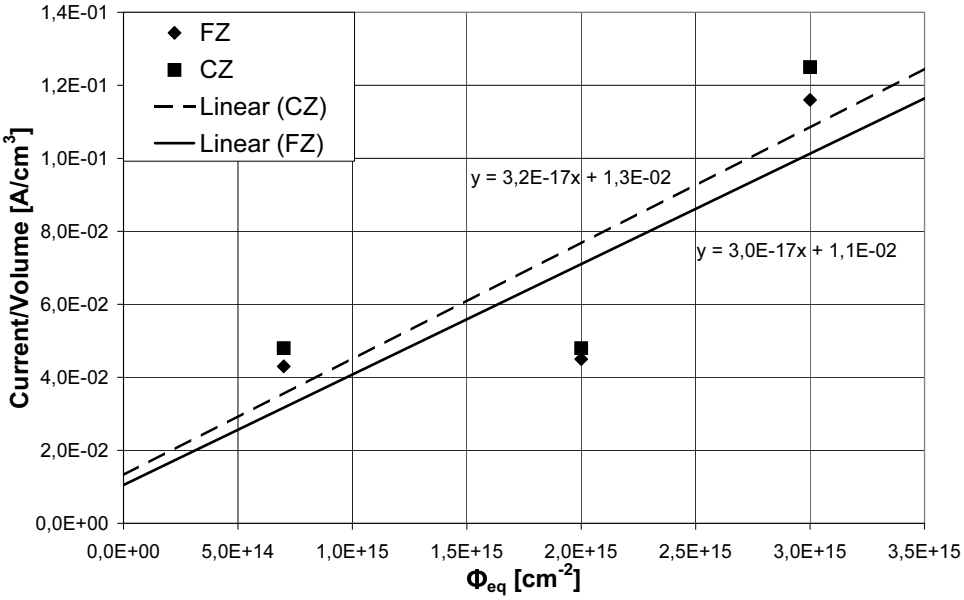

(b)

Figure 43. (a) Depletion voltage as a function of neutron equivalent fluence of measured semi-3D detectors fabricated on FZ and CZ silicon. For comparison, similar measurements of 50 μm and 100 μm planar detectors are included [57]. (b) Volume scaled leakage current as a function of neutron equivalent fluence of measured semi-3D detectors fabricated on FZ and CZ silicon. Linear fits have been included in the data to extract the damage factor of semi-3D detectors.

protons from Fig. 22(a) by scaling with 0.5. Depletion voltages for irradiated 50 μm and 100 μm thick pad detectors from Fig. 23(b) are illustrated for comparison. The NIEL scaling hypothesis suggests that a scale factor of ~ 27 may be used to relate a fluence value obtained with 27 MeV protons to a fluence value obtained with 58 MeV lithium ions [76]. The damage scaling factor of 27 MeV protons to 1 MeV neutrons from Fig. 22(a) is about 2.5. Thus the fluencies in Fig. 23(b) are multiplied by $27/2.5 \approx 10.8$ and the corresponding depletion voltages are plotted in Fig. 43(a). For semi-3D detectors the depletion voltages remain below 100 V even after very high irradiation of 6.0×10^{15} protons/cm^2 and there is no essential difference between the FZ and CZ materials. No correlation with the pad detectors is seen.

Fig. 43(b) shows the leakage currents measured from a strip after irradiation at full depletion. The current values are scaled with a presumed depletion volume, the quantification of which is not an easy task due to the measurement setup and presumed type-inversion of the n-type bulk. It is assumed that depletion began from the back plane side and the punch-through has occurred to the neighboring strips, which are set close to the potential at the backplane. In this case, the volume around the measured strip is depleted and the depletion region does not extend beyond the neighboring strips. The measured currents in publication IV are divided by the approximated depletion volume of a strip surrounding, *i.e.* 0.0006 cm^3 (strip length 100 μm, detector thickness 300 μm and twice a pitch of 100 μm). Equations of the linear fits to the current data are displayed and by using Eq. 34 the damage factor α of $\sim 3 \times 10^{-17}$ A/cm can be extracted. Even though the measured data does not correlate well with the linear fit, the damage factor is strongly compatible with a value of $\alpha \sim 4 \times 10^{-17}$ A/cm obtained from Fig. 23(a).

The preliminary irradiation study shows that the semi-3D detector design fabricated on FZ or CZ silicon is a good candidate for LHC and SLHC for its radiation hardness in terms of low depletion voltage and at high fluencies. Keeping in mind that the charge carriers' mean free path saturates at SLHC fluences to $\sim 30\,\mu$m and can no longer be affected by increasing the electric field, the proposed semi-3D geometry makes possible short charge collection distances. More measurement statistics are needed for making further conclusions concerning the radiation damage issue.

10.3 Imaging and tracking properties

Tracking and imaging properties of the fabricated semi-3D strip and pixel detector structures were characterized in publications IV-VI. Important characteristics such as X-ray response, energy resolution, charge collection speed and efficiency, charge sharing and spatial resolution were considered. Also direct comparisons were made between the planar and semi-3D pixel detectors.

10.3.1 Semi-3D strip detector

The first ever high X-ray or low γ-ray response of a semi-3D structure was tested with a ^{241}Am source in a laboratory at the Helsinki Institute of Physics (HIP) and was presented in publication IV. The tested detector had a strip structure, as shown in Fig. 27(a), on FZ silicon with an effective area of 4 cm^2 (pixel pitch of 200 μm), surface implant width of

100 μm and hole diameter of 20 μm (electrode depth of 200 μm). A number of neighboring strips to the measured one at the center of the detector were grounded, while the measured strip was connected to the amplifier. The irradiation was performed from the front of the detector at a bias of 24 V and the result is shown in Fig. 44.

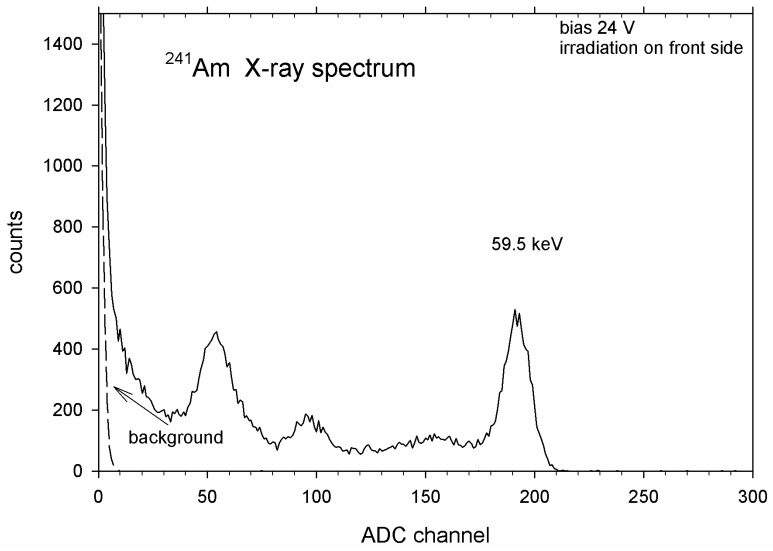

Figure 44. Measured ^{241}Am energy spectrum from a semi-3D detector strip of 100 pixels with a pixel pitch of 200 μm, pillar diameter of 20 μm and implant width of 100 μm.

The full width at half maximum (FWHM) of the energy peak of ^{241}Am at 59.54 KeV was measured to be $\sim$ 4.6 keV (7.7%). As mentioned in publication IV, the full depletion of a semi-3D structure with a pixel pitch of 200 μm is not seen below 34 V and is expected to be around 40 V. Thus the test sample was under-depleted at 24 V bias during irradiation, and the resulting energy spectrum in Fig. 44 is not optimal.

Charge collection

Analysis of the charge collection speed of the semi-3D structure was performed with the methods described in the previous chapter. Now a particle hits the center point of four pixels with the pixel pitch of 100 μm, hole diameter of 10 μm and surface implant widths of 40 μm and 90 μm. Fig. 45(b) illustrates the integrated response currents from a pixel, *i.e.* the charge generated by the penetrating particle. The hit point at the center of the four pixels represents the worst-case scenario for the semi 3D structure, because the electric field is weakest in this region. According to the simulations presented in Fig. 45(c), most of the charge is collected independently on the detector geometry within $\sim$ 20 ns (the leading edge), and beyond this point a slow tail of electron collection from the backplane is observed. Only the charge generated in the weak electric field regions can be lost via the recombination process. The volume of the weak electric field region can be tuned by the surface implant width, as presented in Fig. 45(b), or by the pitch and depth of the p-type electrodes. A more detailed simulation of the charge collection properties of a semi-3D structure can be found in [77].

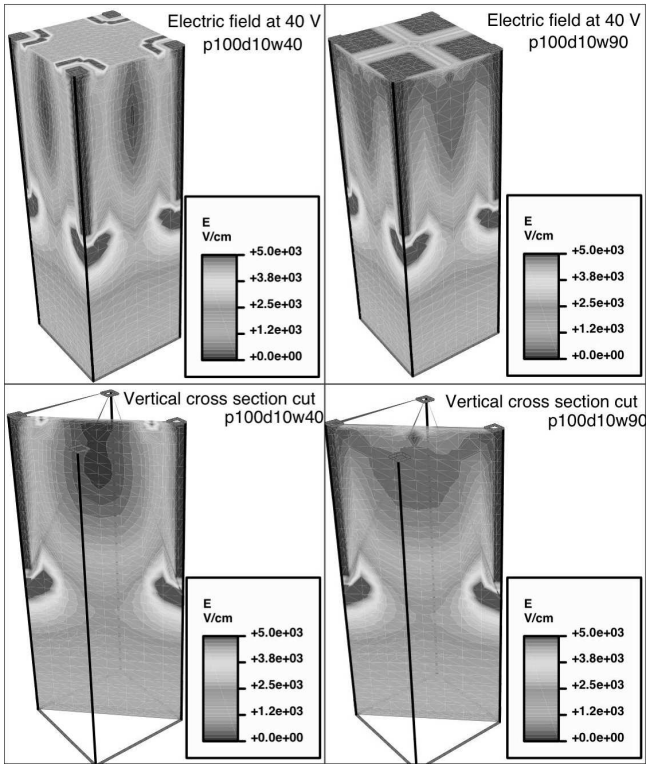

(a)

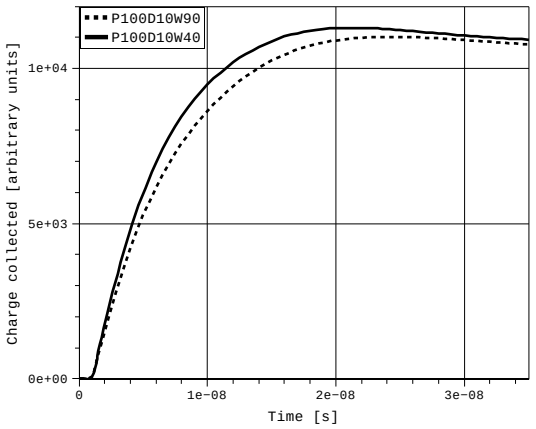

(b)

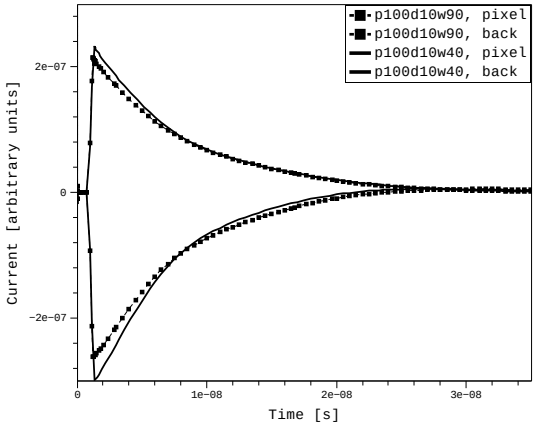

(c)

Figure 45. (a) Simulated electric fields in an intermediate region of pixels in a semi-3D device with different implant widths at 40 V bias. A pixel pitch of 100 μm, pillar diameter of 10 μm and implant widths of 40 and 90 μm are presented. (b) Charge collection of an MIP from the middle of the grounded p-type pillars of the semi 3D detector cells. The fast leading edge of the charge collection is shown. (c) Current response pulses from the pixel and backplane in similar events as in (b).

The charge collection efficiency (CCE) of a semi-3D structure, tested previously in [78] with a ^{90}Sr β-particle source, is shown to be effectively collected from the bulk at low bias voltage. Moreover, it is suggested that at a zero bias voltage the CCE value is roughly proportional to the ratio between the column depth and the substrate thickness of the semi-3D detector.

The semi-3D concept can be promising in applications not requiring charge information within a short time. Observation of a clear leading edge is important in tracking devices that require a fast signal response but not the energy information of the observed particle. A drawback of 3D-stc structures is that, once full depletion is reached, it is not possible to increase the electric field strength in the active region by means of the bias voltage, so that the response time can be degraded.

10.3.2 Semi-3D pixel detector

A semi-3D pixel detector, shown in Fig. 27(b), fabricated on high resistive n-type FZ silicon has been characterized in detail with respect to the imaging capabilities of the proposed design. In publication VI, a reference planar pixel detector and the semi-3D pixel detector are bump-bonded to a Medipix2 readout chip that presents a large number of identical pixels and is an excellent test vehicle for characterizing pixel architectures in imaging.

Medipix2

The Medipix2 chip is a pixel-detector readout chip consisting of 256×256 identical elements, each working in single photon counting mode for positive or negative input charge signals [66]. Each pixel cell contains around 500 transistors and occupies a total surface area of 55 μm $\times$ 55 μm. The total chip covers an area of 1.98 cm^2. A 20 μm wide octagonal opening connects the detector and the preamplifier input via bump bonding. An illustration of the connection scheme by bump-bonding to the Medipix2 and a typical back-illuminated irradiation setup is shown in Fig. 46(a).

The preamplifier feedback provides compensation for detector leakage current on a pixel by pixel basis. The analog and digital parts of the medipix2 circuit of a pixel are drawn in Fig. 46(b). Two identical pulse height discriminators are used to create a pulse if the preamplifier output falls within a defined energy window. These digital pulses are then counted with a 13-bit pseudorandom counter. The counter logic, based in a shift register, also behaves as the input-output register for the pixel. Each cell also has an 8-bit configuration register which allows masking, test-enabling and 3-bit individual threshold adjustment for each discriminator. The chip can be configured in serial mode and read out either serially or in parallel. Using a clock of 100 MHz the entire matrix is readout in less than 9 ms through the serial port, whereas with the parallel option the readout is done in 266 μs. The chip is designed and manufactured with 6-metal 0.25 μm CMOS technology. The detection threshold can be linearly adjusted from $\sim$ 3 keV up to $\sim$ 100 keV. The measured threshold dispersion over the matrix is less than 100 e$^-$ root mean squared (rms), and the equivalent-noise-charge (ENC) of a pixel of 140 e$^-$ rms. For the measurements presented here the chip has been used in single threshold mode only.

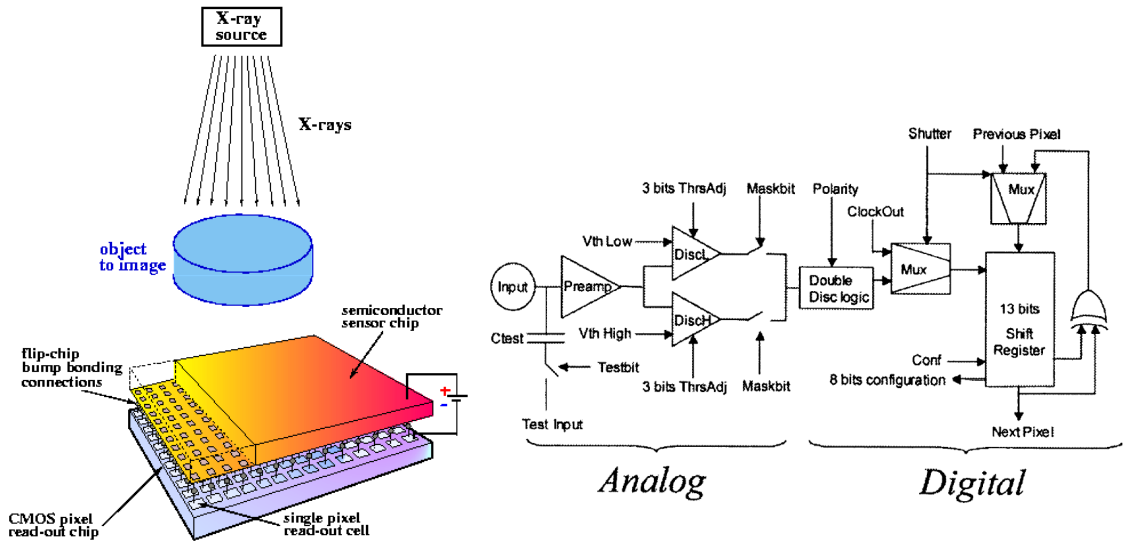

(a) (b)

Figure 46. (a) Illustration of how the Medipix2 readout chip is connected to the detector and how the measurements are performed. (b) Schematic of a circuit in each Medipix2 pixel.

10.3.3 Results

The measurements were done at the CERN irradiation laboratory with X-ray sources of ^{55}Fe, ^{90}Sr and ^{109}Cd, a pulsed 1060 nm laser beam and W-target X-ray tube. The first two were used to validate the quality of the bump-bonding process by investigating the responses at each pixel. The results revealed almost perfect bonding of both planar and semi-3D detectors with a yield of $\sim 99.9\%$.

The ^{109}Cd source was used in a two-fold manner to estimate the depletion voltage and define the energy resolution of the detectors. The full depletion condition was determined by counting a mean number of photons observed at different bias voltages. Fig. 47 shows the IV-curves and mean photon counts obtained with a semi-3D detector and the respective standard planar detector. The measured currents include all contributions from the guard rings and have the same order of magnitude. The depletion voltage of ~ 5 V obtained with the semi-3D detector is consistent with a depletion voltage of a 100 μm planar sensor that is obvious when inspecting the simulation results shown in Fig. 49. The full depletion of the planar detector is reached approximately at 20 V, which is a four-times larger bias.

The energy spectrum and resolution were defined from K lines of ^{109}Cd at 22 keV and 25 keV at 40 V bias by scanning the energy threshold of a digital-analog converter (DAC) and marking the mean number of counts in an acquisition time of 1000 s. Fig. 48 shows the scan results of the semi-3D and planar detector in an energy range from 10 keV to 30 keV. The energy resolution of ~ 1.6 keV (7.4%) FHWM at 22 keV was found for the semi-3D detector without a clear sign of the 25 keV line, which was barely seen in the case of the planar reference detector with FHWM of ~ 1.5 keV (6.8%). The absence of the 25 keV signal could indicate that part of the charge is being lost in the semi-3D structure due to incomplete charge collection from the pillar electrodes and the intermediate undepleted

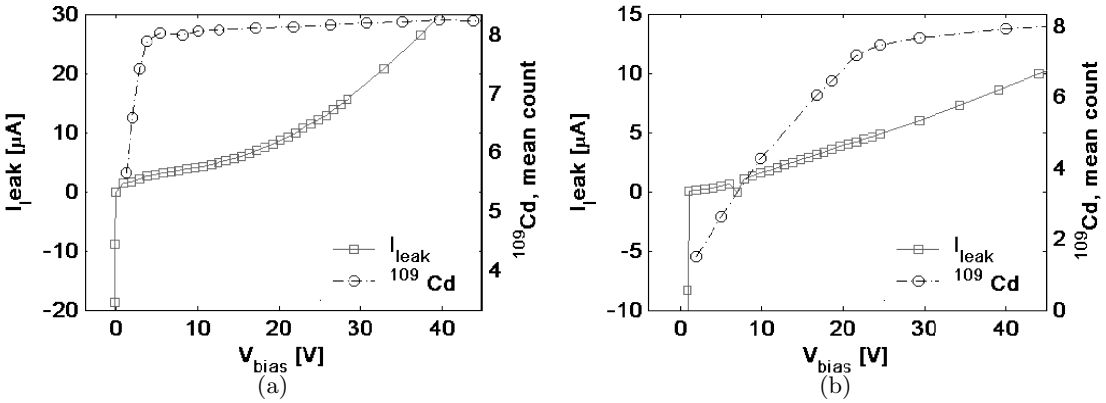

Figure 47. IV curves and depletion voltage measurements using a ^{109}Cd source and an acquisition time of 100 s. (a) Semi-3D pixel detector and (b) planar pixel detector.

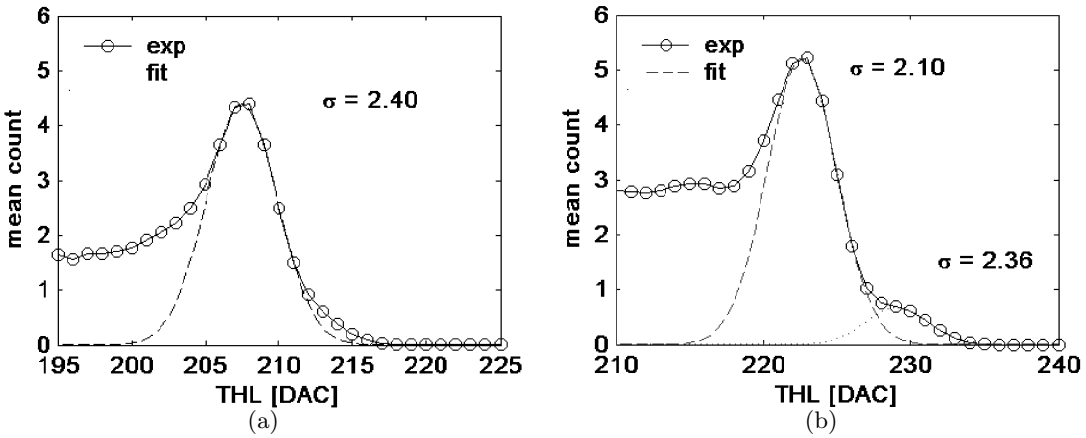

Figure 48. Energy resolution of (a) the semi-3D detector and (b) the planar detector using a ^{109}Cd source.

region between them, as shown in publication VI. The number of mean counts from the planar detector is almost double that obtained from the semi-3D one at energies below the 22 keV peak, as shown in Figs. 48(b) and 48(a), respectively. In addition, the peak height-to-valley ratios are approximately 1.9 and 2.6 in favor of the semi-3D detector. This advantage is assumed to be caused by greater charge sharing in the planar detector. From the charge sharing perspective the 300 μm thick semi-3D detector could be equated with a 100 μm thick planar detector, because below the pillar electrodes the generated charge can be shared between many pixels and between the pillars it can only be shared with the closest ones. Nevertheless, an increase in the bias voltage should reduce the charge sharing in the planar detector but not in the case of the semi-3D detector, because the charge collection time is not significantly improved there.

Simple DC simulations were done to intensify the hypothesis that the intermediate region between the doping pillars is undepleted, which could explain the experimental results mentioned above. Prior to the simulations, the surface charge of $\sim 3 \times 10^{11}$ cm^{-2} was measured at VTT and it was used as an input parameter for the simulations.

Fig. 49 shows the results of an intermediate volume of four p-type doping pillars at 40 V. Even at this bias the depletion region does not penetrate into the volume between the p-type pillars due to the fine pixel pitch and great depth of the grounded p-type pillars. The intermediate volume is not fully depleted and the charge collection process there is deteriorated.

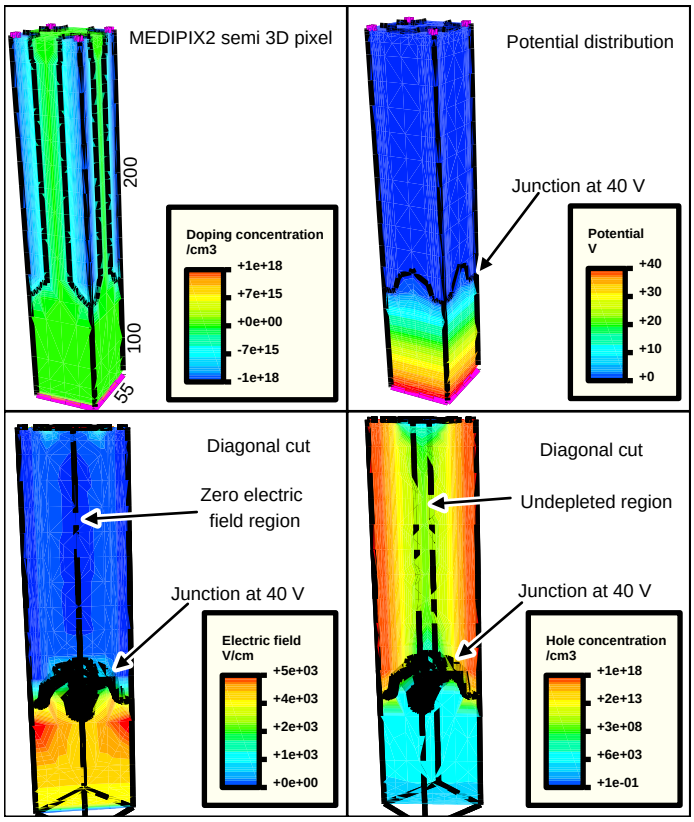

Figure 49. Simulation results of the fabricated semi-3D structure. The black solid line indicates the pn-junction. The figures show the total doping concentration that was used as input to the simulation (up left), the potential (up right), electric field (down left) and hole concentration (down right) distributions at 40 V bias. The lower figures are diagonal cross sections through the center of the intermediate volume of the four doping pillars.

To demonstrate the imaging capabilities of the semi-3D device a slit mask image was taken using a W-target X-ray tube, a filter of 2.5 μm Al and a W-target X-ray tube voltage of 35 kV. The first ever X-ray image taken with a 3D detector is shown in Fig. 50. The demonstration finds the semi-3D design in connection with the Medipix2 well suited also to X-ray imaging. Each line and gap in the image labeled "50" has a width of 100 μm in the Al filter, since the spatial resolution in this case is found to be far better than 100 μm.

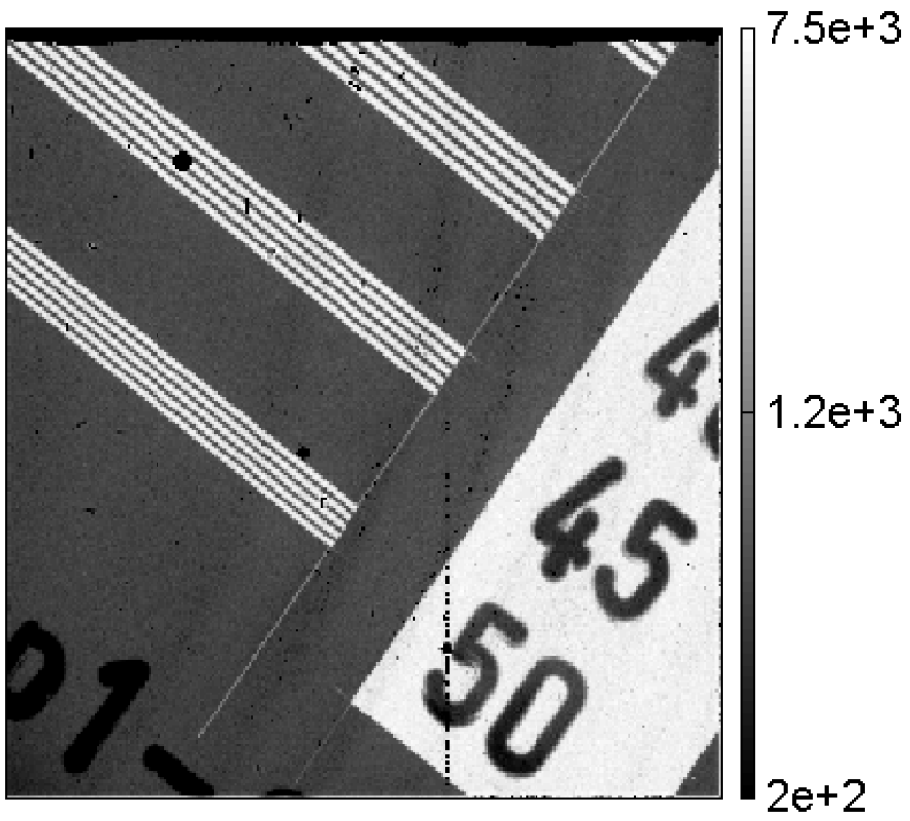

Figure 50. Image of a slit mask taken with the semi-3D detector and a W-target X-ray tube at 35 kV and a filter of 2.5 μm of Al. The number of line-pairs per cm are indicated on the right hand side of the image.

Chapter 11

Conclusions

This thesis describes a possible Higgs boson discovery process and a way to carry out the experimental analysis based on a novel type of a precision detector. For the LHC proton-proton collider, the search for the Higgs boson is top priority. On the other hand, the novel 3D silicon detector solutions developed here for measuring the leading protons in Central Exclusive Diffraction, $p + p \rightarrow p + X + p$, will have a wide range of application beyond fundamental high-energy physics research.

The thesis has introduced a method for reconstructing the mass of a centrally produced system in the central exclusive diffraction process by measuring the momentum of the scattered "leading" protons. A first systematic analysis of the accuracy of the method was carried out and a mass resolution of around 1 GeV/c^2 was obtained for masses beyond $\sim$ 120 GeV/c^2. For the light 120 GeV/c^2 Standard Model Higgs boson produced in the central exclusive diffraction and measured with the mass acceptance window of 1 GeV/c^2, a prediction of a cross-section gave $\sim$ 3 fb with a signal-to-background ratio of $\sim$ 1. In the analysis, the critical terms for the mass resolution were found to be the spatial resolution of the forward detectors, of around 10 μm, the minimized dead space at the detector edge, and the uncertainty in the transverse interaction positions of the colliding protons.

A hard radiation environment requires the tacking detectors to tolerate continuous irradiation during the physics runs. The radiation hardness of a detector has been shown to improve when the charge collection distance in the detector decreases. This work has proposed a novel radiation detector concept, a semi-3D detector, which is based on the idea of improving radiation tolerance, lowering the power consumption and charge sharing, and simplifying the full 3D fabrication process, while maintaining the spatial resolution and radiation attenuation depth similar to planar or full 3D detectors.

Successful fabrication of large scale semi-3D detectors up to $\sim$ 10 cm^2 has been demonstrated at VTT. These devices can be fabricated on a single wafer by only adding two process steps to a common planar process. The critical steps in a 3D detector fabrication were found to be etching and filling of the electrode holes and possible active edge. It has been shown that full 3D detector fabrication with the active edge on a single wafer, without any support on it, is not a straight forward or simple task.

Large scale strip and pixel semi-3D detectors fabricated on CZ- and FZ-silicon have been characterized to determine their electrical and charge collection properties. A comparison of similar structures made on FZ- and CZ-silicon showed that the leakage current is an order of magnitude larger in CZ-silicon, while the radiation hardness to 24 GeV/c protons remains alike with a radiation damage factor $\alpha \sim 3 \times 10^{-17}$ A/cm. The current measurements

of the CZ-silicon semi-3D strips detectors revealed repetitive avalanche breakdown around 70 V, which is about half the values measured for FZ-silicon. Furthermore, the smallest leakage currents and capacitances were measured for the structures with a large electrode implant area on the surface and with electrodes reaching midway in the bulk.

Simulations of 3D detector structures proved and complemented the expected properties of the 3D detector concept - fast charge collection, small charge sharing and low depletion voltage. It was shown that the charge collection process in 3D detector structures is delayed due to the peculiar geometry and induced RC constant, which depends on the interaction depth of the observed radiation. Moreover, the simulations were in agreement with the measured values of the semi-3D detectors and were able to illustrate how the depletion of the bulk is dependent on architecture of the electrode spacing and depth.

The tracking and imaging properties, such as X-ray response, energy resolution, charge collection speed and efficiency, charge sharing and spatial resolution of the fabricated semi-3D pixel detectors on FZ-silicon, were determined by connecting the detector to a Medipix2 readout chip. In addition, a direct comparison of the results with a 300 μm thick planar pixel detector showed that the depletion voltage ($\sim$ 5 V) of a 300 μm thick semi-3D detector with 200 μm deep electrodes is consistent with a depletion voltage of a 100 μm planar sensor and the full depletion of the planar detector is reached approximately with a four-times larger bias. The energy spectrum and resolution were defined from K-lines of ^{109}Cd at 22 keV and 25 keV at 40 V bias. The energy resolution at 22 keV for the semi-3D detector was found to be $\sim$ 1.6 keV (7.4%) FHWM and $\sim$ 1.5 keV (6.8%) FHWM for the planar reference detector. An inferior energy resolution and absence of the 25 keV line in the semi-3D detector spectrum is assumed to be caused by an incomplete charge collection from the electrodes and partly undepleted intermediate space in between. At 40 V bias the peak height-to-valley ratio was 37% in favor of the semi-3D detector. It is suspected that by optimizing the pixel pitch, electrode depth and implant area, the energy resolution could be improved. The irradiation measurements also strengthened the assumption that the charge sharing is diminished in semi-3D detectors compared with planar ones. The preliminary simulations indicated that the major part of the charge could be collected within 20 ns at a substantial bias of 40 V.

Finally, the imaging capabilities of a semi-3D device were demonstrated by taking a slit mask image with a W-target X-ray tube operating at 35 kV and a filter of 2.5 μm of Al. The first ever X-ray image taken with 3D detectors shows that the semi-3D design in connection with an advanced readout chip, Medipix2, is highly suitable for X-ray imaging. The spatial resolution of the image was shown to be far better than 100 μm (50 line-pairs/cm).

It is proposed that the semi-3D detectors fabricated for the TOTEM collaboration could be successfully tested within the next few months, and if the tests prove them to be functional, the second fabrication run for the experiment with the required modifications could be started in 2007 at VTT.

Appendix A

Rapidity and pseudorapidity

The coordinate system used is defined so that the z-axis is assumed to be parallel to the beam line. The x-axis is in the horizontal plane pointing out from the center of the accelerator, and the y-axis is in the vertical plane pointing upwards. The angle p_x in the horizontal plane is defined as

$$p_x = \frac{\Delta x}{\Delta z}. \tag{42}$$

The rapidity is defined in Eq. 43. The rapidity is invariant under a boost in the z-direction and thus a very useful property of the particle.

$$y = \frac{1}{2}\ln\left(\frac{E+p_z}{E-p_z}\right) = \ln\left(\frac{E+p_z}{m_T}\right) = \tanh^{-1}\left(\frac{p_z}{E}\right), \tag{43}$$

where E is the energy of the particle, p_z is the momentum component of the particle in the direction of it's movement, and m_T is the transverse mass defined in Eq. 44.

$$m_T^2 = m^2 + p_x^2 + p_y^2. \tag{44}$$

For $p \gg m$, the rapidity may be expanded to obtain

$$y = \frac{1}{2}\ln\frac{\cos^2(\frac{\theta}{2}) + \frac{m^2}{4p^2} + \dots}{\sin^2(\frac{\theta}{2}) + \frac{m^2}{4p^2} + \dots} \simeq -\ln\tan(\frac{\theta}{2}) \equiv \eta, \tag{45}$$

where θ is the angle between the particle momentum vector and the z-axis, thus $\cos\theta = \frac{p_z}{p}$. Concerning fast particles such as leading protons, the pseudorapidity η is approximately equal to the rapidity. The pseudorapidity is a measurable parameter from the scattering angle of the particle and actually this is how the rapidity is usually calculated.

Appendix B

Discretization

The "Box Integration Method" approximates differential operators on a general triangular grid and each PDE is integrated over a small polygon, a test volume that encloses each node. The set of all polygons completely covers the simulated area. The integration procedure equates fluxes into a polygon with sources and sinks inside the polygon, which means that quantities that are conserved physically are also conserved by the numerical solution [74].

After the integration of PDEs and application of Gauss' theorem, the resulting terms of PDEs are discretized to a first order approximation to give the following discretization:

Each PDE of form

$$\nabla \cdot \overline{J} + R = 0 \tag{46}$$

is discretized into

$$\sum_{j \neq i} \kappa_{ij} \cdot J_{ij} + \mu(\Omega_i) \cdot r_i = 0\,, \tag{47}$$

where κ_{ij} and $\mu(\Omega_i)$ are related to the size of the integration polygon given in Tab. 8. The physical parameters J_{ij} and r_i are defined in Tab. 9 [74].

Table 8. Size parameters of discretized PDE in Eq. (47)

Dimension	κ_{ij}	$\mu(\Omega_i)$
2D	d_{ij}/l_{ij}	Polygon area
3D	D_{ij}/l_{ij}	Polygon volume

In Tab. 8, l_{ij} is the distance between the grid points i and j and d_{ij} is the length of the edge of the polygon that is between the grid points i and j in 2-dimensions and D_{ij} is similarly the area of the face of the polygon that is between the grid points i and j in 3-dimensions.

An example of the integration polygon for a triangular mesh in 2-dimensions is shown in Fig. 51.

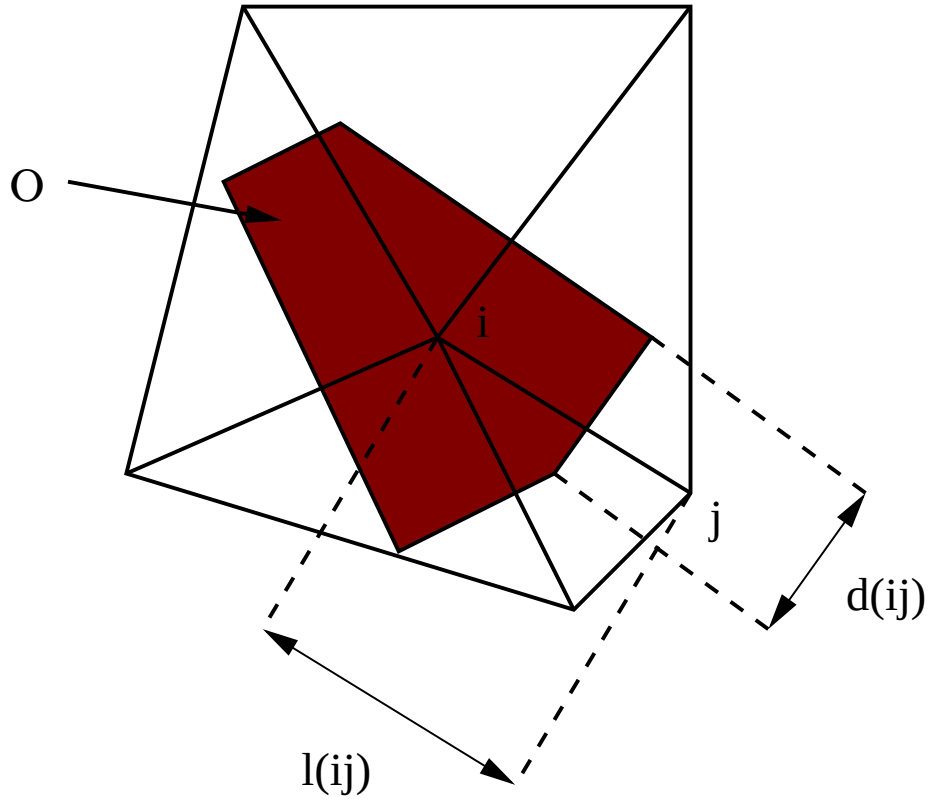

Figure 51. Example of the integration polygon for a triangular mesh in 2-dimensions. Here Ω, filled in red, is the area of the integration polygon of node i, $l(ij)$ is the distance between the grid points i and j, and $d(ij)$ is the length of the edge of the polygon between the grid points i and j.

Table 9. Physical parameters of discretized PDE in Eq. (47)

Equation	J_{ij}	r_i
Poisson	$\epsilon(u_i - u_j)$	$-\rho_i$
Electron continuity	$\mu_n \left[n_i B(u_i - u_j) - n_j B(u_j - u_i)\right]$	$R_i - G_i + \frac{d}{dt} n_i$
Hole continuity	$\mu_p \left[p_j B(u_j - u_i) - p_i B(u_i - u_j)\right]$	$R_i - G_i + \frac{d}{dt} p_i$

In Tab. 9, $B(x) = x/(e^x - 1)$ is the Bernoulli function, ϵ is the local permittivity, u_i and ρ_i are the potential and space charge density at the node i, μ is the mobility, R_i and G_i are the recombination and generation rates at the node i, and n_i and p_i are the electron and hole densities at the node i, respectively.

The actual assembly of the non-linear equations is done element-wise, thus Eq. (47) has an equivalent expression as

$$\sum_{E \in Elements(i)} \left[\left(\sum_{j \in vertices(E)} \kappa_{ij}^E \cdot J_{ij}^E \right) + \mu^E(\Omega_i) \cdot r_i^E \right] = 0\,, \tag{48}$$

where the sums are taken over the elements E of the node i and the vertices of the elements E. Eq. 48) are advantageous for numerical stability as well as for physical exactness, because parameters like ϵ, μ_n and μ_p can be handled element-wise [73].

Appendix C

Newton method

The non-linear algebraic systems that result from discretization are solved iteratively applying the scheme of Bank and Rose [79]. This scheme tries to solve the non-linear system $g(z) = 0$ by the Newton method with a suitable initial guess. The Newton method is given by

$$\begin{aligned} \overline{g}(z) + \overline{g}\,'(z)\overline{x} &= 0\,, \\ \overline{z}_j - \overline{z}_{j+1} &= \lambda\overline{x}\,, \end{aligned} \tag{49}$$

where λ is selected such that $||g(z_{k+1})|| < ||g(z_k)||$, but is as close to 1 as possible [79].

The Newton iteration stops if the convergence criteria are fulfilled. The iteration is handled by computation of an error function by two different methods. The first criterion is simply $||g(z_j)|| < \epsilon_A$. Another one is the relative error of the measured variables and it is given by

$$\left|\left|\frac{\lambda x}{z_j + z_{ref}}\right|\right| < \epsilon_R, \tag{50}$$

with

$$z_{ref} = \frac{z^*\epsilon_A}{\epsilon_R}, \tag{51}$$

where $z^* = n_i = 1.45 \times 10^{10}\,1/\mathrm{cm}^3$ for electron and hole continuity equations and $z^* = 25.8\,\mathrm{mV}$ for Poisson's equation [74].

Appendix D

Transient simulation

In transient simulations the carrier continuity equations are integrated in the time domain. The transient scheme assumes an implicit system of ordinary differential equations of the form

$$\frac{d}{dt}q(z(t)) + f(t, z(t)) = 0, \tag{52}$$

which in the case of continuity equations for electrons and holes has no explicit time dependence, though $f(t, z(t)) = f(z(t))$. In equations of this type, the trapezoidal rule/backward-differentiation-formula (TRBDF) composite method is applied [80]. The TRBDF method is one-step, second order, and both A-stable and L-stable. This means that the TRBDF method uses only the solution at one previous time level; the local truncation error (LTE) of TRBDF is proportional to the second power of the timestep; the errors introduced at one timestep will not increase at the next timestep, and the errors will decay even for large timestep values, respectively [80].

From each time point t_n, TRBDF does not move directly to the next time point $t_n + h_n$, but makes a step in between to time point $t_n + \gamma h_n$, which is advantageous in improving the accuracy of the method. Parameter h_n is the current timestep size and $\gamma = 2 - \sqrt{2} \approx 0.586$ has been shown to be the optimal value for the middle timestep [80].

The trapezoidal rule (TR) step is given by

$$2q(t_n + \gamma h_n) + \gamma h_n f(t_n + \gamma h_n) = 2q(t_n) - \gamma h_n f(t_n), \tag{53}$$

and the backward-differentiation formula (BDF) step by

$$(2 - \gamma)q(t_n + h_n) + (1 - \gamma)h_n f(t_n + h_n) = \frac{1}{\gamma}\left(q(t_n + \gamma h_n) - (1 - \gamma)^2 q(t_n)\right), \tag{54}$$

and the local truncation error (LTE) is estimated after a double step like

$$\Upsilon = C\left[\frac{f(t_n)}{\gamma} - \frac{f(t_n + \gamma h_n)}{\gamma(1 - \gamma)} + \frac{f(t_n + h_n)}{(1 - \gamma)}\right], \tag{55}$$

where

$$C = \frac{-3\gamma^2 + 4\gamma - 2}{12(2-\gamma)}. \tag{56}$$

If either of Eqs. (53) or (54) cannot be solved, the step is refused and tried again with $h_n = h_n/2$. Otherwise the next timestep size is estimated from the local truncation errors as $h_{est} = h_n r^{-1/3}$, where r is given by

$$r = \sqrt{\frac{1}{N}\sum_{i=1}^{N}\left(\frac{\Upsilon_i}{\epsilon_R|q(t_n+h_n)| + \epsilon_A}\right)^2}, \tag{57}$$

where the sum is taken over all unknowns, and ϵ_R and ϵ_A are the relative and absolute errors, respectively, which can be adjusted by the user [74, 80].

Appendix E

Small signal analysis

In an alternating current (AC) simulation, ISE-TCAD computes the complex small signal admittance matrix Y. This matrix specifies the current response at a given node to a small voltage signal at another node as

$$\bar{i} = Y \cdot \overline{u} = A \cdot \overline{u} + j \cdot \omega \cdot C \cdot \overline{u}, \tag{58}$$

where $\bar{i}$ is the vector containing the small signal currents at all nodes and $\overline{u}$ is the corresponding voltage vector. Parameters A and C are the conductance and capacitance matrices, respectively, and ω is the angular frequency given by $\omega = 2\pi f$, where f is the small signal voltage frequency. Finally, j is the amplitude of the small signal current that was used to test the current response at the nodes. ISE-TCAD performs the small signal analysis at a single frequency or multiple frequencies at each bias voltage step during a sweep of the external voltage source in quasi-stationary simulation [74].

References

[1] The Large Hadron Collider: Conceptual Design, CERN-AC-95-05-LHC, 1995.

[2] ATLAS: Technical proposal for a general-purpose p p experiment at the Large Hadron Collider at CERN CERN-LHCC-94-43, CERN-LHCC-P2, 1994.

[3] CMS, the Compact Muon Solenoid: Technical proposal, CERN-LHCC-94-38, 1994.

[4] LHCB Technical Proposal, CERN-LHCC-98-4, 1998.

[5] TOTEM: Technical design report. Total cross section, elastic scattering and diffraction dissociation at the Large Hadron Collider at CERN, 2004.

[6] ALICE Technical Proposal, CERN-LHCC-95-71, 1995.

[7] F. Gianotti, M. L. Mangano and T. Virdee *et al.*, Eur. Phys. J. C **39** (2005) 293–333.

[8] D. J. Griffiths, Introduction to Elementary Particles, (Wiley, John & Sons, Inc., 1987).

[9] S. F. Novaes, Standard Model: An Introduction, hep-ph/0001283.

[10] K. L. Gordon, Modern Elementary Particle Physics, (Perseus Books, 1987).

[11] D. P. Roy, Basic Constituents of Matter and their Interactions — A Progress Report, hep-ph/9912523.

[12] B. R. Martin and G. Shaw, Particle Physics (second edition), (Wiley, John & Sons, Inc., 1999).

[13] D. A. Bromley, Gauge Theory of Weak Interactions, (Springer, 2000).

[14] E. S. Abers and B. W. Lee, Physics Reports (Elsivier) **C9** (1973) 1–141.

[15] M. J. Herrero, The Standard Model, hep-ph/9812242, 1998.

[16] J. D. Barrow and F. J. Tiple, The Anthropic Cosmological Principle, (Oxford University Press, 1986).

[17] F. Halzen and A. D. Martin, Quarks and Leptons: An Introductory Course in Modern Particle Physics, (Wiley, John & Sons, Inc., 1984).

[18] D. Gross, D. Politzer and F. Wilczek, The Nobel Prize in Physics 2004 – Information for the public, Online at http://nobelprize.org/physics/laureates/2004/public.html.

[19] A. Kiiskinen, Looking for Physics Beyond the Standard Model: Searches for Charged Higgs Bosons at e^+e^- Colloiders, INTERNAL REPORT, HIP - 2004 - 01.

[20] D. Chakraborty, J. Konigsberg, Review of Top Quark Physics, hep-ph/0303092, (2003).

[21] J. Hogan, Nature **445** (2007) 239.

[22] Fermilab Press Releases 01/08/07, CDF precision measurement of W-boson mass suggests a lighter Higgs particle *Online* at http://www.fnal.gov/pub/presspass/press_releases/LighterHiggs.html, (2007).

[23] A. B. Kaidalov, V. A. Khoze, A. D. Martin and M. G. Ryskin, Eur. Phys. J. C **33** (2004) 261–271.

[24] CMS outreach, physics plots, *Online* at http://cmsinfo.cern.ch/outreach/CMSdocuments/CMSplots/CMSplots.html, (2003).

[25] P. D. B. Collins and A. D. Martin, Hadron Interactions, (Adam Hilger Ltd., 1984).

[26] V. A. Khoze, A. D. Martin and M. G. Ryskin, Eur. Phys. J. C **23** (2002) 311.

[27] Prospects for Diffractive and Forward Physics at the LHC, The CMS and TOTEM diffractive and forward physics working group, CERN/LHCC 2006-039/G-124, CMS Note-2007/002, TOTEM Note 06-5, (2006).

[28] A. De Roeck, V. A. Khoze, A. D. Martin, R. Orava and M. G. Ryskin, Eur. Phys. J. C **25** (2002) 391–403.

[29] V. A. Khoze, A. D. Martin and M. G. Ryskin, European Physical Journal C **14** (2000) 525.

[30] J. Monk and A. Pilkington, Computer Physics Communications **175** (2005) 232.

[31] M. Glück, E. Reya and M. Stratmann, Phys. Rev. D **51** (1995) 3220–3229.

[32] P. Vanlaer, Track and Vertex Reconstruction in CMS for key physics processes, in proceedings of Hadron Collider Physics conference, Les Diablerets, Switzerland, (2005).

[33] F. C. Icelin, J. M. Jowett, J. Pancin and A. Adelmann, MAD Version 9, CERN-SL-2000-026 AP (2000).

[34] Lattice & optics version 6.2, *Online* at http://proj-lhc-optics-web.web.cern.ch/proj-lhc-optics-web/V6.2/.

[35] K. Eggert and A. Morsch, Leading proton detection in diffractive events for an LHC low beta insertion, CERN-AT-94-09-DI, CERN-LHC-NOTE-289, (1994).

[36] V. Avati and K. Österberg, TOTEM forward measurements: leading proton acceptance, CERN-2005-014, DESY-PROC-2005-001, (2005), p. 452-454.

[37] Lattice & optics version 6.5, *Online* at http://proj-lhc-optics-web.web.cern.ch/proj-lhc-optics-web/V6.5/.

[38] The MAD-X program, Version 10, *Online* at http://www.cern.ch/mad.

[39] The TOTEM Collaboration, Letter of Intent, CERN-LHCC 97-49, LHCC/I11 1997.

[40] The TOTEM Collaboration, Technical Proposal, CERN-LHCC 99-7, LHCC/P5, 1999.

[41] V. Avati *et al.* with J. Kalliopuska, Eur. Phys. J. C **34** (2004) 255–268.

[42] M. Deile, Czech. J. Phys. **55** (2005) B757–B767.

[43] C. Bourelly, J. Soffer and T. T. Wu, Eur. Phys. J. C **28** (2003) 97.

[44] A. Ageer *et al.*, Nucl. Part. Phys. **28** (2002) R117–R215.

[45] B. E. Cox, The FP420 R&D Project at the LHC, hep-ph/0609209, 2006.

[46] B. E. Cox *et al.*, Detecting the standard model Higgs boson in the WW decay channel using forward proton tagging at the LHC, hep-ph/0505240, 2005.

[47] B. E. Cox, C. Da Via *et al.*, FP420 : An R&D Proposal to Investigate the Feasibility of Installing Proton Tagging Detectors in the 420m Region at LHC, *Online* at http://www.fp420.com/papers/fp420_UK_2006.pdf.

[48] Lattice & optics version 6.4, *Online* at http://proj-lhc-optics-web.web.cern.ch/proj-lhc-optics-web/V6.4/.

[49] E. Noschis *et al.*, Nuclear Instruments and Methods in Physics Research A **563** (2006) 41–44.

[50] G. F. Knoll, Radiation detection and measurement, (Wiley, John & Sons, Inc., 1989).

[51] G. Lindström *et al.*, Nucl. Inst. Meth. A **466** (2001) 308–326.

[52] M. Laakso, P. Singh and P. F. Shepard, Nucl. Inst. Meth. A **327** (1993) 517–522.

[53] V. A. J. van Lint, T. M. Flanagan, R. E. Leadon, J. A. Naber and V. C. Rogers, Mechanism of radiation Effects in Electronic Materials, (Wiley, John & Sons, Inc., 1980).

[54] M. Huhtinen, Nucl. Inst. Meth. A **491** (2002) 194–215.

[55] A. Vasilescu and G. Lindström, Displacement Damage in Silicon, *Online* at http://sesam.desy.de/members/gunnar/Si-dfuncs.html.

[56] R. Wunstorf, Systematische Untersuchungen zur Strahlenresistenz von Silizium Detektoren fur die Verwendung in Hochenergiephysik Experimenten, Ph. D. thesis, Universität Hamburg, Hamburg, Germany (1992).

[57] A. Candelori, Nucl. Inst. Meth. A **560** (2006) 103–107.

[58] E. H. M. Heijne *et al.*, Nucl. Inst. Meth. **178** (1980) 331–343.

[59] J. Kemmer, Nucl. Inst. Meth. A **169** (1980) 499.

[60] S. Parker, C. Kenney and J. Segal, IEEE Trans. Nucl. Sci. **A 395** (1997) 328–343.

[61] C. Kenney, S. Parker, J. Segal and C. Storment, IEEE Trans. Nucl. Sci. **46** (1999) 1224–1236.

[62] C. Da Via *et al.*, Nucl. Inst. Meth. A **509** (2003) 86–91.

[63] C. J. Kenney, J. D. Segal, E. Westbrook, S. Parker, J. Hasi, C. Da Via, S. Watts and J. Morse, Nucl. Inst. Meth. A **565** (2006) 272–277.

[64] D. Pennicard, G. Pellegrini, M. Lozano, R. Bates, C. Parkes and V. Wright, Simulation results from double sided 3D detectors, N45-1, presented in NSS-MIC 2006 conference, San Diego, USA, (2006).

[65] G. Pellegrini, M. Lozano, J. Rafi, M. Ullan, R. Bates, D. Pennicard and C. Fleta, Double sided 3D detector technologies at IMB-CNM, N30-202, presented in NSS-MIC 2006 conference, San Diego, USA, (2006).

[66] X. Llopart, M. Campbell, R. Dinapoli, D. San Segundo and E. Pernigotti, IEEE Trans. Nucl. Sci. **49** (2002) 2279–2283.

[67] G. Pellegrini, Technology Development of 3D Detectors for High Energy Physics and Medical Imaging, Ph. D. thesis, University of Glasgow, Scotland, (2002).

[68] Surface Technology Systems Ltd, Product manual, *Online* at http://www.stsystems.com, (2003).

[69] S. Lourdudoss and S. L. Zhang, Applied Physics Letters **64** (1994) 3461–3463.

[70] H. K. Gummel, IEEE Trans. Elect. Dev. **ED-11** (1964) 455–456.

[71] D. P. Kennedy and R. P. O'Brien, IBM J. Res. Develop. **13** (1969) 662–674.

[72] J. W. Slotboom, Electron. Lett. **5** (1969) 667–678.

[73] E. M. Buturla, P. E. Cottrell, B. M. Grossman and K. A. Salsburg, IBM J. Res. Develop. **25** (1981) 218–239.

[74] ISE Integrated Systems Engineering AG, Zurich, Switzerland, ISE-TCAD Release 6.1, Reference manual, *Online* at http://www.ise.ch, (2003).

[75] CERN irradiation facility, IRRAD-1 (CERN PS East Hall), *Online* at http://irradiation.web.cern.ch/irradiation/irrad1.htm, (2003).

[76] RD50 Status Report 2002/2003, Radiation hard semiconductor devices for very high luminosity colliders, CERN-LHCC-2003-058, LHCC-RD-002, (2003).

[77] C. Piemonte *et al.*, Nucl. Inst. Meth. A **541** (2005) 441–448.

[78] M. Boscardin *et al.*, Characterization of 3D-stc detectors fabricated at ITC-irst, Article in Press in Nucl. Inst. Meth. A, doi:10.1016/j.nima.2006.10.367, (2006).

[79] R. E. Bank and D. J. Rose, Numerische Mathematik **37** (1981) 279–295.

[80] R. E. Bank, W. M. Coughran, W. Fichtnerm, E. H. Grosse, D. J. Rose and R. K. Smith, IEEE Trans. CAD **4** (1985) 436–451.